Control and fast Measurement of Spin Qubits

A dissertation presented

by

Christian Barthel

to

The Department of Physics

in partial fulfillment of the requirements

for the degree of

Doctor of Philosophy

in the subject of

Physics

Harvard University

Cambridge, Massachusetts

2010

Dissertation Advisor: Professor Charles M. Marcus Author: Christian Barthel

Control and fast Measurement of Spin Qubits

Abstract

This thesis presents experiments on the manipulation, measurement and coherence of an individual spin or of a two-electron spin state in GaAs double quantum dots. Single-spin qubit manipulation is discussed in the first experiment. A novel hyperfine effect on a single spin in a quantum dot is presented. Gradients in nuclear polarization allow single-spin resonance to be driven by an oscillating electric field. Spin resonance spectroscopy revealed a nuclear polarization built up by driving the resonance. The following experiments investigate measurement, relaxation and coherence of two-electron spin qubits. In the second experiments fast single-shot measurement of the singlet-triplet qubit is demonstrated using a radio frequency (rf) quantum point contact (QPC). The evolution of the GaAs nuclear state is continuously monitored, and the qualitative difference between evolution of nuclear spin components parallel and perpendicular to the applied magnetic field is illuminated. The third experiment extends on the previous by using a proximal sensor quantum dot (SQD) as a rf-charge sensor. The SQD is up to 30 times more sensitive than a comparable QPC, and yields three times greater signal to noise in rf measurements. Numerical modeling is qualitatively consistent with experiment and shows that the improved sensitivity of the SQD results from reduced lifetime broadening and screening.

In the fourth experiment the triplet relaxation time, T_1, is studied as function of magnetic field gradients induced by nuclear spin polarization for different gate voltage configuration and applied magnetic fields. A simple model describes charge relaxation after singlet-triplet mixing and agrees well with the data. The initialization fidelity of a singlet

decreases with increasing field gradients, presumably due to finite times over which the system is separated into two dots, and recombined into one dot.

The final experiment demonstrates interlacing of coherent qubit operations, via exchange and Overhauser field, with Carr Purcell (CP) spin echo sequences. Different decoupling sequences, Hahn echo (HE), CP, Concatenated dynamical decoupling (CDD) and Uhrig dynamical decoupling (UDD) are compared in their effectiveness to preserve an initialized singlet state. Coherence times $\gtrsim 100$ μs are observed for a CP spin echo sequence.

Contents

List of Figures

Acknowledgements

With the completion of my Ph.D. in sight, I can take the luxury to pause and remember the people who guided me in and contributed to this work, were part of my daily life and shared the excitement, fun and pain.

My first thanks naturally goes to Charlie who offered guidance, inspiration, support and impellent throughout all of my dissertation. Charlie invited me into his group and paired me with great teachers in the form of David Reilly and Jason Petta. He gave me challenging and exciting projects to work on, but he also gave me the means to do so. That means on the one hand excellent equipment, a shipshape lab and sufficient cryogens in order to stop an experiment not until it is done. On the other hand, and more importantly, he provided me with excellent mentors, David, Jason, Jake Taylor, Emmanuel Rashba, Mike Stopa, Hendrik Bluhm, Amir Yacoby, and most importantly himself.

A great physicist who not only has a deep understanding of theory but who also is a true experimentalist, Charlie guided my thought process while also teaching me how to wield a blowtorch to repair a broken refrigerator. He lead by example in keeping the lab orderly by personally putting tools away. He maintained a balance of being an authoritative figure, encouraging us to work hard, but also being someone we would enjoy grabbing beers and cracking jokes with. Charlie is a great example of a well-rounded physicist - he talks about Shakespeare, politics, movies and other worldly things, while still maintaining a deep understanding of his field. His example made me doubt my decision to leave science multiple times.

I am very happy to have chosen Charlie as an advisor. He always supported me, even in my choice not to follow an academic career path. With the choice of an advisor comes the choice of a lab and thus of lab mates, with whom most of the waking hours of five years

are spent, or, as in Jimmy's case, sleeping hours as well.

We few, we happy few, we band of brothers[1]

this quote, intended to motivate the English footmen to throw themselves against the french knights against all odds, in some sense describes the cohesion and determination of the members of the Marcus lab[2]. Motivated to throw themselves against the odds of getting a ******** experiment or device to work and getting out of graduate school somewhat sane, all Marcusites are united in the determination to work hard and do things right, lead by the example of Charlie. I am grateful for having had the chance to share the lab with many great undergraduate students, graduate students, post-docs and visitors.

David Reilly welcomed me to the group, and taught me about dilution refrigerators, which I - as a former atomic physicist - knew nothing about at the time. After a short time with David I went through the hard but thorough school of double dot fabrication and quadruple-dot tuning of Jason Petta. Jason is a one hundred percent determined physicist, who taught me nano-fabrication, running a dilution refrigerator and the tricks of device tuning. His strict training prepared me well for the following years. Alex Johnson always seemed to know an answer or solution when asked for help or advice, and furthermore an aura of calm emanated from him. Another dear companion from the early years is Leo DiCarlo, who not only offered advice, taught me about noise and save me from a nervous breakdown when I falsely thought I had blown up Jason's device [3]. He is also a very pleasant person to be around and to work with, and he always was a good sport when teased or made fun of. After working with Jason I was paired to work with Edward, or "Oh-Gosh" as he was lovingly called due to his frequent mutterings during lab-mishaps. The results presented in chapter 3 were obtained in collaboration with Edward. For a short time, Colin

[1] Shakespeare, Henry V

[2] At times, you would omit *happy*.

[3] Leo helped me track down the problem to a broken Lock-in.

Dillard was a Marcusite and worked with us figuring out the etching technique discussed in appendix F.

Other people visited the lab shortly during that time. Slaven, Tim, Andrew, Rob, Thomas, who I had the pleasure to meet again in Copenhagen, and Michi, who will be remembered not only for his attempts at cursing in English, were great people to work around. I also thank Michi for hosting me during my visit to the Tarucha lab in Tokyo which I enjoyed very much. Jen Harlow [4] and Carolyn Stwertka were really fun people to share the lab with, not only because they introduced me to great American literature, like *No girls allowed*.

In the later years I had the pleasure to share the lab with Jacob Aptekar, who would keep us entertained for hours during group meeting, Yiming Zhang and Doug McClure. The latter two already were in the lab before I joined, but making the move to LISE, and as in Doug's case outlasting me, makes them count into the later years. Doug's tireless efforts to ensure our data is backed up are appreciated. Jeff Miller and his plants, now slowly dying, as well as My Linh Pham - all in pink - brightened up the lab. Hugh Churchill always made his few words count, recently even cracking jokes - unexpected at first.

Many thanks to David and Jimmy, who during the typically dark third year of graduate school would help me maintain sanity and keep assuring me of the light soon to be at the end of the tunnel. David's jolly nature and his endless supply of funny, odd and interesting stories always took the weight off days of hard work. His great find in McKay, back in the days, will always be remembered. His contribution to the work presented in chapter 4 was elemental and I am grateful for what he taught me about electronics and radio-frequency. Jimmy was a great friend and invaluable partner in duels of wit, not only involving ancestral mention. He always made a great example, working extremely hard but still taking time to socialize, help out others and be a fun person to be around. Danielle also deserves lots of gratitude, being the slightly older sister, caring for the Marcusites, well beyond her exceptionally well done job as an administrator. Reuter cheered us up whenever possible

[4] Not actually a short-term visitor, but compared to being a graduate student, undergrad research is over quick and painless.

by hiding easter treats, bringing her adorable kids, and coming out dancing with us.

Maja the bird, formerly known as the bee, always was one of the boys. Chris and her would be up for dinner and beer, even host christmas parties for the lab orphans. She would even occasionally donate her Helium when other's experiments were at stake. Angela, despite her two-dimensionality, always proved large capacity to deal with crude jokes from us boys, and brightened up the lab with her high spirit. I am very grateful to Jim Medford, not only for replacing me and continuing the work on my project, but also for being a great collaborator. It was a pleasure to train Jim, and to see him grow into a partner, who contributed much work to the last two chapters of this thesis. Aside from being a hard-working colleague he is a fun person to work and hang out with as well, often demonstrating how a link to cannibalism or zombies can be found in any topic of conversation.

Nocturnal Patrick was an amazing study on how a person can exist without food or sleep but still be a really nice guy. Jonah was a pleasant person to work with, always friendly and interested in discussion. Teesa not only surprised by learning everything Edward knew in 3 weeks. She also impressed with very high ethics and responsibility, and by being a person everybody in lab loved to spend time with. Ferdinand is a phenomenon, he forgets everything and everyone while doing lab-work or thinking about physics. Despite these light streaks of autism and his quirks, he is one of the kindest people I met over the years. His stories are always entertaining and he can be relied on without doubt [5]. Sandro was a source of calm and friendliness. Menyoung would not only amuse by quoting numbers as N, but he was also be patient in teaching me Korean and come out to drink with us. Max Lemme, who turned out to be much younger inside than marriage, kids and gray hair led to expect, was happy to listen and give advice as well as to partake in foolish joking around with us. Thanks to Willy for advising me on photography. He as well as Anna, and Ruby will make a good new generation of Marcusites.

Outside of the Marcus lab, Jake Taylor became a partner in stimulating and instructive conversations early in my Ph.D. and remained one until the very end. I was happy to

[5] except for proof-reading thesis chapters

discuss ideas related to the work in chapter 3 with Mark Rudner. Discussing physics but also especially non-physics with Frank Koppens was always enjoyable. It was a great honor for me to work with Emmanuel Rashba who, despite his impressive achievements, surprised by his modesty and kindness. I found it stimulating to collaborate with him on the work presented in chapter 3, and was able to learn much from him. His passion for physics is contagious. I enjoyed the stories he shared from his rich experience and I am happy to have him on my Ph.D. committee. Mike Stopa was not only a great person to work with on the paper which is presented in chapter 5, he also also a great companion to go out with in Tokyo. Morten is a quirky physicist, with whom I enjoyed collaborating together with Mike and Jim on the work in chapter 5. It was fun to go out in Copenhagen as well as in Boston. Without the 2DEG, grown by Micah Hanson at UCSB, whom unfortunately I never met, this thesis would not have been possible.

I thank Amir for the pleasure of having him on my Ph.D. committee, and working with him on the paper presented in chapter 6. Discussion with him was always stimulating and his questions are always succinct and instructive, and kept me on my toes during my qualifying exam. Sandra Foletti not only displayed a high level of genuine openness when we were working on two different yet very similar experiments. She was also a pleasant person to interact with both in physics discussion and non-physics related conversation. Hendrik Bluhm became one of my late-stage mentors and it was a pleasure to collaborate with him on the work presented in chapter 6. He has a deep love for physics and many hours passed discussing or arguing with and learning from him. Mikey, Gilad and Vivek were a fun bunch who always happily shared the riches of the food in the Yacoby lab kitchen.

None of the work in this thesis could have been completed without the hardworking people at CNS and DEAS, many thanks to Steve Shephard, Noah Clay, Steve Sheppard, Ed Macomber, Jiangdong Deng, Ling Xie and Yuan Lu at CNS, and to Louis Defeo and his colleagues in the machine shop, as well as to James McArthur. I am grateful to the administrators of the Marcus lab during my time here, James Gotfredson, and Jess Martin and Rita Filipowicz, who always made sure Helium or other necessities were ordered and my stipend was paid.

I also want to thank my mentors and advisors before I started my Ph.D.. Professor Jodl

enabled me to engage in research before entering University and in my early undergraduate semesters. Jörg Kreutz was a great teacher during these early years. Isaac Silvera enabled me to do exciting research during a semester abroad at Harvard, made me feel welcome in the US. It was always stimulating to discuss physics with him. Sandeep Rekhi, Eran Sterer, Gerhard Böhler, Ako Chijioke were great coaches and companions during my short visit in Ike's lab.

For my Master's thesis I had the luck to work with Klaas Bergmann who is not only a great experimentalist and physicist but also a gifted manager and a great mentor who cares a great deal about the advancement of his students and mentees. I am also grateful to Frank, Manfred, Anett, Zsolt, Aigas, Vladimir, and Ruth whose company and partnership during my Master's thesis was very valuable to me.

Last but not least, I want to thank all of my friends, loved ones and my family who supported me on the way to and during my dissertation. I am especially indebted to my parents and grandparents without whom I would not be where I am now, as they gave me a strong foundation to build on. I could always count on their support and love.

Chapter 1

Introduction

1.1 Organization of this Thesis

In chapter 1, after this brief outline, I give a broad overview of the motivation for the work presented in this thesis, followed by a summary of what I believe are the key contributions. Chapter 2 starts with a brief introduction to spin qubits, which are central to this thesis, before giving a brief overview of the physics of gate-defined double quantum dots in GaAs heterostructures and some of the experimental techniques used in this thesis. Finally, a necessarily incomplete list of important, previous contributions to the field of GaAs spin qubits, that put the work in the following chapters in context, is discussed.

In chapter 3, experiments on single-spin qubits are presented. A mechanism of electric dipole spin resonance, driven by an electric field and mediated by hyperfine coupling is described. While the coherence of the evolution is lost due to the randomly fluctuating hyperfine fields, this method of spin manipulation is technically simpler than conventional magnetically driven spin resonance, because time-varying electrical fields can be created more easily on the nanoscale. The effect is useful for spectroscopic measurement of the magnetic fields at the quantum dots, for average and difference fields, and for the creation of nuclear polarizations.

In chapters 4 - 7, experiments on two-electron spin qubits are presented. Chapters 4 and 5 describe methods to rapidly determine the two-electron spin state in a single quantum measurement. In chapter 6 the influence of magnetic field gradient on triplet relaxation time is investigated, in chapter 7 the coherence of the singlet-triplet qubit is studied.

Chapter 4 discusses an experiment demonstrating the single-shot measurement of a singlet-triplet spin qubit. While previous measurements of the state of a two-electron qubit constituted ensemble averages over many individual measurements, in this work, a single quantum mechanical measurement identifies the qubit state as singlet or triplet. The measurement fidelity and visibility of the single-shot measurement are analyzed. The readout is used to monitor the time-evolution of the Overhauser field difference between two quantum dots, and to investigate the different time scale of the evolution of transversal and longitudinal nuclear spin components.

In chapter 5, the use of a sensor quantum dot (SQD) as a charge detector is demonstrated, and shown to provide a significant improvement over the work presented in chapter 4. Results from numerical simulations that are in qualitative agreement with the experiment are discussed. The numerics show that the improved sensitivity of the sensor quantum dot results from reduced lifetime broadening and reduced screening.

In chapter 6, I discuss experiments that were aimed to understand phenomenology presented in Ref. [Reilly 2008] and initially attributed to the preparation of a special nuclear spin state with zero polarization gradient. The experiments elucidate the mechanism of triplet relaxation during the two-electron spin measurement, the influence of magnetic field gradients on spin relaxation rate and on initialization and readout of the singlet-triplet qubit.

Chapter 7, describes experiments aimed at studying and extending qubit coherence. The interlacing of qubit rotations about two different Bloch sphere axis with Carr Purcell spin echo pulses is demonstrated as an initial step to coherence-protected qubit operations and to show that spin echo sequences extend the coherence of singlet-triplet superpositions as well as the coherence of initial singlet states. The coherence times of an initial singlet state for different types of spin echo sequences are compared.

Appendices give further physical background, and technical information related to the experiments. Appendix A details the fabrication recipe used to create the devices discussed in chapters 3-7, and comments on the difficulties fabricating nanoscale devices with micromagnets. In appendix B, I give a short introduction to rf-reflectometry which was essential to obtain the results of chapters 4 and 5. Appendix C presents calculations estimating signal

and noise of rf-measurements in chapters 3 and 4.Appendix D gives supplementary material to chapter 4 and Ref. [Barthel 2009], presenting the derivation of an equation. In Appendix E inhomogeneous dephasing in spin-echo experiments due to electrical pulse imperfections and drifts, is estimated. Appendix F briefly discusses the viability of etching techniques to be combined with depletion gates in GaAs quantum dot fabrication.

1.2 Motivation

1.2.1 Quantum Control over single Spins interacting with a Bath

Anyone who is not shocked by quantum theory has not understood it.

Niels Bohr

Quantum mechanics, while widely applicable and believed to be the most accurate description of nature, still offers mysteries and puzzles that are not completely understood. Among the most prominent open questions or "mysteries" are entanglement, the process of measurement, the fractional quantum hall effect and the phenomenon of decoherence. In quantum mechanics, a particle or system can be in a superposition of two distinct states, for example being located simultaneously at two different positions, or - in the case of an electron spin - pointing up and down at the same time. This is not simply a mathematical oddness, but the superposition principle is experimentally confirmed. In the 'classical' world that we observe everyday, there are no superpositions, as illustrated by the famous Schroedinger's cat paradox [Schrödinger 1935]. Generally, the laws of quantum mechanics hold at small length scales, small temperatures and only over short times, while for macroscopical objects a classical, non-quantum mechanical description is completely adequate. Interaction of quantum mechanical systems with their environment leads to decoherence and, hence, classical behavior. In the framework of quantum mechanic a measurement "collapses" the state of the system into the state corresponding to the measured observable [Wheeler 1983]. Weak measurements, however, can infer information about a quantum state without collapse while yielding non-intuitive measurement results [Aharonov 1988; Romito 2008; Katz 2008].

Electron spins in solids are ideal systems to study fundamental quantum mechanics and decoherence. Recent advances in nanoscale fabrication techniques gave birth to mesoscopic physics, allowing for length scales smaller than the particle's coherence length, such that quantum effects become important, but still large enough for the particle to interact with many other particles.

Multiple electron spins can create long-lived superposition and entangled states, and full experimental control over the Hamiltonian can be achieved electrically. The spin states are coupled to the host material via hyperfine and spin-orbit interaction. These interactions result in finite lifetime of superpositions and of entangled electron spin states, via the entanglement of the electron state with the environment. The evolution of electron spins, their interaction with each other and with the environment can therefore be electrically tuned to a wide degree. The spin state can be measured on individual spins, and in the experiments discussed in chapters 4 and 5 the spin state of a two-electron system is determined in a single quantum mechanical measurements.

1.2.2 Quantum Computation

Motivated by the simulation of physical systems Richard Feynman suggested the use of a quantum computer, with the information encoded in the quantum state of the system and the operations performed via unitary operations [38; Mermin 2007]. The probabilistic nature of physics, and multiple particle interaction and entanglement make the simulation of many physical problems too complex to solve in a classical computer, while a quantum computer possesses the same large number of degrees of freedom as a physical system of study. In a quantum computer, the bits that contain the information 1 or 0 are replaced by qubits (quantum bits) that can be in any quantum mechanical superposition of 0 and 1. As a whole, a quantum computer can be in a superposition, in multiple (or all possible) states at the same time, and therefore perform multiple (or all possible) operations simultaneously.

Due to this quantum parallelism, a quantum computer is significantly more efficient than a classical computer in the solution of certain computational problems, as was realized a full ten years after Feynman's initial proposal by Bruce Shore [Shor 1994] . The quantum algorithms most widely known are Shor's algorithm and Grover's algorithm. Shor's algo-

rithm allows to factorize numbers in an amount of time that scales as N^2, for a number with N digits, while the scaling with N for a classical algorithm is $e^{N^{1/3}}$ [Shor 1994]. Unique solutions to mathematical functions with arguments of N bits can be found in a time that scales as $2^{N/2}$ using Grover's algorithm, while the classical scaling is as 2^N [Grover 1997].

The biggest challenge in quantum computation is decoherence, which tends to make all systems behave classically at high temperatures, for large numbers of interacting particles and after long times over which a system evolves. Coupling to an environment always leads to decoherence, and cannot be avoided as the quantum computer needs to be controlled, and read out.

Recent results, however, give hope (and continued funding) to the quantum computation community. It was found by DiVincenzo that any unitary transformation on a collection of qubits can be decomposed into a series of one- and two-qubit unitary transformations [DiVincenzo 1995; Barnenco 1995]. Furthermore, it has been shown that an approximation of arbitrary single qubit operations by a discrete subset of transformations on a single qubit is sufficient for the realization of quantum computation [Kitaev 1997; Mermin 2007]. Quantum error correction allows to perform quantum computation in the presence of imperfect gate operations [Steane 1996].

Electron spins in semiconductor quantum dots are a promising system to form the qubit for quantum computation [DiVincenzo 1998; Loss 1998]. Electron spin qubits are comparatively insensitive to decoherence and dissipative initialization in a ground state is possible. Such a system can in principle be integrated with conventional semiconductor electronics, and the tools available to the semiconductor industry can be used in the fabrication and measurement of devices.

1.2.3 Spintronics

Electronics was one of the success stories of the 20th century. For 50 years, the exponential growth in computational power and functionality has followed Moores law, which predicts a doubling of the number of transistors per chip every 18 months. Conventional electronics relies on the encoding of information into electrical voltages and currents, and information storage typically is handled differently from information processing. Heat dissipation is a

burning issue especially as devices shrink and insulating layers get thinner thereby increasing leakage currents. The reduction in device size faces an unsurmountable boundary as atomic length scales are approached.

Employing the electron spin as the smallest unit of information, even without harnessing the powers of quantum computation, promises several advantages over conventional electronics [Prinz 1998; Das Sarma 2001; Datta 1990]. In spin electronics (spintronics), storage and manipulation can in principle be done in the same devices, and a reduction of power dissipation and device size is possible.

In order to realize spintronic devices, we need to understand how spins are transported through materials, how to create aligned spins, and how to manipulate and control the direction of spins. Semiconductor quantum dots offer highly tunable systems in which spin dependent electron transport and electron tunneling can be studied. Experiments investigating decoherence of electron spins may provide insights that help to preserve information in spintronics devices. Decoherence and spin relaxation are important parameters. Methods to electrically manipulate spin may prove useful as tools in applications or in basic research on electron-spin devices.

1.3 Summary of Contributions

The key contributions reported here are as follows:

- In Chapter 3, electrically driven spin resonance of a single electron is demonstrated. By studying the magnetic field dependence of the resonance strength, it is shown that a novel mechanism couples the electric field to the electron spin, namely a fluctuating hyperfine field. Driving the resonance is found to create a nuclear polarization in the quantum dot. Using a micromagnet to create a magnetic field gradient across the device, a technique to address individual spins in a multi-electron device is presented.

- In Chapter 4, rapidly repeated high-fidelity ($> 90\%$) single-shot measurements of a singlet-triplet qubit is demonstrated for measurement times of a few microseconds. Quasi-static nuclear Overhauser fields are observed and their evolution is monitored. A model of single-shot readout statistics that accounts for T_1 relaxation, is developed.

It is shown that the transverse component of the Overhauser field difference is not quasi-static on the time scale of data acquisition, as expected theoretically.

- In Chapter 5, the use of a sensor quantum dot (SQD) for fast charge and two-electron spin-state measurement are demonstrated. The performance of the SQD is compared to quantum point contact (QPC) sensors for dc and radio-frequency (rf) measurement. The SQD is up to 30 times more sensitive, provides roughly three times the signal to noise ratio (SNR) of a comparable QPC. Numerical simulations, also presented, elucidate the role of screening in determining the sensitivity of proximal charge sensors.

- In Chapter 6, nuclear polarization gradients built by electrical pump-cycles are investigated. An increased triplet relaxation rate, during measurement, with increasing nuclear field gradient is found and characterized. A model describing triplet decay is developed, describes the data well and provides guidance in the choice of parameters to improve measurement visibility. Initialization and readout fidelity of the qubit in the presence of field gradients are studied as function of pulse rise- and ramp- times.

- In Chapter 7, the protection of a singlet-triplet superposition from decoherence is demonstrated by interlacing qubit rotations about two different Bloch sphere axes with Carr Purcell spin echo pulse sequences. Coherence times of a singlet, decoupled by a single Hahn echo, a Carr Purcell echo sequence with 16 π-pulses, a 5th order Concatenated dynamical decoupling sequence, and a 22nd order Uhrig decoherence decoupling sequence are compared. Singlet coherence times beyond 100 μs are achieved.

Chapter 2

Spin Qubits in GaAs Double Quantum Dots

2.1 Spin Qubits

A qubit for quantum information processing can be realized by any two-level system, which allows for manipulation of its state, that can be coupled to another two-level system, and that can be measured. The challenge lies in the coupling qubits to each other and to a classical control apparatus, to enable manipulation of the qubit state, without inducing decoherence.

Electron spins are arguably the most fundamental manifestation of a quantum mechanical two-level system. They are promising candidates for qubits, because the spin does usually not strongly couple to the environment, while the charge of the electron allows to localize, move and manipulate the system electrically. The two implementations, on which most work has been done in recent years, are single-spin and two-electron spin qubits. Both are discussed briefly in the following.

2.1.1 Single-Spin Qubits

In single-spin qubits [Loss 1998], the information is encoded in the quantum state of a spin in a large applied magnetic field (> 1 Tesla) [Elzerman 2004]. The basis states of the qubit are the states $|\uparrow\rangle$ and $|\downarrow\rangle$, the spin being parallel or anti-parallel to the applied field respectively. The qubit bloch sphere, a graphical representation of the state of the two level system, is shown in Figure 2.1.1(a). Large applied fields are needed to create a large

enough Zeeman splitting to enable accurate measurement of the qubit state [Astafiev 2004; Elzerman 2004; Meunier 2006].

Qubit manipulations are performed by rotations around the x- and y- axis of the bloch sphere. Rotations around both axes are realized by electron spin resonance (ESR) [Rabi 1937; Bleany 1953]. An ac magnetic field, with amplitude perpendicular to the static applied field, B, and angular frequency $\omega = \omega_L$ equal to the Lamor frequency,

$$\omega_L = g\mu_B B/\hbar, \tag{2.1}$$

drives coherent oscillations between the states $|\uparrow\rangle$ and $|\downarrow\rangle$ of the qubit. The angular rate of oscillations is given by the Rabi-frequency

$$\Omega = g^*\mu_B B_1/2\hbar, \tag{2.2}$$

where B_1 is the amplitude of the ac magnetic field, orthogonal to the external field, g^* is the effective electron g-factor and μ_B is the Bohr magneton. The rotation axis in the bloch sphere is set by the phase, Φ, of the ac-field, and the electron spin can be rotated around any axis in the (x, y) plane, see Fig. 2.1.1(a).

2.1.2 Two-Electron Spin Qubits

Two-electron spin qubits are encoded in the entangled state of two electrons [Levy 2002]. The basis is formed by the singlet state $S = (|\uparrow\downarrow - \downarrow\uparrow\rangle)/\sqrt{2}$ and the triplet state $T_0 = (|\downarrow\uparrow + \uparrow\downarrow\rangle)/\sqrt{2}$, with magnetic quantum number, $m = 0$. Figure 2.1.1(b) shows the Bloch sphere of the qubit which, as opposed to the single-spin qubit, does not have a real space interpretation.

The singlet-triplet basis of two electron spins had originally been suggested as a logical qubit by Levy, because it is inherently protected against collective dephasing [Levy 2002]. More importantly all-electrical sub-nanosecond operations on the qubit are possible, and have been realized [Petta 2005]. Using the exchange energy, J, between singlet and triplet states allows to perform rotations around the z-axis of the qubit Bloch sphere, see Fig. 2.1.1(b).

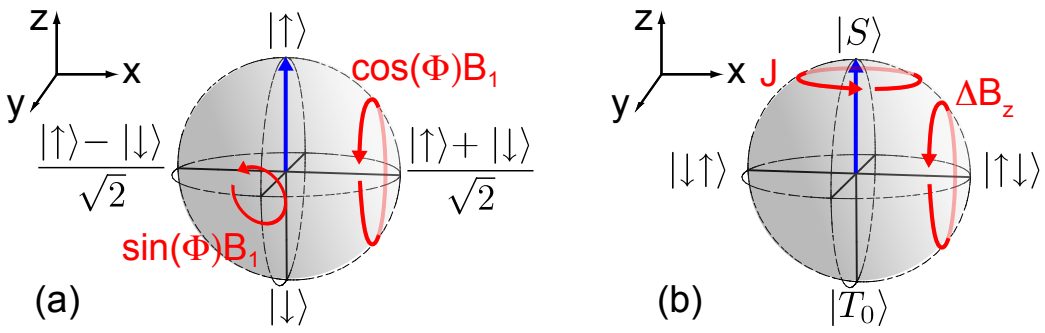

Figure 2.1: Single-spin and two-electron spin qubit bloch spheres (a) The Bloch sphere is a graphical representation of the quantum state of a two-level system, in our case of the direction an electron spin. The inclination from the z-axis θ is determined by the probability amplitude of the spin superposition state, $P_\uparrow = \cos^2\theta$, while the azimuthal angle gives the phase of a superposition state of two spin directions. Rotations about the x- and y-axis of the Bloch sphere are realized via an oscillating magnetic field with amplitude B_1, perpendicular to the applied static magnetic field, see text. The phase of the oscillating field Φ sets the axis of rotation on the Bloch sphere. (b) The Bloch sphere of the two-electron spin qubit does not have a real space interpretation, as opposed to the single-spin qubit. The qubit is spanned by the singlet and triplet states S and T_0 and rotations around the z-axis of the Bloch sphere are induced by an energy difference, J, between singlet and triplet, see section 2.5. Rotations around the x-axis are driven by the projection of a magnetic field difference between the two electrons,$\Delta\ B_z$, onto the average magnetic field direction.

Qubit rotations around a second independent axis are needed for universal control, and can be induced around the x-axis of the Bloch sphere by a magnetic field difference,$\Delta\ B_z$, between the two electrons. A field difference for these rotations can be realized via a micro magnet, [Pioro-Ladrière 2007] and has recently been realized via a gradient in the nuclear polarization of the host material containing the electron spins, see section 2.5 and Ref. [Foletti 2009].

Single-shot readout of the qubit has been realized as part of the work presented in this thesis and is discussed in Ref. [Barthel 2009] and chapter 4. Coherence times over 200 μs can be achieved using a spin echo sequences [Hahn 1950; Carr 1954; Meiboom 1958; Bluhm T_2 2010] to suppress hyperfine dephasing [Petta 2005]. Thus all necessary components for single qubit operations have been implemented, however not simultaneously in a single experiment. Two-qubit operations have not yet been realized, however promising progress has been made towards the coupling of two adjacent double quantum dots [Laird 2010], each of which would contain a two-electron spin qubit [Taylor 2006].

2.2 GaAs Heterostructures and Depletion Gates

GaAs heterostructures are ideal systems to study confined electrons and electron spins. They provide confinement for electrons in one direction by an electronic band structure tailored to the experimental needs. At low temperatures the confined electrons behave like a two-dimensional electron gas (2DEG), as they are free to move in the directions perpendicular to the confinement direction [Beenakker Review 1991; Johnson Thesis 2005]. Very clean crystals are grown by molecular beam epitaxy (MBE) [Drummond 1986] on top of a GaAs substrate, as illustrated in Fig. 2.2(a). A superlattice, 30 alternating layers of GaAs and $Al_{0.3}Ga_{0.7}As$, is deposited on the GaAs substrate by MBE, in order to minimize lattice mismatch at the heterostructure. The experimental system is created by a layer of Si dopant atoms, that forms and donates electrons to a triangular quantum well at the interface of the 800 nm GaAs- and the 100 nm $Al_{0.3}Ga_{0.7}As$ layers. One of the bound states of the triangle well, indicated by the thick solid line in the energy level diagram in Fig. 2.2(a), lies below the Fermi energy and forms the 2DEG, while other sub-bands [thick dashed line in Fig. 2.2(a)] are not occupied at low temperatures.

The electrons in the 2DEG can be further confined by application of negative voltages to top gates, as illustrated in Fig. 2.2(b). Metallic gates, patterned by electron-beam lithography and deposited by thermal or electron-beam evaporation, create Schottky diodes. These diodes are reverse-biased by negative voltages, which locally change the electric potential experienced by electrons in the 2DEG underneath. For voltages low enough, the region of 2DEG directly underneath the gate can be depleted, completely emptied of electrons, as indicated by the dashed line region of the 2DEG underneath the gates in Fig. 2.2(b). In this work the top gates are realized by a 15 nm layer of gold on top of a 5 nm layer of titanium to ensure strong adhesion of the gold to the GaAs wafer, see Appendix A.

The 2DEG is electrically contacted by a mixture of Gold and Germanium that diffuses down to the 2DEG from Platinum-Gold-Germanium contact pads during a thermal annealing step, see Fig. 2.2(b). The contact pads are deposited on the surface of the wafer by photo-lithography and electron-beam evaporation. Details are provided in Appendix A.

The schematic in Fig. 2.2(a) shows the parameters of the wafer 050329A grown by Micah

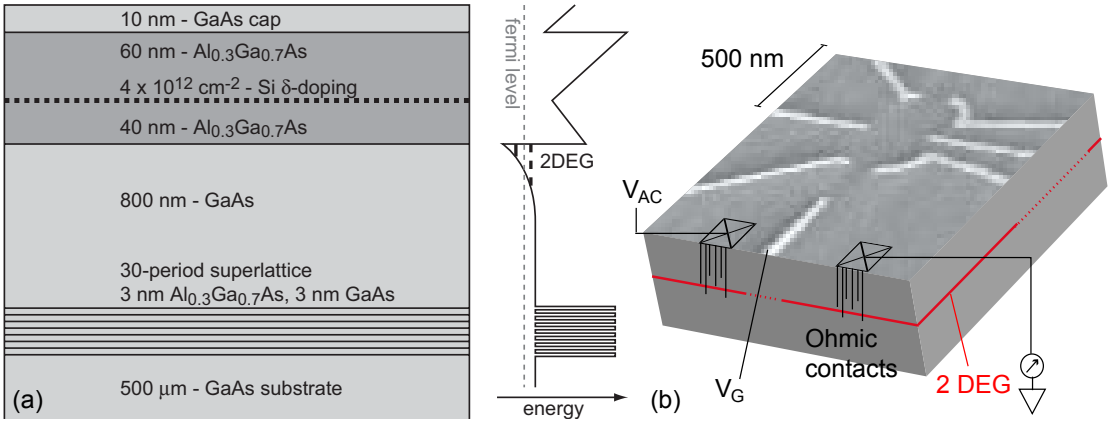

Figure 2.2: GaAs heterostructure and depletion gates. (a) Schematic of GaAs/AlGaAs heterostructure (left), shows layers of GaAs, and $Al_{0.3}Ga_{0.7}As$ that are deposited to form a triangular potential well at the interface of the 800 nm GaAs layer and the 100nm $Al_{0.3}Ga_{0.7}As$ layer, as shown by the profile of the conduction band on the right. One sub-band (thick solid line) lies below the Fermi level and forms the two-dimensional electron gas (2DEG), while other sub-bands (thick dashed line) are not occupied at low temperatures. The specific layer-thicknesses are for the wafer 050329A (grown by M. Hanson in the group of A.C. Gossard at U.C. Santa Barbara), which is used in the experiments described in this thesis. (Image adapted from Ref. [Johnson Thesis 2005]) (b) Ohmic contact is made to the 2DEG by thermal annealing of Pt/Ge/Au pads (black spikes, see Appendix A), allowing measurement of charge transport through devices. Negative gate voltages, V_G, are applied to metal top gates (light gray), to deplete the (2DEG) underneath and form constrictions, like quantum point contacts (QPCs) or quantum dots.

Hanson in the Gossard group at U. C. Santa Barbara. All experiments described in this thesis are performed on four devices fabricated from this wafer.

Charge noise and telegraph noise [1] due to switching of charges between donors in the dopant layer and due to electrons tunneling through the Schottky barriers of top gates [Buizert 2008], pose a major complications in device tuning and operation. Different wafers have different quality, characterized by the absence of switching noise. Limiting the magnitude of the negative applied gate voltages, aided by the application of a positive bias during cool-down (see Appendix B.4 of Ref. [Laird 2010] and Ref. [Buizert 2008]), reduces charge noise as demonstrated in Ref. [Buizert 2008]. If charge noise from the GaAs heterostructure becomes the limiting noise, after eliminating noise from dc-wiring and pulse-generators, an

[1] called switching noise in lab jargon

insulator layer between gates and GaAs cap may reduce noise further [Buizert 2008].

2.3 Quantum Point Contacts and Quantum Dots

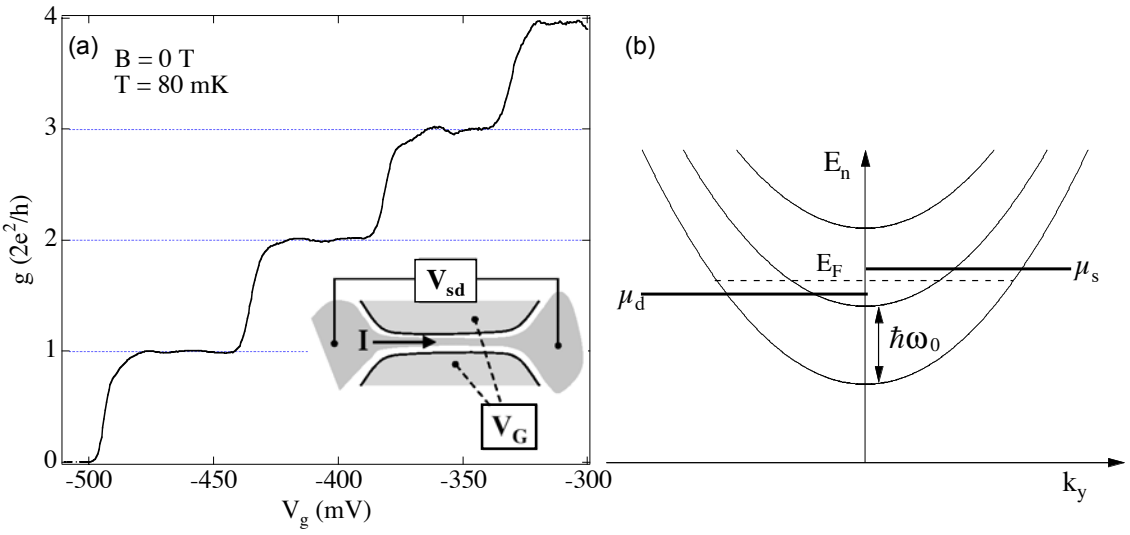

Figure 2.3: Quantum point contacts (QPC) (a) The conductance, g, through a quantum point contact (QPC) as function of the gate voltage, V_{G}, shows steep risers and flat plateaus. The gate voltage forms a one-dimensional (1D) channel in a 2DEG, as illustrated in the inset. (b) Energy of electrons in 1D the channel formed by the gate-voltage depleted 2DEG regions as function of the electron momentum along the channel. The energy of the bands is modulated by V_{G}, or any nearby source of electrical potential, like for example a charge distribution. The energy bands of the transmitting channels are spaced by an energy, $\hbar\omega_0$, due to the lateral confinement. When a new band is shifted into the bias window created by the bias voltage, V_{SD}, the conductance increases by a step $2\mathrm{e}^2/\mathrm{h}$ [Beenakker Review 1991]. Figures are adapted from Ref. [Cronenwett 2001]

A quantum point contact (QPC) is formed by a constriction due to depletion in a 2DEG, see section 2.2, that constrains electron flow through a narrow channel. Figure 2.3(a) schematically shows a QPC formed by an application of a negative gate voltage, V_{G}, to a split gate that depletes the 2DEG on two sides of a narrow channel. As with the triangular well for the vertical direction, see section 2.2, the lateral confinement of the electrons results in discretization of the lateral electron motion. The electrons behave as free particles only along the channel. A one-dimensional system is formed.

The energy bands are shown in Fig. 2.3(b) as function of the electron momentum, k_{y}, along the channel. The gate voltage V_{G} sets the electrical potential which in turn deter-

mines the chemical energies of the electron bands. By changing V_G, the number of bands that fall into the bias window can be modified. Each band increases the conductance by $2\,e^2/h$ [Beenakker Review 1991; Cronenwett 2001]. By fixing V_G to the threshold, at which an additional band enters the bias window (one of the steep risers in conductance in Fig. 2.3(a)), the conductance through the QPC becomes sensitive to the charge arrangement of nearby structures. This enables charge sensing, the measurement of the charge occupation of quantum dots and other systems, as demonstrated for double quantum dots in Ref. [Dicarlo 2004] and discussed in more detail in Ref. [Dicarlo Thesis 2007].

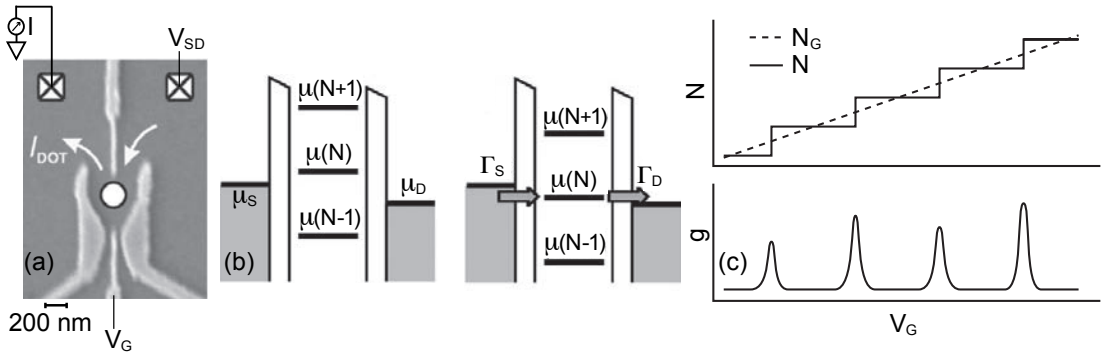

Figure 2.4: Quantum dots (QDs) (a) When gates confine semiconductor electrons into a nanometer scale island, a zero-dimensional system, similar to an atom or to the model of a particle in a box, is created. Light gray gates deplete the 2DEG underneath. The voltage V_G controls the chemical potential, $\mu(N)$, to add an Nth electron to the $N-1$ electrons trapped in the potential well of the QD. A voltage bias V_{SD} can be applied at Ohmic contacts to allow current transport through the dot via tunneling through barriers created by the gates. (b) Schematic energy levels of a quantum dot in the Coulomb blockade regime (left), where the chemical potential of no electron number state lies in the bias window, the chemical potential, μ_S, of the source lead is to low to allow tunneling of electrons onto the dot. When the chemical potential, $\mu(N)$, to add an Nth electron, lies in between the chemical potentials μ_S and μ_D of source and drain lead, electrons can tunnel from source lead onto the dot, and then from the dot to the drain lead. (a) and (b) are adapted from Ref. [Hanson 2007]. (c) Schematic charge occupation, N, (top) and conductance, g, (bottom) for transport through a quantum dot and (non-integer) minimum-energy electron number, N_G, for which the free energy would be minimized. Risers of steps in N and peaks in g correspond to the right configuration in (b), while flat regions in N and g correspond to the Coulomb blockade regime, illustrated on the left of (b). (c) is adapted from Ref. [Johnson Thesis 2005].

When top gates are used to constrain the electrons in a 2DEG to a small region, a quantum dot (QD), a zero dimensional system which often called an artificial atom, is formed. A gate defined QD is shown in Fig. 2.4(a). The equilibrium electron occupation

of the quantum dot can be changed via a top gate, that changes the size of the dot, or equivalently the electrostatic energy of conduction band electron trapped in the quantum dot. Gate voltages also set the potential barrier between the dot and the rest of the 2DEG, and therefore tune the tunnel coupling between bound states of electrons in the dot and free electron states in the 2DEG. The quasi-continuum of electronic states of the 2 DEG is referred to as leads, as they act like metallic contacts to the quantum dot. If the potential barrier between QD and the leads is large enough, with barrier-conductance $\lesssim e^2/h$, the number of charges is quantized, see Ref. [Beenakker Review 1991] for a derivation. Even though the number of charges, N_{G}, that would minimize the free energy of the system may be non-integer (dashed line in Fig. 2.4(c), top) the actual number of charges, N, is an integer [Beenakker CB 1991; Beenakker Review 1991]. When a bias is applied across a QD, then an electrical current only flows if the chemical potential $\mu(N)$ to add an N^{th} electron to the dot lies in between the chemical potentials of the leads, $\mu_{\mathrm{S}} > \mu(N) > \mu_{\mathrm{D}}$. Then electrons can hop form the source into the quantum dot and leave it by tunneling to the drain. If $\mu(N)$ lies outside of the bias window, the transport through the QD is blocked, which is called Coulomb blockade. The conductance of a QD with V_{G} biased on the steep riser of a Coulom peak (Fig. 2.4(c), bottom) is sensitive to the arrangement of nearby charges.

The charge occupation of a quantum dot or a double quantum dot (see section 2.4) can be measured with an adjacent charge sensor, which can be a QPC [Field 1993] or another quantum dot, as demonstrated as part of this thesis, and discussed in chapter 5. A change in the charge configuration of the object of interest will act as a change in electrical potential at the sensor, effectively changing V_{G} and therefore the sensor conductance as seen in Fig. 2.3(a) and in the bottom part of Fig. 2.4(c).

2.4 Double Quantum Dots and Spin Blockade

Two quantum dots, arranged next to each form a double quantum dot, if tunneling between the two dots is possible through a tunnel-barrier. A double quantum dot, as used in experiments discussed in chapters 4 - 7, is shown in Fig. 2.5(a). The two gate voltages,

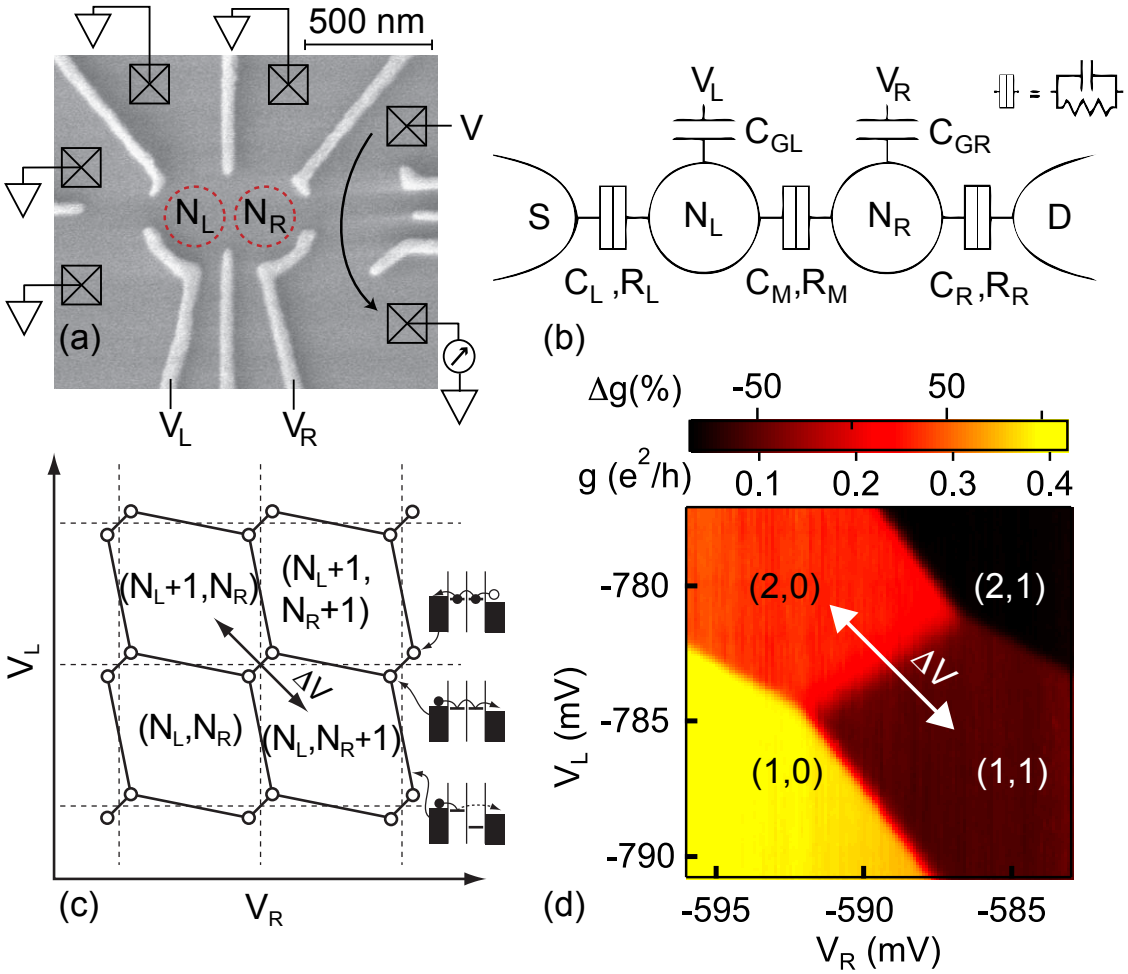

Figure 2.5: (a) Micrograph of a double quantum dot (double dot) device, see chapters 4 - 7. The top gates (light gray) confine electrons into two tunnel-coupled quantum dots (red dashed circles). Gate voltages, $V_{\rm L}$ and $V_{\rm R}$, set the electrostatic energy of left and right dot and control the double dot charge state $(N_{\rm L}, N_{\rm R})$, with $N_{\rm L}$ ($N_{\rm R}$) the number of electrons in the left (right) dot. Ohmic contacts (black boxes) allow to bias the double dot and the charge sensor. (b) Schematic of the double dot device in (a). Gate voltages $V_{\rm L}$ and $V_{\rm R}$ are capacitively coupled to the dots. Tunnel couplings between dots and between dots and leads can be modeled as resistors, parallel to capacitors. (c) Charge stability diagram of a double quantum dot, as function of gate voltages, $V_{\rm L}$ and $V_{\rm R}$. The dashed lines show the equilibrium charge states for the idealized schematic, shown in (b), with $\rm C_M = 0$. The solid lines show a realistic charge stability diagram, accounting for cross coupling (e.g. between $V_{\rm L}$ and the right dot) resulting in non-orthogonal transition lines between charge states. Gating of the left dot by the electrons in the right dot, and vice versa, results in the transition from rectangles to hexagons [Van der Wiel 2003]. (adapted from Ref. [Johnson Thesis 2005]) (d) Conductance, g, of nearby charge sensor for double dot in (a) as function of $V_{\rm L}$ and $V_{\rm R}$, with charge state $(N_{\rm L}, N_{\rm R})$, in agreement with the form in (c). Voltage detuning,$\Delta\ V$, controls the energy detuning, ϵ, between $(0, 2)$ and $(1, 1)$ charge states.

V_{L} and V_{R}, are capacitively coupled to the two dots [Van der Wiel 2003], as illustrated in Fig. 2.5(b). The gates set the electrostatic energy of left and right dot and thereby control the number of electrons on either dot [Van der Wiel 2003]. The double dot can be completely emptied of excess electrons. For the experiments described in this thesis, and generally for many thinkable applications in quantum information processing, the charge configuration is restricted to the states $(0,2)$ and $(1,1)$.

The two-electron system is controlled via the energy detuning, ϵ, between the (1,1) and (0,2) charge state. The detuning is varied via the gate voltages, V_{L} and V_{R}, and scales as $|\epsilon| = \eta\,\Delta V$, with the voltage detuning,$\Delta\ V = \sqrt{\Delta V_{\mathrm{L}}^2 + \Delta V_{\mathrm{R}}^2}$. The gate voltage detunings, ΔV_{L} and$\Delta\ V_{\mathrm{R}}$, are measured from the (1,1)-(0,2) charge degeneracy along the diagonal axis,$\Delta\ V_{\mathrm{R}} \sim -\Delta V_{\mathrm{L}}$, indicated by the double arrow in Fig. 2.5(c) and (d). The lever arm, η, is calibrated in dc transport measurements through the double dot, as illustrated in Fig. 2.6(a) and (c). An electrical bias applied across the device results in a chemical potential difference between left and right leads. When the bias is applied as in Fig. 2.6(a) electrons tunnel through the device if the gate voltages are tuned such that $\mu_{\mathrm{D}} < \mu((1,1)S) < \mu((0,2)S) < \mu\mathrm{S}$. This is the case in a triangular region near the charge degeneracy, as derived in Ref. [Van der Wiel 2003] and as can be seen in the measured current shown in Fig. 2.6(d). The length of current triangles in for forward biased transport measurements corresponds to the energy-detuning$\Delta\ \epsilon = \mathrm{e}\,\mathrm{V_{SD}} = \eta\,\Delta\mathrm{V}$ [Van der Wiel 2003].

According to the Pauli principle [Pauli 1925] the overall two-electron wavefunction has to be antisymmetric (in respect to interchange of electrons). Two electrons, forming a triplet state, must have an antisymmetric orbital wavefunction, as their spin state is symmetric. Out of two electrons in a single dot, one must therefore occupy an excited orbital state. This results in an exchange energy splitting, $J_{(0,2)}$, between a $(0,2)$ singlet state $(0,2)S$ and a $(0,2)$ triplet state $(0,2)T_0$ [Johnson PRB 2005; Ono 2002], given by the single particle level spacing due to electron confinement in the quantum dot. The exchange energy for quantum dots as discussed in this thesis is typically $J_{(0,2)} \sim 0.5$ meV.

For a $(1,1)$ charge configuration, with one electron in each dot, there also is an exchange energy splitting, J, due to the tunnel coupling between the two dots, as discussed briefly in section 2.5 and in much more detail in Ref. [Taylor PRB 2007]. The exchange, J, is

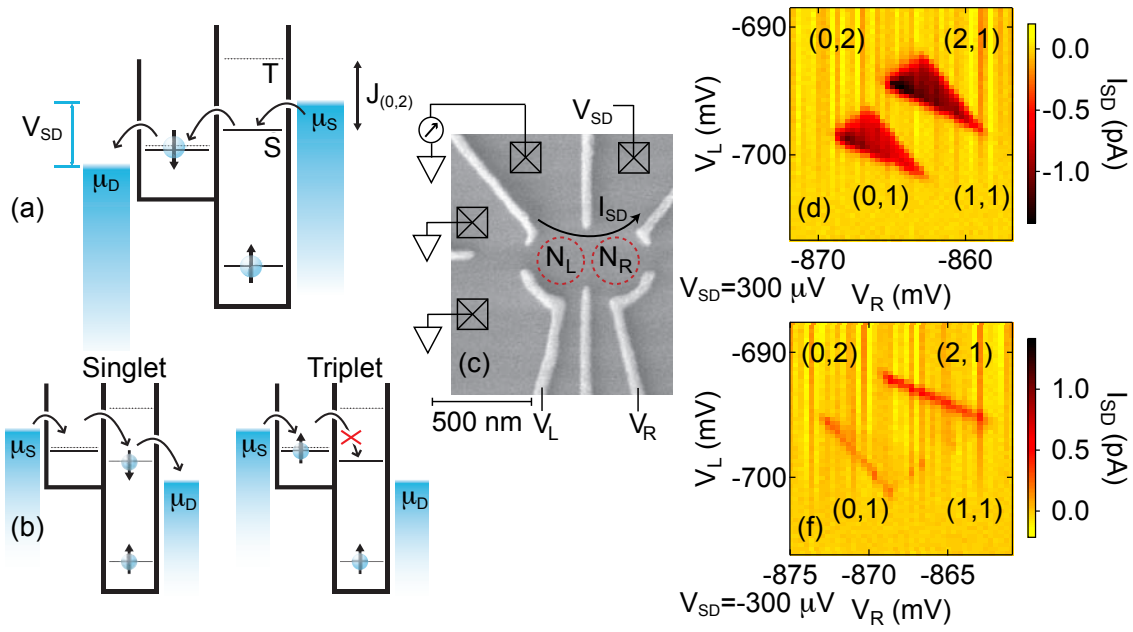

Figure 2.6: DC transport and spin blockade (a) With a forward bias [$V_{\rm SD} > 0$ for setup shown in (c)] applied, electrons can successively tunnel through the two dots, because the $(0,2)$ singlet state is loaded, and tunnels into the $(1,1)$ singlet. (b) With a reverse bias [$V_{\rm SD} < 0$ for setup shown in (c)] applied, a $(1,1)S$ state that is formed by an electron tunneling in from the leads, can tunnel through the (0,2) charge state. However, if the loaded electron forms a triplet state with the electron already in the double dot, tunneling is forbidden, as the $(0,2)$ triplet state is not energetically accessible, and transport is spin-blockaded. (a) and (b) are adapted from Ref. [Laird 2009]. (c) Setup to measure spin blockade with the electron configuration $(N_{\rm L}, N_{\rm R})$ at the $(1,1)$-$(0,2)$ degeneracy, a bias $V_{\rm SD}$ is applied across the double dot, and the current $I_{\rm SD}$ is measured. (d) Current, $I_{\rm SD}$, through the double dot, biased in forward direction. In the transport triangles a roughly homogenous current flows [Van der Wiel 2003]. (e) For a double dot in reverse bias [$V_{\rm SD} < 0$ for setup shown in (c)] , the current flow through the bias triangles is strongly suppressed [Johnson PRB 2005]. The lines of current are due to formed triplet states transitioning into singlet states by virtual electron exchange with the leads [Johnson PRB 2005].

typically much smaller than $J_{(0,2)}$, see Fig. 2.6(a), and can be made arbitrarily small via choice of gate voltages.

Spin blockade is illustrated and the singlet triplet splitting can be measured by applying a reverse bias across the double dot, as illustrated in Fig. 2.6(b), with the setup shown in Fig. 2.6(c). The chemical potential to load a singlet or a triplet state into the $(1,1)$ charge configuration is practically identical, compared to other energy scales. If the electron loaded into the left dot forms a triplet state with the electron in the right dot, it cannot tunnel into the right dot because tunneling conserves electron spin and the $(0,2)$ triplet state is

energetically inaccessible. Due to the bias it cannot escape back to the left lead either and electron transport stops until a spin flip occurs, yielding a an almost zero average current through the double dot. The current I_{SD} is shown as function of the gate voltages$\Delta\ V_{\mathrm{L}}$ and ΔV_{R} for a reverse bias, $V_{\mathrm{SD}} = -300\ \mu$eV in Fig. 2.6(e). For a reverse bias there is no current flowing in the transport triangles. The current along the lines bordering the triangle is due to co-tunneling, electron spin flips due to virtual electron exchange with the leads. When a sufficiently large bias, $\mathrm{e\,V_{SD}} > \mathrm{J_{(0,2)}}$, is applied current starts flowing at the tip of the transport triangle. This allows to measure $J_{(0,2)}$ in a dc-measurement [Johnson PRB 2005; Van der Wiel 2003], analogous to the measurement for the lever-arm with forward bias, discussed above.

2.5 Coherent Manipulation and Decoherence of Singlet-Triplet Spin Qubits

The qubit, on which chapters 4 - 7 are focussing, is formed by the singlet-triplet basis of a pair of electron spins in a double quantum dot [Levy 2002], see section 2.1.2. As discussed in section 2.4, two electrons can be trapped in a double dot, and the energy detuning, ϵ, between the charge states $(0, 2)$ and $(1, 1)$ of the double dot can be controlled via the gate voltage detuning,$\Delta\ V$, as illustrated in Fig. 2.5(c), (d). The energy detuning can also be used to control and manipulate the spin state of the two electrons, thanks to the Pauli principle which leads to an influence of the spin-state on the orbital wave function and charge state, and vice versa.

To understand the singlet-triplet qubit, its proposed operation and the experiments discussed in the following, it is instructive to consider the energy level diagram as a function of detuning, ϵ, shown in Fig. 2.7. The singlet states of $(0, 2)$ and $(1, 1)$ anti-cross at $\epsilon = 0$, because an increase in energy detuning makes it more favorable for the two electrons to occupy one dot. For two electrons occupying one dot, there is a large exchange energy splitting $J_{(0,2)}$ between singlet and triplet states $(0, 2)S$ and $(0, 2)T_{-,0,+}$. Thus the charging energy must compensate for this, by making the occupation of a single dot more favorable, compared to a singlet, in order to load a $(0, 2)$ triplet state. The anti-crossing between the

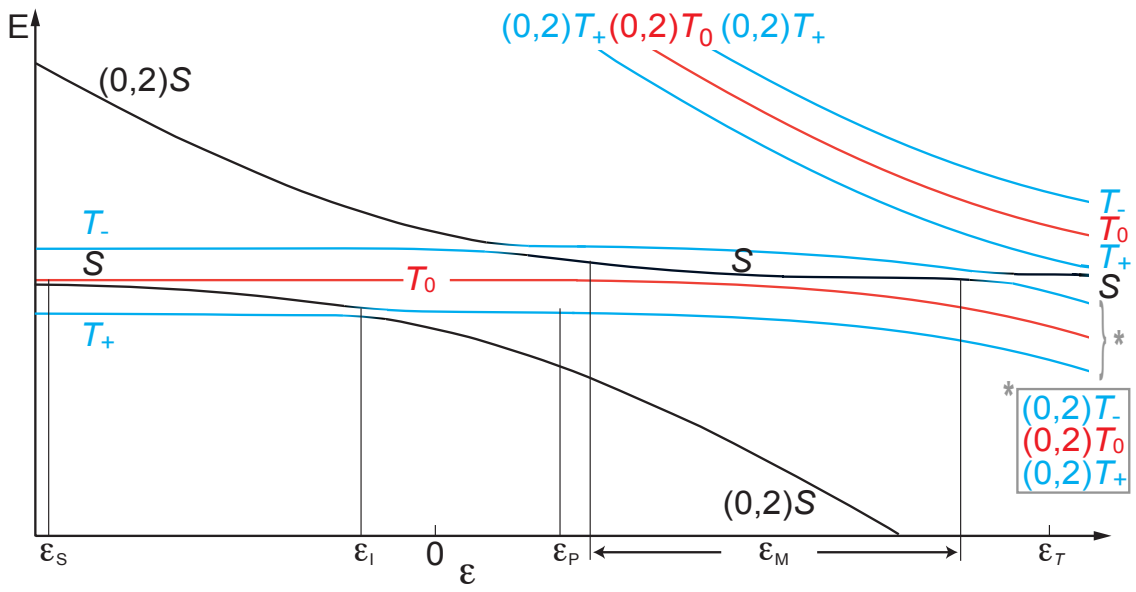

Figure 2.7: Energy level diagram of the two-electron spin system as function of detuning, ϵ; the charge state is (1,1) unless noted otherwise. The tunnel-coupling between the two dots, forms charge anti-crossings at $\epsilon = 0$, for singlet states, and at ϵ_T, for triplet states. Detunings, $\epsilon_{\rm P}$, where a $(0,2)$ singlet state is prepared via electron-exchange with the leads, $\epsilon_{\rm I}$ of $S - T_+$ resonance, and $\epsilon_{\rm S}$, where the singlet-triplet qubit is operated and where system is pulsed for $S - T_0$ precession, during pulse-cycles in the experiments discussed in chapters 4 - 7, are labeled. Ramping ϵ from positive to negative detunings rapidly, starting in $(0,2)S$, allows to initialize a $(1,1)S$ singlet state. Ramping ϵ in the opposite direction recombines singlet states into one dot, while triplet states remain in a metastable (1,1) charge configuration.

triplet states of $(0,2)$ and $(1,1)$ therefore occurs at larger energy detuning $\epsilon_T = J_{(0,2)} \sim$ 0.5 meV, as illustrated in Fig. 2.7.

The electron spin in GaAs has an effective g-factor, $g^* = -0.44$, for bulk GaAs, deviating from the free electron g-factor due to spin-orbit coupling. In quantum dots, the effective g-factor is typically slightly smaller, $g^* \sim -0.4$, see chapter 3, and Ref. [Koppens 2006]. The Zeeman energy difference between two electrons in the states $|\uparrow\downarrow\rangle$ and $|\downarrow\uparrow\rangle$ is $g^*\mu_{\rm B}\Delta B_{\rm z}$, where$\Delta$ $B_{\rm z}$ is the difference in magnetic fields between the two dots, along the total field direction (approximately the direction of the applied magnetic field).

The wavefunction of electrons in the double dot overlaps with $\gtrsim 10^6$ nuclei, with non-zero spin, and hence non-zero magnetic moment. The nuclear spins act on the electron as a Overhauser magnetic field, via the contact hyperfine interaction [Fermi 1930]. Fully polarized nuclear spins, create an effective magnetic field of ~ 5 Tesla. The nuclear spins in

the two dots each have a small random polarization due their finite number, which yields equilibrium fluctuations in effective magnetic fields with a root means square (RMS) width of $\lesssim \frac{1}{\sqrt{10^6}}$ 5 Tesla $\lesssim$ 5 mT.

The triplet states T_+ and T_- of the (1,1) charge state, with magnetic quantum number $m = 1$ and $m = -1$ respectively, and their counterparts of the $(0, 2)$ configuration, are split by an applied magnetic field, $B \gtrsim 100$ mT, large compared to magnetic fields induced by the GaAs nuclei near equilibrium. This decouples the $m = 0$ states S and T_0 from the other states and creates the two-level system that forms the singlet-triplet qubit, which is operated in the $(1, 1)$ charge configuration.

At negative detunings $\epsilon < 0$ the singlet S and triplet T_0 are split by an exchange energy $J << J_{(0,2)}$, see Fig. 2.7. The exchange energy for separated electrons is due to virtual tunneling of a singlet state into the (0,2) charge state, which is forbidden for the triplet state. The virtual tunneling results in a small admixture of the lower energy state $(0, 2)S$ to the $(1, 1)$ singlet, S, lowering its overall energy compared to the $(1, 1)$ triplet, T_0.

Rapid separation of the electrons, by pulsing ϵ to ϵ_S, initializes a (1,1) singlet state, S, if the change of energy detuning is slow enough to adiabatically follow the lower branch of the singlet anti-crossing in Fig. 2.7, but fast compared to the energy scale set by the Zeeman energy of nuclear field differences$\Delta\ B_z$ between the two quantum dots.

At detuning, ϵ_S, where the qubit states S and T_0 are nearly degenerate, a difference in magnetic field,$\Delta\ B_z$, between left and right dot, induces precession between the two states, at the $S - T_0$ precession frequency,

$$f_S = \frac{|g^*|\,\mu_B \Delta B_z}{h}. \tag{2.3}$$

, due to the energy difference between the $|\uparrow\downarrow\rangle$ and $|\downarrow\uparrow\rangle$ states resulting in an a phase difference accumulation.

The Overhauser fields from the GaAs nuclei create a random field difference,$\Delta\ B_z$ that fluctuates with an RMS width of ~ 2 mT for the double dots discussed in this thesis. This results in inhomogeneous dephasing of the qubit. An ensemble average over initial singlet states after evolution in a separated state is an incoherent mixture of singlet and triple states

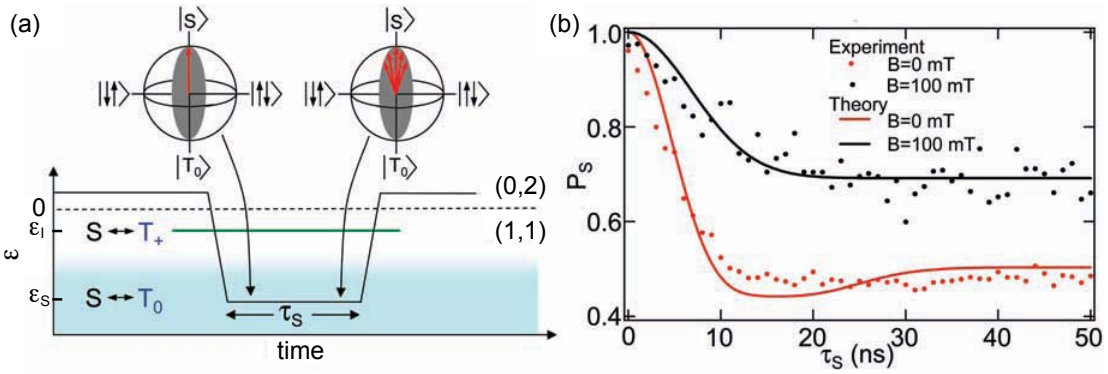

Figure 2.8: Dephasing and T_2^* (a) Pulse sequence used to measure the inhomogenous dephasing time T_2^*. The system is prepared in $(0,2)S$, the two electrons are separated by rapidly pulsing the detuning to $\epsilon_{\rm S}$. With the triplet states T_+ and T_- energetically separated by an applied magnetic field, the states S and T_0 mix at large detuning (light blue region), where the magnetic field difference between the left and the right dot, induced by hyperfine fields, drive rotations about the x axis in the Bloch sphere [See Fig. 2.1.1(b)]. After a separation time $\tau_{\rm S}$, the detuning is rapidly ramped to $\epsilon_{\rm M}$ which corresponds to a projection onto $(0,2)S$, see text. (B) Singlet probability P_S measured using the calibrated QPC charge sensor, as a function of $\tau_{\rm S}$ at an applied magnetic field of $B = 100$ mT (black curve) and $B = 0$ mT (red curve). For $\tau_{\rm S} < T_2^*$, the singlet state does not have ample time to dephase, and the system is returned as a singlet, $P_S \sim 1$. For $\tau_{\rm S} > T_2^*$, $P_S \sim 0.5$ at 100 mT and $P_S \sim 0.3$ at 0 mT. The measured saturation probabilities (~ 0.7 and ~ 0.5) are higher due to triplet relaxation during the measurement, which gives a singlet bias, see chapter 6. Fits to the model (solid curves), including a parameter adjusting measurement contrast, give $T_2^* \sim 10$ ns and the RMS width of nuclear fluctuations $B_{\rm nuc} \sim 2.3$ mT.

for separation time $\tau_{\rm S} > T_2^* = \frac{\hbar}{g^*\mu_{\rm B}B^{\rm nuc}} \sim 15$ ns, with the RMS width of the Overhauser field in one dot, $B^{\rm nuc}$ [Petta 2005]. The inhomogeneous dephasing of the qubit is illustrated in Fig. 4.6 by data from Ref. [Petta 2005], showing the probability, P_S, of the qubit being in a singlet state after evolution at $\epsilon_{\rm S}$ for a separation time, $\tau_{\rm S}$.

The qubit state, e.g. the singlet probability $P_{\rm S}$, is generally measured by reverting the singlet initialization procedure, discussed above. After evolution in a separated state, ϵ is pulsed to the measurement detuning, $\epsilon_{\rm M}$, where the $(0,2)$ charge configuration is the ground state, see Fig. 2.7. If the separated electrons are in a singlet configuration when the system is pulsed to $\epsilon_{\rm M}$, the system returns to $(0,2)$, but if the two electrons are in a triplet state, it remains locked in $(1,1)$ at $\epsilon_{\rm M}$. Superpositions are projected to one of the two charge states during measurement. The different charge states of singlet and triplet are measured via an adjacent charge sensor, as discussed in Fig. 2.5, allowing to determine the spin state.

Generally, many experimental cycles of singlet separation, evolution and recombination for spin-to-charge conversion are performed and the charge signal is averaged, yielding an ensemble averaged singlet probability [Petta 2005]. Chapter 4 discusses the implementation of single-shot qubit measurement for the singlet-triplet spin qubit [Barthel 2009].

In order to initialize the qubit in a state $|\ X\rangle$ rather than $|\ Z\rangle$, a slow sweep of ϵ from $\epsilon \lesssim \epsilon_{\mathrm{I}}$ to ϵ_{S}, maps a $(1,1)$ singlet, $S = \left(|\uparrow\downarrow\rangle - |\downarrow\uparrow\rangle\right)/\sqrt{2}$, onto the ground state of the nuclear Overhauser fields, $|\uparrow\downarrow\rangle$ [Petta 2005], as illustrated in Fig. 2.9(a). This allows to demonstrate fast z-axis rotation, driven by the exchange energy splitting, J, due to a phase accumulation between S and T_0.

After initialization into $|\uparrow\downarrow\rangle$, ϵ is pulsed to ϵ_{E}, with an exchange energy, $J_{\mathrm{E}} > |g^*|\,\mu_{\mathrm{B}}\Delta B_{\mathrm{z}}$, larger (ideally much larger) than the nuclear field gradient [Petta 2005; Foletti 2009]. This results in rapid precession around the z-axis of the qubit Bloch sphere as demonstrated in Ref. [Petta 2005] and shown in Fig. 2.9(b) and (c). The oscillations are detected by measuring the x-axis projection of the qubit as function of the exchange evolution time, τ_{E} (Fig. 2.9).

The projection of the qubit on the x-axis, or equivalently onto state $|\uparrow\downarrow\rangle$, is measured, by reverting the initialization procedure of state $|\ X\rangle = |\uparrow\downarrow\rangle$. The detuning is slowly ramped from ϵ_{S} to $\epsilon \lesssim \epsilon_{\mathrm{I}}$, mapping the state $|\uparrow\downarrow\rangle$ onto the $(1,1)$ singlet state. The state $|\downarrow\uparrow\rangle$ is mapped onto T_0. This state mapping is followed by a rapid pulse to ϵ_{M} to measure the singlet probability, P_{S}, via the double dot charge state, using the charge sensor. The measured singlet probability, shown in Fig. 2.9(b), corresponds to the $|\ X\rangle$ probability, $p(|\ X\rangle)$, before the mapping. In Ref. [Petta 2005] oscillation periods shorter than one nanoseconds were realized, the operation time for z-rotations is practically only limited by pulse rise-times.

Qubit rotations around a second independent axis are needed for universal control of the singlet-triplet qubit in order for it to be a viable system for quantum information processing. As discussed above, an x-rotation is induced by a magnetic field difference,$\Delta\ B_{\mathrm{z}}$ between the two quantum dots. A field difference for these rotations can be realized via a micro magnet on top of the double dot as experimentally shown in Ref. [Pioro-Ladrière 2007] and in Refs. [Laird 2007; Laird 2009] as part of this thesis, discussed in chapter 3.

Recently a nuclear field difference between two dots in a double dot has been realized

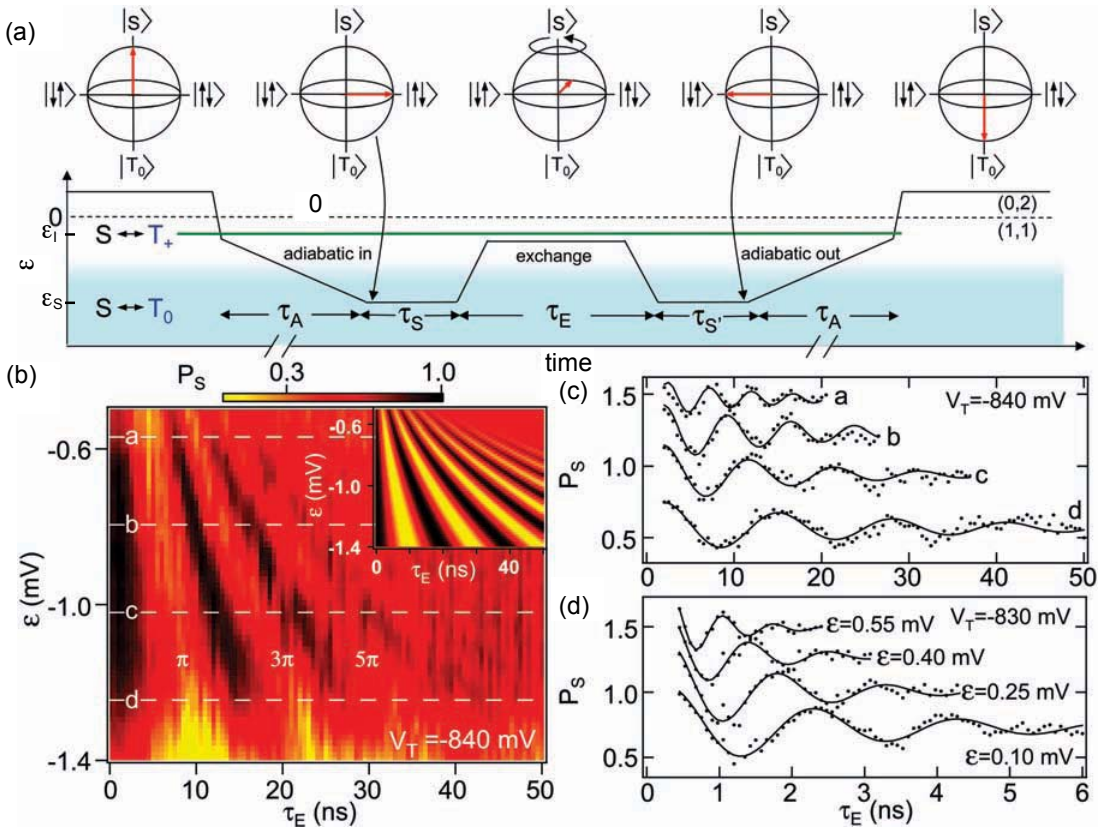

Figure 2.9: Bloch-axis z-rotations (a) Pulse sequence demonstrating rotations around the z-axis of the qubit Bloch sphere by control of the exchange energy splitting, J. After preparing $(0,2)S$, detuning is pulsed to $\epsilon \lesssim \epsilon_{\rm I}$, adiabatically compared to the inter-dot tunnel coupling but fast compared to the $S - T_+$ mixing by hyperfine fields, to initialize a $(1,1)S$ state. The following slow ramp ($t \sim 1\mu$s) to large detuning, $\epsilon_{\rm S}$ loads the system in the ground state, $|\uparrow\downarrow\rangle$ of the nuclear field difference,$\Delta\ B_{\rm z}$. An exchange pulse of duration $\tau_{\rm E}$ rotates the system about the z-axis in the Bloch sphere from $|\uparrow\downarrow\rangle$ to $|\downarrow\uparrow\rangle$. Reversing the slow adiabatic passage allows the projection onto $(0,2)S$ to distinguish states $|\uparrow\downarrow\rangle$ and $|\downarrow\uparrow\rangle$ after time $\tau_{\rm E}$. Typically, $\tau_{\rm S} \sim \tau_{\rm S}' \sim 50$ ns. (b) P_S as a function of detuning and $\tau_{\rm E}$. The z-axis rotation angle $\phi \sim J(\epsilon)\tau_{\rm E}/\hbar$ results in oscillations in P_S as a function of both ϵ and $\tau_{\rm E}$. (Inset) Model of P_S using $J(\epsilon)$ extracted from $S - T_+$ resonance condition, assuming $g^* = 0.44$ and ideal measurement contrast (from 0 to 1). (c) Rabi oscillations measured in P_S at four values of detuning indicated by the dashed lines in (b). Fits to an exponentially damped cosine function, with amplitude, phase, and decay time as free parameters (solid curves), are shown. Curves are offset by 0.3 for clarity. (D) Faster Rabi oscillations are obtained by increasing tunnel coupling and by increasing detuning to positive values, resulting in a π-pulse time of ~ 350 ps.

via a gradient in the nuclear polarization of the host material, that was created by electrical pumping of nuclear spin flips [Foletti 2009]. A creation of nuclear polarization by electrical pump cycles had originally been reported in Refs. [Petta 2008; Reilly Diff. 2008], without

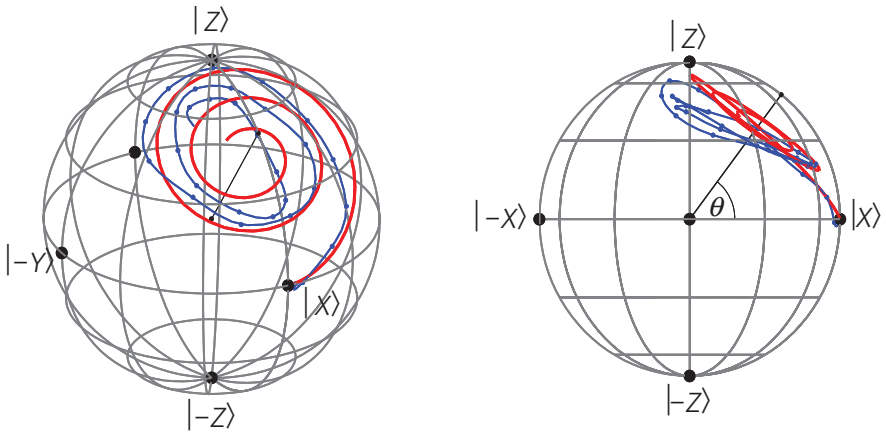

Figure 2.10: Representation of qubit trajectories in the Bloch sphere during evolution at a detuning ϵ_E (indicated in Fig. 2.7) at presence of a controlled nuclear field gradient $\Delta B_z \sim J_E/(g^*\mu_B)$. This qubit trajectory constitutes the demonstration of universal qubit gate control, as the rotation axis can be almost freely set by the values ofΔ B_z and J_E. The exchange is controlled by choice of ϵ_E and the nuclear field gradient via the electrical pump cycle. The blue line is a spline interpolation of measured data points, while the red line is the fit of a numerical solution of the Schrödinger equation incorporating finite pulse rise time and inhomogeneous broadening due to fluctuations in the nuclear field gradient. The experiment is described and the results are discussed in detail in Ref. [Foletti 2009], from where the Figure was adapted.

investigating gradients. The electrical pump-cycle is discussed in detail in Refs. [Reilly 2008; Reilly Diff. 2008] and briefly explained in the following.

Nuclear polarizations can be created electrically by repeated ramping of ϵ through the anti-crossing of singlet, S, and $m = 1$ triplet, T_+ [Foletti 2009; Reilly Diff. 2008; Reilly 2008], see Fig. 2.7. In the nuclear pump-cycle, a singlet state is prepared dissipatively, at ϵ_P as discussed above, and the detuning, ϵ, is ramped slowly through ϵ_I. When following the lower branch of the level-crossing an electron spin is flipped by hyperfine interaction, see inset of Fig. 6.2(a). Due to spin conservation a nuclear spin is flipped simultaneously. Subsequently the system is rapidly brought back to $\epsilon > 0$, without spin flip. The system is reset to a singlet state at ϵ_P, via electron exchange with the leads rather than electron-nuclear spin flips, resulting in a net nuclear spin flip per pump-cycle.

A wide range of nuclear field gradients, typically 1 mT $\lesssim \Delta B_z \lesssim$ 500 mT can be achieved and stabilized [Bluhm FB 2010]. A qubit in a separated state at a detuning ϵ_E precesses around a tilted axis in the Bloch sphere, as illustrated in Fig. 2.10. The precession

frequency

$$f_{\mathrm{E}} = \frac{\sqrt{J_{\mathrm{E}}^2 + (g^*\mu_{\mathrm{B}}\Delta B_z)^2}}{h} \tag{2.4}$$

and the rotation axis in the Bloch sphere (Fig. 2.10) are set by exchange energy and magnetic field difference which can be controlled via the detuning ϵ_{E} and the nuclear pump cycle. This rotation around an arbitrary axis on the Bloch sphere constitutes the realization of universal control of the qubit state.

Aside from being a useful tool to manipulate the qubit, the Overhauser fields of the nuclei also are the major source of qubit decoherence as discussed above (Fig. 4.6 [Petta 2005]). However the fluctuations of nuclear fields have been shown to be slow and to have a $\sim 1/f^2$ power spectrum at moderate to high applied magnetic fields [Reilly 2007]. Dephasing can be partially undone by a spin echo, a π-rotation on the bloch sphere, that refocusses the evolution of the electron spin state [Hahn 1950; Petta 2005; Bluhm T_2 2010]. The π-rotations are realized via z-rotations by pulsing the system to detuning ϵ_{E} for half an oscillation period. In a Hahn echo sequence [Hahn 1950], a π-pulse is performed after time $\tau_{\mathrm{D}}/2$ spent at ϵ_{S}, during which the qubit state precesses out of its initial state. After the π-rotation the system is rapidly brought back to S for the time $\tau_{\mathrm{D}}/2$ during which the spin state precesses back into its original state, if the nuclear field has not changed.

In Refs. [Petta 2005; Bluhm T_2 2010] a Hahn echo was used to extend the qubit coherence time from T_2^* of few nanoseconds up to ~ 30 μs. Multiple π- pulses extend the coherence to longer times, as suggested in Refs. [Carr 1954; Meiboom 1958] and experimentally demonstrated in Ref. [Bluhm T_2 2010]. For the Carr Purcell spin echo sequence, N_π π-pulses are performed, each with an equal dephasing and rephasing time, before and after the π-pulse [Carr 1954; Meiboom 1958]. Theoretical work suggests that, under the assumptions of certain dephasing power spectra, spin echo sequences more complex than CP could further increase coherence times. [Witzel CDD 2007; Uhrig 2007] In chapter 7 experiments that interlace operations around x- or z-axis of the Bloch sphere with Carr Purcell spin echoes, and experiments that compare different spin echo pulse sequences are discussed.

Therefore the requirements for single qubit operation [DiVincenzo 1998], fast measurement, initialization, universal control and long coherence times have been implemented,

while not simultaneously in a single device during a single experiment. However two-qubit operations are critical for the realization of a quantum computer [DiVincenzo 1998], and have not been realized thus far. Promising progress has been made however, the charge coupling between two adjacent quantum dots has been shown to be strong enough to in principle allow phase operations on one singlet-triplet qubit, conditional on another qubit [Laird 2010]. One of the double dots being in the (0,2) versus (1,1) configuration results in a detuning difference of$\Delta\ \epsilon \sim 50\ \mu$eV in the other double dot [Laird 2010], enough to create a significant difference in exchange oscillation frequency.

Chapter 3

A new Mechanism of electric Dipole Spin Resonance: Hyperfine Coupling in Quantum Dots

E A Laird[1], C Barthel[1], E I Rashba[1,2], C M Marcus[1], M P Hanson[3] and A C Gossard[3]

[1] Department of Physics, Harvard University, Cambridge, Massachusetts 02138, USA

[2] Center for Nanoscale Systems, Harvard University, Cambridge, Massachusetts 02138, USA

[3] Materials Department, University of California at Santa Barbara, Santa Barbara, California 93106, USA

A recently discovered mechanism of electric dipole spin resonance, mediated by the hyperfine interaction, is investigated experimentally and theoretically. The effect is studied using a spin-selective transition in a GaAs double quantum dot. The resonant frequency is sensitive to the instantaneous hyperfine effective field, revealing a nuclear polarization created by driving the resonance. A device incorporating a micromagnet exhibits a magnetic field difference between dots, allowing electrons in either dot to be addressed selectively. An unexplained additional signal at half the resonant frequency is presented [1].

---

[1]This chapter is adapted from Ref. [Laird 2007; Laird 2009] with permission,

3.1 Introduction

Electric dipole spin resonance (EDSR) is a method to electrically manipulate electron spins. In this technique, two fields are applied; a static magnetic field $\mathbf{B}$ and an oscillating electric field $\tilde{\mathbf{E}}(t)$ resonant with the electron precession (Larmor) frequency [Rashba 1962; Bell 1962; McCombe 1967; Rashba 1991]. Spin resonance techniques are of interest for quantum computing schemes based on single electron spins, because they allow arbitrary one-qubit operations [Loss 1998]. Single-spin EDSR is a particularly desirable experimental tool because it allows spin manipulation without time-dependent magnetic fields, which are difficult to generate and localize at the nanoscale [Jelezko 2004; Rugar 2004; Xiao 2004; Koppens 2006].

Achieving EDSR requires a mechanism to couple $\tilde{\mathbf{E}}$ to the electron spin $\boldsymbol{\sigma}$. This coupling can be achieved by the traditional spin-orbit interaction, which couples $\boldsymbol{\sigma}$ to the electron momentum $\mathbf{k}$, or by an inhomogeneous Zeeman interaction, which couples $\boldsymbol{\sigma}$ to the electron coordinate $\mathbf{r}$ [Pekar 1965; Rashba 1991; Kato 2003; Tokura 2006; Golovach 2006]. Single-spin EDSR has recently been achieved in quantum dots using both techniques [Nowack 2007; Pioro-Ladriere 2008].

Recently, we presented an experimental and theoretical study of a novel EDSR effect mediated by the spatial inhomogeneity of the hyperfine nuclear field [Laird 2007]. An electron moving under the influence of the electric field $\tilde{\mathbf{E}}(t)$ experiences this inhomogeneity as an oscillating hyperfine coupling which drives spin transitions. In this chapter, we illuminate the underlying physics and present new experimental data on a still unexplained phenomenon at half the resonant frequency.

This EDSR effect is observed via spin-blocked transitions in a few-electron GaAs double quantum dot [Engel 2001]. As expected for a hyperfine mechanism, but in contrast to $\mathbf{k} - \boldsymbol{\sigma}$-coupling mediated EDSR, the resonance strength is independent of $\mathbf{B}$ at low field and shows, when averaged over nuclear configurations, no Rabi oscillations as a function of time. We find that at large $\mathbf{B}$ driving the resonance creates a nuclear polarization, which we interpret as the backaction of EDSR on the nuclei [Gueron 1959; Dobers 1988; Koppens 2006; Baugh 2007; Rudner 2007]. Finally, we demonstrate that spins can be individually addressed in each dot by creating a local field gradient.

3.2 Device and Measurement

The device for which most data is presented (Figure 1(a)) was fabricated on a GaAs / $Al_{0.3}Ga_{0.7}As$ heterostructure with two-dimensional electron gas (2DEG) of density 2×10^{15} m^{-2} and mobility 20 m^2/Vs located 110 nm below the surface. Voltages applied to Ti/Au top gates locally deplete the 2DEG, defining a few-electron double quantum dot. A nearby charge sensing quantum point contact (QPC) is sensitive to the electron occupation $(N_{\rm L}, N_{\rm R})$ of the left ($N_{\rm L}$) and right ($N_{\rm R}$) dots [Field 1993; Elzerman 2003]. The voltages $V_{\rm L}$ and $V_{\rm R}$ on gates L and R can be rapidly pulsed; in addition, L is coupled to a microwave source. The static magnetic field **B** was applied in the plane of the heterostructure, and measurements were performed in a dilution refrigerator at 150 mK electron temperature.

The characteristic feature of tunnel-coupled quantum dots is a discrete electron energy spectrum. An overall shift to the spectrum, proportional to the electron occupation, is induced by V_L and V_R, which therefore determine which occupation is energetically favoured. Figure 1(b) shows the QPC conductance $g_{\rm s}$ as a function of V_L and V_R; different conductances correspond to different $(N_{\rm L}, N_{\rm R})$. For most V_L, V_R configurations, only one value of $(N_{\rm L}, N_{\rm R})$ is energetically accessible; these correspond in Figure 1(b) to regions of uniform g_s.

A bias $V_{\rm sd}$ applied across the device drives electron transport via sequential tunneling subject to two constraints [Hanson 2007]. The first constraint, Coulomb blockade, arises because for most gate configurations electrostatic repulsion prevents additional electrons from tunneling onto either dot. This constraint inhibits transport except when V_L, V_R are tuned so that three occupation configurations are near-degenerate. The energy cost of an extra electron tunneling through the device is then small enough to be provided by the bias voltage. Values of V_L and V_R satisfying this condition correspond to the two white dashed triangular regions marked in Figure 1(b), for which transport is permitted via the transition sequences $(0,2) \rightarrow (0,1) \rightarrow (1,1) \rightarrow (0,2)$ or $(0,2) \rightarrow (1,2) \rightarrow (1,1) \rightarrow (0,2)$.

A second constraint, spin blockade, is caused by the Pauli exclusion principle, which leads to an intra-dot exchange energy J_{02} in the right dot [Ono 2002; Johnson PRB 2005]. As shown in the first panel of Figure 1(c), the effect of this exchange is to make the $(1,1) \rightarrow$

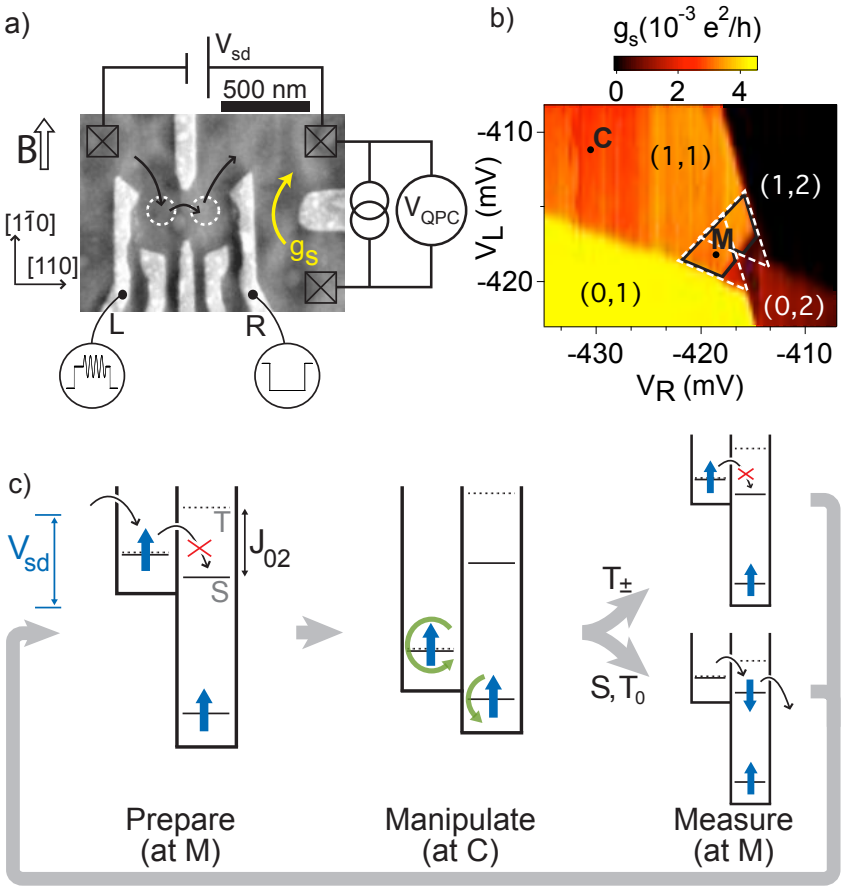

Figure 3.1: (a) Micrograph of a device lithographically identical to the one measured, with schematic of the measurement circuit. Quantum dot locations are shown by dashed circles, and a bias $V_{\rm sd}$ drives sequential tunneling in the direction marked by black arrows. The conductance g_s of the QPC on the right is sensitive to the dot occupation. The direction of the magnetic field $\mathbf{B}$ and the crystal axes are indicated. (b) QPC conductance $g_{\rm s}$ measured at $V_{\rm sd} \sim 600$ μeV near the (1,1)-(0,2) transition. Equilibrium occupations for different gate voltages are shown, as are gate voltage configurations during the measurement/reinitialization (M) and manipulation (C) pulses. The two white dashed triangles outline regions where transport is not Coulomb blocked; the solid black line outlines where spin blockade is active. A plane background has been subtracted. (c) Energy levels of the double dot during the pulse cycle (See text).

$(0,2)$ transition selective in the two-electron spin state, inhibited for triplet states but allowed for the singlet. The hyperfine field difference between dots converts the $m_s = 0$ component T_0 of the blocked triplet T to an unblocked singlet S within ~ 10 ns, as we have confirmed by the technique of [Petta 2005]. However, decay of $m_s = \pm 1$ components $T_\pm$ requires a spin flip and therefore proceeds much more slowly. This spin flip becomes the rate-limiting step in transport, and so the time-averaged occupation is dominated by the (1,1) portion of the transport sequence [Johnson PRB 2005]. Gate configurations where spin blockade applies correspond to the black solid outlined region of Figure 1(b); inside this region, g_s has the value corresponding to (1,1). Any process that induces spin flips will partially break spin blockade and lead to a decrease in g_s.

Unless stated otherwise, EDSR is detected via changes in g_s while the following cycle of voltage pulses V_L and V_R [Koppens 2006] is applied to L and R (Figure 1(c)). The cycle begins inside the spin blockade region (M in Figure 1(b)), so that the two-electron state is initialized to $(1,1)T_\pm$ with high probability. A $\sim$1 μs pulse to point C prevents electron tunneling regardless of spin state. Towards the end of this pulse, a microwave burst of duration τ_EDSR at frequency f is applied to gate L. Finally the system is brought back to M for $\sim$3 μs for readout/reinitialization. If and only if a spin (on either dot) was flipped during the pulse, the transition $(1,1) \rightarrow (0,2)$ occurs, leading to a change in average occupation and in g_s. If this transition occurs, subsequent electron transitions reinitialize the state to $(1,1)T_\pm$ by the end of this step, after which the pulse cycle is repeated. This pulsed EDSR scheme has the advantage of separating spin manipulation from readout.

Changes in g_s are monitored via the voltage V_QPC across the QPC sensor biased at 5 nA. For increased sensitivity, the microwaves are chopped at 227 Hz and the change in voltage δV_QPC is synchronously detected using a lock-in amplifier. We interpret δV_QPC as proportional to the spin-flip probability during a microwave burst, averaged over the 100 ms lock-in time constant.

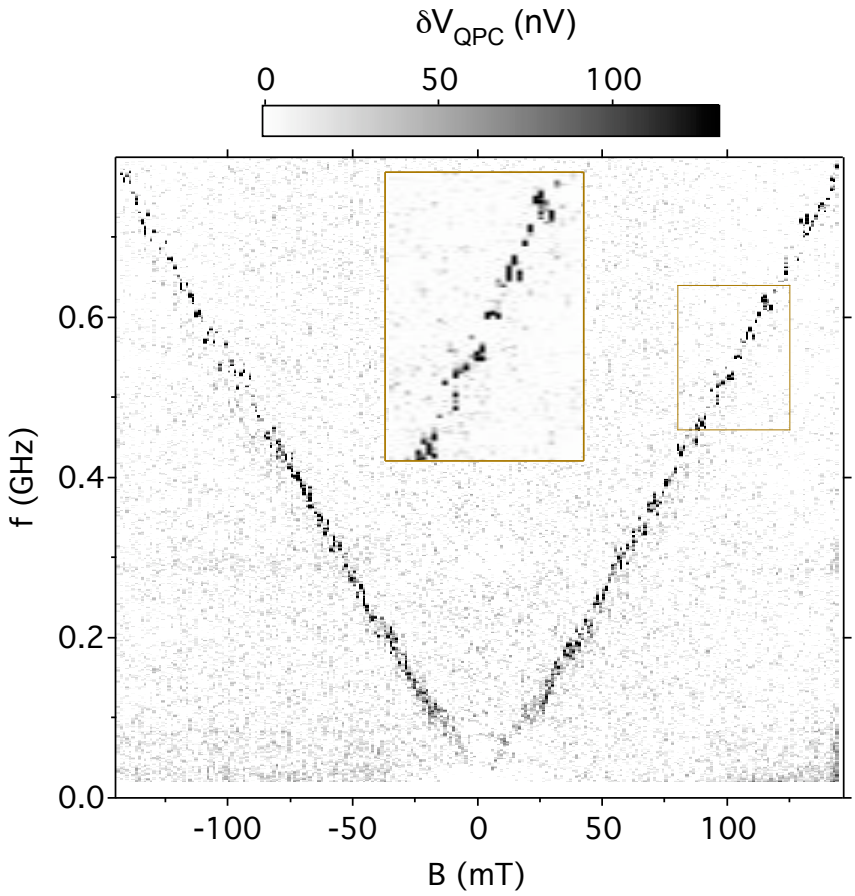

Figure 3.2: Signal of spin resonance δV_{QPC} as a function of magnetic field B and microwave frequency f. EDSR induces a breaking of spin blockade, which appears as a peak in the voltage across the charge sensor δV_{QPC} at the Larmor frequency. Field- and frequency-independent backgrounds have been subtracted. Inset: Jitter of resonant frequency due to random Overhauser shifts.

3.3 Electric Dipole Spin Resonance Spectroscopy

Resonant response is seen clearly as B and f are varied for constant $\tau_{\mathrm{EDSR}} = 1\ \mu$s (Figure 2.) A peak in δV_{QPC}, corresponding to a spin transition, is seen at a frequency proportional to B. This is the key signature of spin resonance. (A feature corresponding to lifted spin blockade around B=0 is not seen or expected, because this measurement technique is sensitive only to the differential effect of the microwaves [Koppens 2006].) From the slope of the resonant line in Figure 2 a g-factor $|g| = 0.39 \pm 0.01$ is found, typical of similar GaAs devices [Goldhaber-Gordon 1998; Hanson 2003]. We attribute fluctuations of the resonance frequency (Figure 2 inset) to Overhauser shift caused by the time-varying hyperfine field acting on the electron spin. Their range is $\sim \pm 22$ MHz, corresponding to a field of ~ 4 mT, consistent with Overhauser fields in similar devices [Koppens 2005; Johnson Nature 2005; Petta 2005].

Information about the EDSR mechanism can be obtained by studying the peak height as a function of duration, strength, and frequency of the microwave burst (Figure 3). To reduce the effects of the shifting Overhauser field, the microwave source is frequency modulated at 3 kHz in a sawtooth pattern with depth 36 MHz about a central frequency $\overline{f}$. The resonance line as a function of τ_{EDSR} is shown in the inset of Figure 3(a). For equal microwave power at two different frequencies $\overline{f}$, the peak heights $\delta V_{\mathrm{QPC}}^{\mathrm{peak}}$ are plotted in Figure 3(a) (main panel). The two data sets are similar in turn-on time and saturation value; this is the case for frequencies up to $\overline{f} = 6$ GHz. From similar data (insets of Figure 3(b)), using theory to be described, we extract the dependence of the spin-flip rateΩ_R on microwave power P_{MW} shown in the main panel of Figure 3(b). Coherent Rabi-type oscillations in $\delta V_{\mathrm{QPC}}^{\mathrm{peak}}(\tau_{\mathrm{EDSR}})$ are not observed for any microwave power or magnetic field over the range measured.

The B-independence of the EDSR strength rules out spin-orbit mediated EDSR of the $\mathbf{k} - \boldsymbol{\sigma}$ type (either Dresselhaus or Rashba), for which the Rabi frequency is proportional to B [Rashba 1991; Golovach 2006; Nowack 2007]. This is in contrast to the results of [Nowack 2007], where the spin-orbit effect was found to dominate in a similar device to ours. A possible explanation is the device orientation relative to $\mathbf{B}$ and the crystal axes. In both our experiment and [Nowack 2007], the gate geometry suggests a dominant $\tilde{\mathbf{E}}(\mathbf{t})$

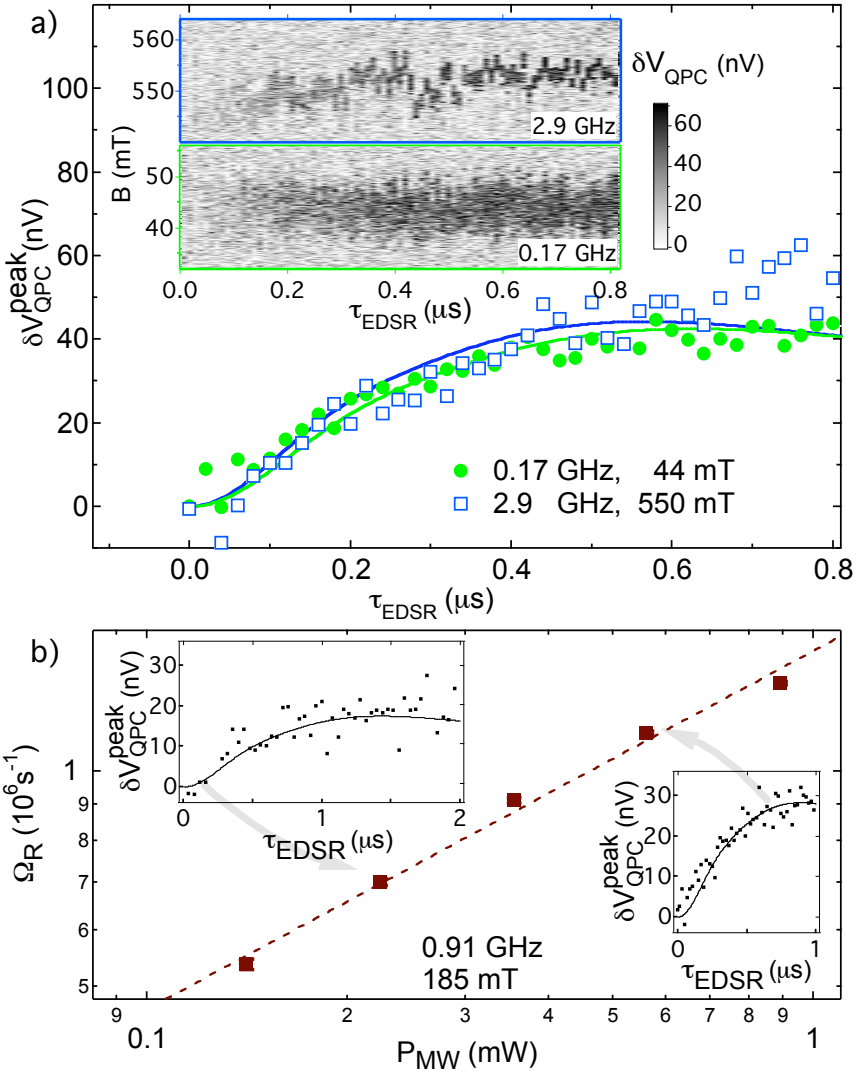

Figure 3.3: (a) Measured EDSR peak strength $\delta V_{\mathrm{QPC}}^{\mathrm{peak}}$ (symbols) versus microwave pulse duration τ_{EDSR} for two frequencies, along with theoretical fits (curves) obtained by numerically evaluating and scaling Equation (4) (see text). Both the applied power ($P_{\mathrm{MW}} \sim 0.6$ mW) and the calibrated power at the device are equal at these two frequencies (see footnote to Section 4.1). Inset: Raw data from which the points in the main figure are extracted. Each vertical cut corresponds to one point in the main figure. Jitter in the field position of the resonance reflects time-dependent Overhauser shifts. (b) Spin-flip rateΩ_R as a function of applied microwave power P_{MW}, along with a fit to the form$\Omega_R \propto \sqrt{P_{\mathrm{MW}}}$ (dashed line). Insets: $\delta V_{\mathrm{QPC}}^{\mathrm{peak}}$ versus τ_{EDSR} for two values of the microwave power, showing the fits from which points in the main figure are derived.

oriented along one of the diagonal axes ([110] or [1$\bar{1}$0]), leading to an in-plane spin-orbit effective field $\mathbf{B}_{\rm eff}^{\rm SO}$ perpendicular to $\tilde{\mathbf{E}}(\mathbf{t})$. In our geometry (see Figure 1(a)), this orientation of $\mathbf{B}_{\rm eff}^{\rm SO}$ is parallel to $\mathbf{B}$, and therefore ineffective at driving spin transitions. In the geometry of [Nowack 2007], $\mathbf{B}$ is perpendicular to $\mathbf{B}_{\rm eff}^{\rm SO}$, so that the $\mathbf{k}-\boldsymbol{\sigma}$ spin-orbit mechanism becomes more efficient.

Although the strength of the EDSR line is field-independent, the hyperfine-induced jitter becomes more pronounced with increasing field. As seen from the upper inset to Figure 3(a), repeated scans over the resonance at high field display larger fluctuations in the position of the peak center. This difference presumably reflects slower nuclear spin diffusion [Reilly 2007] as well as incipient polarization (see Section 5). In none of the data was any periodicity of the jitter detectible [Ono 2004].

3.4 Theory

A theoretical description of $\delta V_{\rm QPC}^{\rm peak}(\tau_{\rm EDSR})$ and its dependence on B and $P_{\rm MW}$ can be obtained by modeling EDSR as arising from the coupling of an electron in a single dot to an oscillating electric field $\tilde{\mathbf{E}}(t)$ and the hyperfine field of an ensemble of nuclei [2] [Laird 2007; Rashba 2008]. Then the center of the dot oscillates as $\mathbf{R}(t) = -e\tilde{\mathbf{E}}(t)/m\omega_0^2$, where m is the electron effective mass, and ω_0 is its confinement frequency in a parabolic dot. As a result, the Hamiltonian of the hyperfine coupling of the electron spin $\mathbf{S} = \boldsymbol{\sigma}/2$ with spatial coordinate $\mathbf{r}$ to nuclear spins $\mathbf{I}_j$ located at $\mathbf{r}_j$ becomes time dependent, $H_{\rm hf} = A\Sigma_j \delta(\mathbf{r}+\mathbf{R}(t)-\mathbf{r}_j)(\mathbf{I}_j\cdot\mathbf{S})$. Here A is the hyperfine coupling constant and the summation over j runs over all nuclear spins. After expanding $H_{\rm hf}$ in $\mathbf{R}(t)$ (assumed small compared to the dot size) and averaging over the orbital ground-state wave function $\psi_0(\mathbf{r})$ of the dot, the time dependent part of $H_{\rm hf}$ becomes $H_{\rm hf}(t) = \mathbf{J}(t)\cdot\boldsymbol{\sigma}$, where $\mathbf{J}(t)$ is an operator in all $\mathbf{I}_j$. Choosing the z-axis in spin space along $\mathbf{B}$, the components of $\mathbf{J}(t)$ are $J_z = \frac{1}{2}A\sum_j \psi_0^2(\mathbf{r}_j)I_j^z$ and

[2] There exists some physical similarity between the hyperfine mechanism of EDSR described in this chapter and EDSR due to the coupling of electron spin to a random exchange field in semimagnetic semiconductors [Khazan 1993].

$$J_{\pm}(t) = \frac{eA}{m\omega_0^2} \sum_j \psi_0(\mathbf{r}_j)\tilde{\mathbf{E}}(t) \cdot \nabla\psi_0(\mathbf{r}_j) I_j^{\pm}. \tag{3.1}$$

The time-dependent off-diagonal components $J_{\pm}(t)$ drive EDSR, while the quasi-static diagonal component J_z describes detuning of EDSR from the Larmor frequency ω_L by an amount ω_z randomly distributed as $\rho(\omega_z) = \exp(-\omega_z^2/\Delta^2)/(\Delta\sqrt{\pi})$ [Merkulov 2002]. The dispersions Δ of the detuning andΩ_R of the Rabi frequency are the root-mean-square values of J_z and $J_{\pm}$ respectively. Whereas J_z is dominated by fluctuations of $\mathbf{I}_j$ symmetric about the dot centre, $J_{\pm}$ is dominated by fluctuations antisymmetric in the $\tilde{\mathbf{E}}$ direction because $\tilde{\mathbf{E}} \cdot \nabla\psi_0(\mathbf{r})$ is odd with respect to the $\tilde{\mathbf{E}}$ projection of $\mathbf{r}$. Finally,

$$\Delta = \frac{A}{2\hbar}\sqrt{\frac{I(I+1)m\omega_0 n_0}{2\pi\hbar d}},\ \Omega_R = \frac{e\tilde{E}A}{\hbar^2\omega_0}\sqrt{\frac{I(I+1)n_0}{8\pi d}}, \tag{3.2}$$

with $I = 3/2$ for GaAs, n_0 the nuclear concentration, and d the vertical confinement. It is seen thatΩ_R is independent of B; this is in contrast to EDSR mediated by the conventional $\mathbf{k} - \boldsymbol{\sigma}$ spin-orbit coupling, where Kramers' theorem requires that the Rabi frequency vanish linearly as $B \to 0$ [Rashba 1991; Levitov 2003; Golovach 2006].

In an instantaneous nuclear spin configuration with detuning $\delta\omega = 2\pi f - (\omega_L + \omega_z)$ and Rabi frequency Ω, the spin-flip probability from an initial $\uparrow$ spin state is [Rabi 1937]:

$$p_{\downarrow}(\tau_{\mathrm{EDSR}}) = \frac{\Omega^2}{(\delta\omega/2)^2 + \Omega^2} \sin^2\left[\sqrt{(\delta\omega/2)^2 + \Omega^2}\ \tau_{\mathrm{EDSR}}\right]. \tag{3.3}$$

(We neglect the electron spin relaxation and nuclear-spin dynamics, which remain slow compared with the Rabi frequency even in the EDSR regime [Petta 2005; Rashba 2008].) To compare with the time-averaged data of Figure 3, we average Equation (3.3) over ω_z with weight $\rho(\omega_z)$ and over Ω with weight $\rho(\Omega) = 2\Omega\exp(-\Omega^2/\Omega_R^2)/\Omega_R^2$. This latter distribution arises because the $J_{\pm}$ acquire Gaussian-distributed contributions from both I_j^x and I_j^y components of the nuclear spins, hence it is two-dimensional. Averaging over ω_z and Ω results in a mean-field theory of the hyperfine-mediated EDSR. The resulting spin-flip

probability

$$\overline{p}_{\downarrow}(\tau_{\mathrm{EDSR}};\Delta,\Omega_R)=\int_{-\infty}^{+\infty}d\omega_z\,\rho(\omega_z)\int_{0}^{+\infty}d\Omega\,\rho(\Omega)p_{\downarrow}(\tau_{\mathrm{EDSR}}) \tag{3.4}$$

shows only a remnant of Rabi oscillations as a weak overshoot at $\tau_{\mathrm{EDSR}}\sim\Omega_R^{-1}$. The absence of Rabi oscillations is characteristic of hyperfine-driven EDSR when the measurement integration time exceeds the nuclear evolution time [Reilly 2007], and arises because $J_{\pm}$ average to zero.

3.4.1 Comparison with Data

To compare theory and experiment, the probability $\overline{p}_{\downarrow}(\tau_{\mathrm{EDSR}};\Delta,\Omega_R)$ is scaled by a QPC sensitivity V^0_{QPC} to convert to a voltage $\delta V^{\mathrm{peak}}_{\mathrm{QPC}}$. After scaling, numerical evaluation of Equation (4) gives the theoretical curves shown in Figure 3(a). The parameters that determine these curves are as follows: The Larmor frequency spread, $\Delta=2\pi\times 28$ MHz, is taken as the quadrature sum of the jitter amplitude seen in Figure 2 and half the frequency modulation depth, whereasΩ_R and V^0_{QPC} are numerical fit parameters. The 44 mT data (green curve in Figure 3(a)) give$\Omega_R=1.7\times10^6$ s^{-1} and $V^0_{\mathrm{QPC}}=2.4$ μV. Holding V^0_{QPC} to this value, the 550 mT data give$\Omega_R=1.8\times10^6$ s^{-1} (blue curve in Figure 3(a)) and the 185 mT data give the dependence ofΩ_R on microwave power P_{MW} shown in Figure 3(b). The Rabi frequencyΩ_R increases as $\sqrt{P_{\mathrm{MW}}}$ (Figure 3(b)) and is independent of B, both consistent with Equation (1). The B-independence ofΩ_R — also evident in the EDSR intensity in Figure 2—and the absence of Rabi oscillations support our interpretation of hyperfine-mediated EDSR in the parameter range investigated [3]

Estimating $\hbar\omega_0\sim 1$ meV [Hanson 2003], $\tilde{E}\sim 3\times10^3$ Vm^{-1} at maximum applied power [4], $d\sim 5$ nm, and using values from the literature $n_0=4\times10^{28}$ m^{-3} and An_0=90 μeV

[3] AlthoughΩ_{R} is found to be substantially smaller than the inhomogeneous dephasing rate $1/T_2^*\sim$ 100 MHz, oscillations would still be expected from a coherent process. Quasistatic dephasing processes, such as the hyperfine process dominant here, allow Rabi oscillations to persist even whenΩ T_2^* is considerably less than unity [Nowack 2007; Koppens 2007].

[4] The power at the device is calibrated separately at each frequency from the threshold for non-resonant lifting of spin blockade, which we take to indicate a microwave amplitude large enough to configure the dot

[Paget 1977] we calculate$\Omega_R \sim 11 \times 10^6$ s^{-1}, an order of magnitude larger than measured. The discrepancy may reflect uncertainty in our estimate of $\tilde{E}$.

We have neglected any effect of residual exchange in (1,1) during the ESR burst. From the width of the (1,1)-(0,2) charge transition, the interdot tunnel rate t_c is deduced to be much smaller than Boltzmann's constant multiplied by the electron temperature [Dicarlo 2004]. From the known (1,1)-(0,2) energy detuning ϵ with gate voltages configured at C, we estimate an upper bound on the (1,1) exchange $t_c^2/\epsilon \ll 80$ neV, of the same order as the hyperfine coupling. Since different choices of point C give qualitatively similar results, we conclude that (1,1) exchange is negligible.

Above, we generalized a mean-field description of the hyperfine interaction [Khaetski 2002; Merkulov 2002] to the resonance regime. Justification for this procedure was provided recently in [Rashba 2008]. A distinctive feature of the mean-field theory is a weak overshoot, about 10 - 15%, that is expected in the data of Fig. 3(a) before $\delta V_{\rm QPC}^{\rm peak}(\tau_{\rm EDSR})$ reaches its asymptotic value at $\tau_{\rm EDSR} \to \infty$. No overshoot is observed in the 550 mT data (blue symbols in Figure 3(a)), which was taken in a parameter range where an instability of the nuclear polarization begins to develop; see Section 5. For the 44 mT data (green symbols in Figure 3(a)), a considerable spread of experimental points does not allow a specific conclusion regarding the presence or absence of an overshoot. The theory of [Rashba 2008] suggests that the existence of the overshoot is a quite general property of the mean-field theory. However, after passing the maximum, the signal decays to its saturation value vary fast, with Gaussian exponent $e^{-\Omega_{\rm R}^2\tau_{\rm EDSR}^2}$. By contrast, the first correction to the mean-field theory decays slowly, as $1/(N\Omega_{\rm R}^2\tau_{\rm EDSR}^2)$, where N is the number of nuclei in the dot. As a result, the two terms become comparable at $\tau_{\rm EDSR} \sim \sqrt{\ln N}/\Omega_{\rm R}$, which should make the maximum less pronounced. Because for $N \sim 10^5$ the factor $\sqrt{\ln N} \sim 3$, the corrections to the mean-field theory manifest themselves surprisingly early, at times only about $\tau_{\rm EDSR} \approx 3/\Omega_R$, making the overshoot difficult to observe.

---

temporarily in a different charge state. This amplitude corresponds in Figure 1(b) to the 4mV distance from point C to the nearest charge transition. The data in Figure 3(a) and the last data point in Figure 3(b) use power 2 ± 1 dB below this threshold, corresponding to 3.2 mV. Dropped uniformly across the 500 nm width of the device this voltage gives a field $\tilde{E} \sim 3 \times 10^3$ Vm^{-1}.

3.5 Nuclear Polarization

Consistent with a hyperfine mechanism, this EDSR effect can create a non-equilibrium nuclear polarization [Baugh 2007]. If f is scanned repeatedly over the resonance at high power, a shift of the resonance develops (Figure 4(a)), corresponding to a nuclear spin alignment parallel to $\mathbf{B}$. The effect is stronger at higher B, and saturates over a timescale ~ 200 s. In Figure 4(b), we show how to build up a substantial polarization: While slowly increasing B, we scan f repeatedly downwards, i. e., in the direction which tracks the moving resonance. The resonance frequency remains approximately fixed, showing that the developing polarization compensates the increase in B. From the maximum line displacement from equilibrium, an effective hyperfine field of 840 mT can be read off, corresponding to a nuclear polarization of $\sim 16\%$. Figure 4(c) shows similar data for lower power and opposite frequency sweep direction, indicating the approximate equilibrium line position. Figure 4(d), similar to Figure 4(b) but with a faster sweep rate, makes the displacement and eventual escape of the resonance clearer although the maximum polarization is less.

The resonance shift is observed to be towards lower frequency, corresponding to a nuclear polarization parallel to $\mathbf{B}$. This can be understood if the pulse cycle preferentially prepares the electron ground state T_+ over T_-, either because it is more efficiently loaded or because of electron spin relaxation. EDSR then transfers this electron polarization to the nuclei [Rudner 2007]. We emphasize that the line shift is opposite to what is given by the usual Overhauser mechanism for inducing nuclear polarization via electron resonance [Overhauser 1953; Gueron 1959].

3.6 Addressing individual Spins

In quantum information applications, it is desirable to address individual spins selectively [Loss 1998]. A scheme to allow this is presented in Figure 5. In an otherwise similar device (Figure 5(a)), we incorporated a 100 nm thick micron-scale permalloy (84% Ni, 16% Fe) magnet over 35 nm of atomic-layer-deposited alumina [Tokura 2006; Pioro-Ladrière 2007]. This device was measured with external field $\mathbf{B}$ normal to the heterostructure plane. A finite-element simulation of the field $\mathbf{B}^{\mathrm{mag}}$ due to the micromagnet, assuming complete

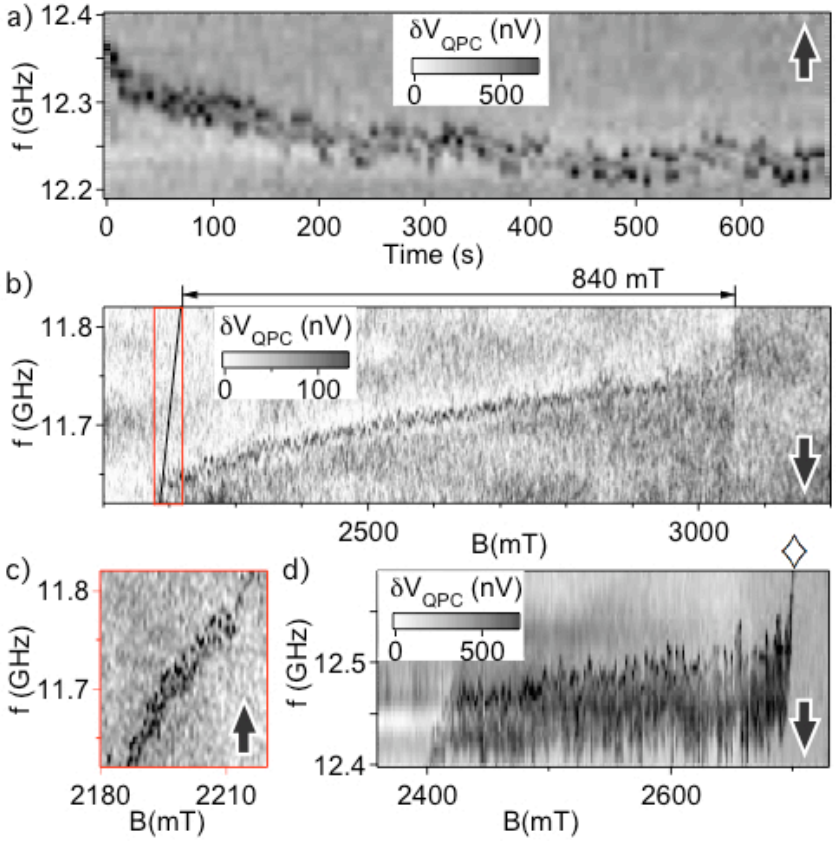

Figure 3.4: (a) Shift of the resonance frequency with time at constant $B = 2390$ mT, showing build-up of nuclear polarization over ~ 200 s. (b) A scheme to allow larger polarizations: the microwave frequency is repeatedly scanned over the resonance while B is swept upwards at 6 mT/min. Nuclear polarization partly counteracts B, moving the resonance away from its equilibrium position (black diagonal line) by up to 840 mT. (c) Similar data taken at lower microwave power and opposite frequency sweep direction, showing approximately the equilibrium resonance position. (Grey scale as in (b)). (d) Similar data as in (b), with faster sweep rate (22 mT/min), showing more clearly the displacement and subsequent return to equilibrium of the resonance. $\diamondsuit$ marks the escape of the resonance from the swept frequency window. In all plots, arrows denote frequency sweep direction.

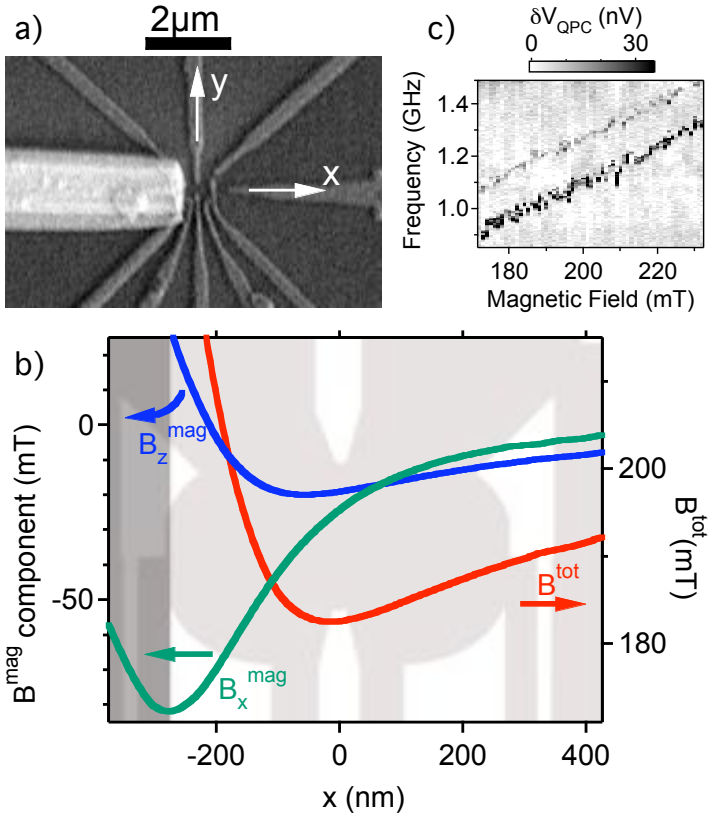

Figure 3.5: (a) A device similar to that of Figure 1, incorporating a micromagnet. (b) Total field magnitude B^{tot} (right axis) and the x and z components of the micromagnet contribution $\mathbf{B}^{\text{mag}}$ (left axis), simulated at $y = 0$ for external field $B = 200$ mT along $\hat{\mathbf{z}}$ (out of the plane). B_y^{mag} vanishes by symmetry. The gate layout is shown in the background. (c) The associated split EDSR line. The lower resonance is stronger, as expected if the left electron is confined close to the minimum of B_{tot}.

permalloy magnetization along $\mathbf{B}$, yields the field profiles shown in Figure 5(b). The difference in total field $B^{\rm tot} = |\mathbf{B} + \mathbf{B}^{\rm mag}|$ between dots is ~ 5 mT. As expected, the EDSR line measured in this device is frequently split (Figure 5(c)). The splitting, $10 - 20$ mT depending on precise gate voltage and pulse parameters, is not observed without the magnet and presumably reflects the field difference between dots. Since this splitting is considerably larger than the Overhauser field fluctuations, spins in left and right dots can be separately addressed by matching f to the local resonance condition [Pioro-Ladriere 2008].

The observation of a field difference between dots raises the possibility of EDSR driven by a field gradient [Pioro-Ladriere 2008]. We cannot exclude a contribution from this effect to the signal in Figure 5(c); however we did not observe the Rabi oscillations which would be expected if the field gradient were the primary EDSR mechanism.

3.7 Open Issues and Discussion

Finally, we discuss unexplained behavior observed only in the device of Figure 5(a). For the data described in this section, a simplified measurement scheme is used: Rather than applying gate pulses, the device is configured in the spin blockade region (point M in Figure 1(a)) throughout. Microwaves are applied continuously, and spin resonance is detected by directly measuring the QPC conductance $g_{\rm s}$.

As well as the EDSR signal at full frequency $f = g\mu_B B/h$, an unexpected half-frequency signal is sometimes seen (Figure 6.) Furthermore, depending on the exact gate configuration, both full-frequency and half-frequency signals can have either sign; the change in $g_{\rm s}$ at full frequency is usually negative as expected, but sometimes positive close to degeneracy of (1,1) and (0,2) charge configurations, where spin blockade is weakest [Koppens 2005]; by contrast, the change in $g_{\rm s}$ at half frequency is usually positive but sometimes negative far from degeneracy. For most gate configurations, full-frequency and half-frequency signals have opposite sign, as seen in Figure 6.

A half-frequency response is as far as we know unprecedented in spin resonance, and suggests second harmonic generation (SHG) from the microwave field. SHG is generally a non-linear phenomenon; it occurs for example in optical materials with non-linear polariz-

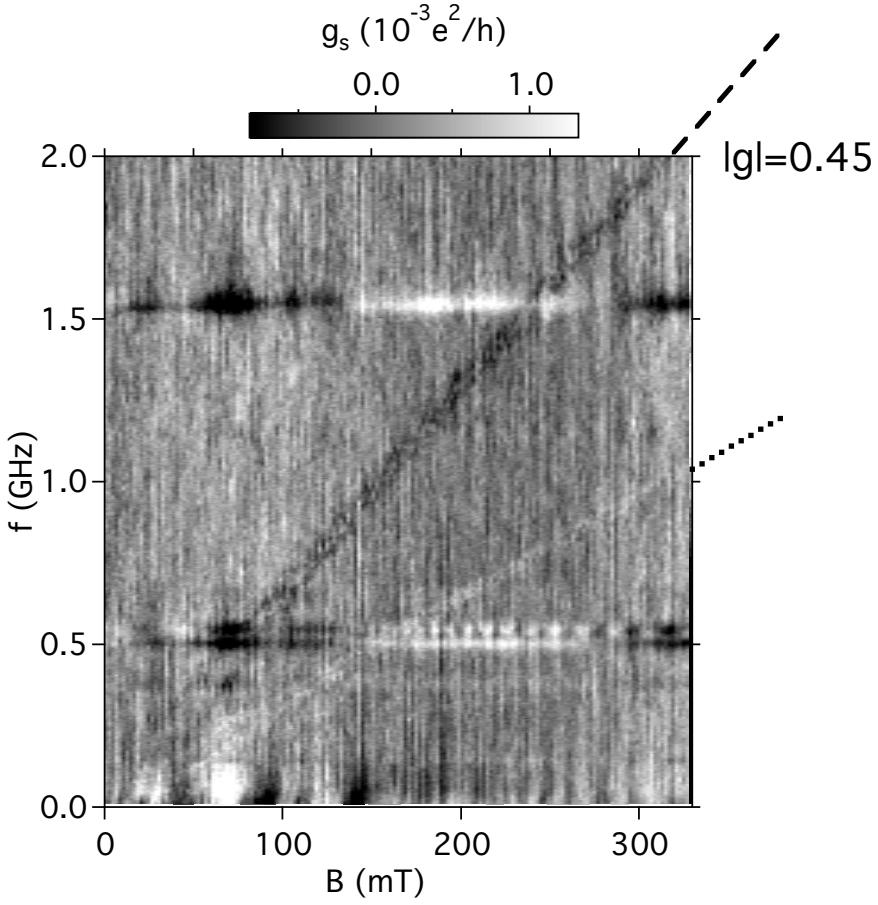

Figure 3.6: Spin resonance signal (measured in conductance) in the device of Figure 5(a). The EDSR signal shows up as a decrease in conductance as expected at frequency corresponding to $|g| = 0.45$ (marked with dashed line.) An additional signal of opposite sign appears at exactly half this frequency (dotted line). The larger splitting of both signals below 100mT is consistent with a greater contribution of B_x^{mag} to the total field difference between dots. The horizontal features at 0.5 and 1.5 GHz result from resonances of the microwave circuit. As in Figure 2, field- and frequency-independent backgrounds have been subtracted, including any signal due to spin blockade lifting around $B = 0$ [Koppens 2006].

ability [Franken 1961] and in non-linear electronic components. For hydrogenic donors in a semiconductor, the nonlinear dependence of g-tensor on electric field has been predicted to drive EDSR at subharmonics of the Larmor frequency [De 2009]. In our system, a hyperfine field at a harmonic of the microwave frequency arises if the confinement potential is non-parabolic.

However, SHG alone does not explain the sign of the conductance change seen at half-frequency in Figure 6. The positive signal would be consistent with a reduced admixture of (0,2), corresponding to a unexpected enhancement of the spin lifetime by microwaves. Alternatively, a positive signal could be caused by an admixture of the (0,1) charge state; but it is observed even for the gate configurations where (0,1) is energetically inaccessible (in the top right of the spin blockade region of Figure 1(b)). Also, there is no reason why (0,1) should be admixed for one resonance but not the other. These anomalous behaviours are therefore left unexplained.

Acknowledgements

We acknowledge useful discussions with Al. L. Efros, H.-A. Engel, F. H. L. Koppens, J. R. Petta, D. J. Reilly, M. S. Rudner, J. M. Taylor, and L. M. K. Vandersypen. We acknowledge support from the DTO and from DARPA. E. I. R. was supported in part by a Rutherford Professorship at Loughborough University, U.K.

Chapter 4

Rapid Single-Shot Measurement of a Singlet-Triplet Qubit

C. Barthel[1] D. J. Reilly[1,2] C. M. Marcus[1] M. P. Hanson[3] A. C. Gossard[3]

[1]Department of Physics, Harvard University, 17 Oxford Street, Cambridge, Massachusetts 02138, USA

[2]School of Physics, University of Sydney, Sydney, 2006, Australia

[3]Materials Department, University of California, Santa Barbara, California 93106, USA

We report repeated single-shot measurements of the two-electron spin state in a GaAs double quantum dot. The readout scheme allows measurement with fidelity above 90% with a ~ 7 μs cycle time. Hyperfine-induced precession between singlet and triplet states of the two-electron system are directly observed, as nuclear Overhauser fields are quasi-static on the time scale of the measurement cycle. Repeated measurements on millisecond to second time scales reveal evolution of the nuclear environment [1].

---

[1]This chapter is adapted from Ref. [Barthel 2009] with permission,

4.1 Introduction

Qubits constructed from spin states of confined electrons are of interest for quantum information processing [Loss 1998], for investigating decoherence and controlled entanglement, and as probes of mesoscopic nuclear spin environments. For logical qubits formed from pairs of electron spins in quantum dots [Levy 2002], several requirements for quantum computing [DiVincenzo 1998] have been realized [Petta 2005; Nowack 2007; Pioro-Ladriere 2008; Reilly 2008]. To date, however, measurements of these systems have constituted ensemble averages over time, while protocols for quantum control, including quantum error correction, typically require high-fidelity single-shot readout. Coherent evolution conditional on individual measurement outcomes can give rise to interesting non-classical states [Armen 2002; Romito 2008]. Rapidly repeated single-shot measurements can also give access to the dynamics of the environment, allowing, for instance, feedback-controlled manipulation of the nuclear state. Single-shot measurements of solid-state quantum systems have been reported for superconducting qubits [Astafiev 2004], the charge state of a single quantum dot [Lu 2003], the spin of a single electron in a quantum dot in large magnetic fields [Elzerman 2004; Amasha 2008], and the two-electron spin state in a single quantum dot [Meunier 2006].

In this chapter, we demonstrate rapidly repeated high-fidelity single-shot measurements of a two-electron spin (singlet-triplet) qubit in a double quantum dot. Singlet and triplet spin states are mapped to charge states [Petta 2005], which are measured by a radio-frequency quantum point contact (rf-QPC) that is energized only during readout. The measurement integration time required for $> 90\%$ readout fidelity is a few microseconds. On that time scale, nuclear Overhauser fields are quasi-static, leading to observed periodic precession of the qubit. By measuring over longer times, the evolution of the Overhauser fields from milliseconds to several seconds can be seen as well. We apply a model of single-shot readout statistics that accounts for T_1 relaxation, and find good agreement with experiment. Finally, we examine the evolution of the two-electron spin state at the resonance between the singlet (S) and the $m = +1$ triplet (T_+) via repeated single-shot measurement, and show that the transverse component of the Overhauser field difference is

not quasi-static on the time scale of data acquisition, as expected theoretically.

4.2 Device and System

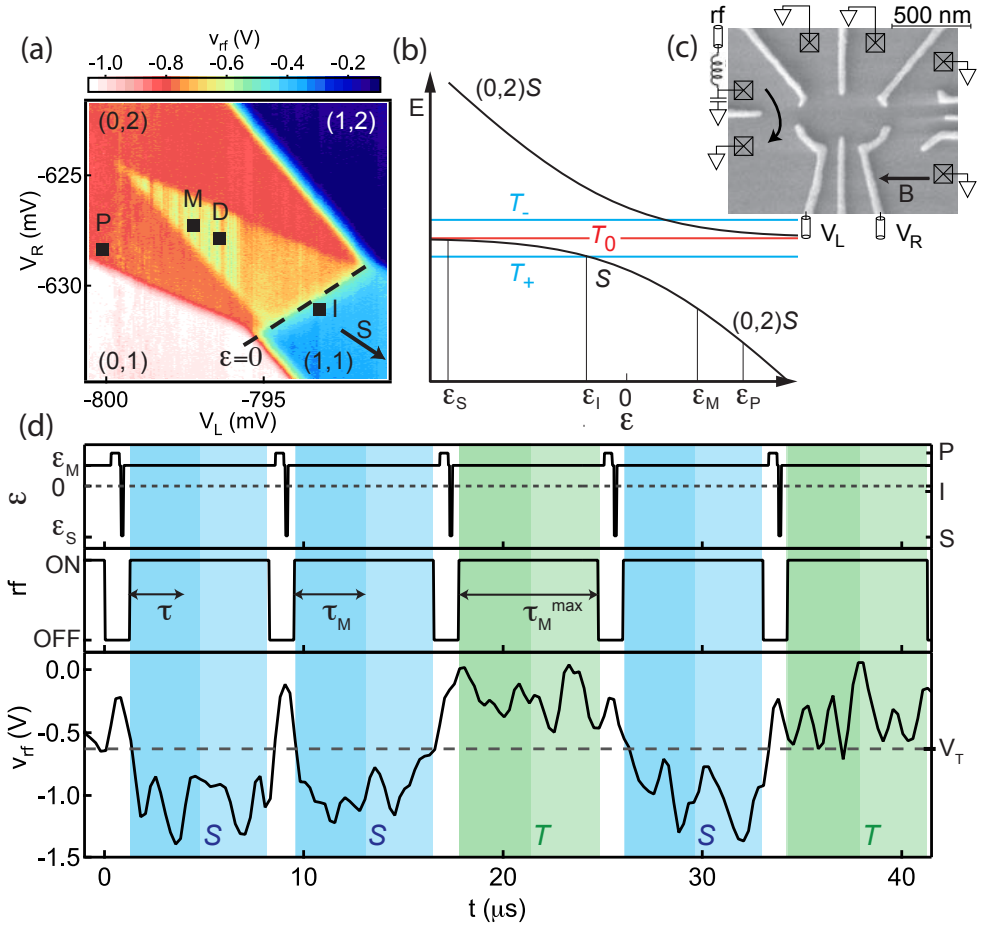

Figure 4.1: (a) Charge occupancy (left, right) of the double dot, detected using rf-QPC reflectometer voltage, $v_{\rm rf}$, in continuous-sensing mode [Reilly 2008] rather than single-shot readout. The yellow triangle in (0,2) indicates where charge state (1,1) is metastable. Markers indicate gate voltages used in single-shot mode. Preparation of $(0,2)$ singlet (P); separation for $S-T_0$ mixing (S) and $S-T_+$ mixing (I); measurement (M); operating point with 0 V pulse amplitude (D). (b) Two-electron energy levels as a function of detuning ϵ from (0,2) - (1,1) degeneracy. (c) Micrograph of device identical to measured device, indicating ohmic contacts (boxes), fast gate lines, reflectometry circuit, grounded contacts, and field direction. (d) Pulse-sequence of ϵ, controlled by $V_{\rm R}$ and $V_{\rm L}$, cycling through the points P, S, M. Sensor signal $v_{\rm rf}$ indicates triplet (T) or singlet (S) outcome for $\tau_{\rm S} = 100$ ns. Integration subinterval time $\tau_{\rm M}$ chosen in post-processing.

The double quantum dot is formed by Ti/Au depletion gates on a GaAs/$Al_{0.3}Ga_{0.7}As$ heterostructure with a two-dimensional electron gas (density 2×10^{15} m^{-2}, mobility 20 m^2/Vs)

100 nm below the surface. In order to split the three triplets, an in-plane magnetic field, B, larger than the typical Overhauser fields is applied along the line between dot centers. Except where noted, $B = 200$ mT. As described elsewhere [Reilly APL 2007], a proximal radio-frequency quantum point contact (rf-QPC) is sensitive to the charge state of the double dot, yielding an output signal $v_{\rm rf}$ via reflectometry, with sub-microsecond time resolution. The charge state of the double dot is controlled by fast-pulsed gate voltages $V_{\rm L}$ and $V_{\rm R}$ from two synchronized Tektronix AWG710B arbitrary waveform generators.

Energy levels of the system as a function of detuning, ϵ, from the (1,1) - (0,2) charge degeneracy (controlled by $V_{\rm R}$ and $V_{\rm L}$) are shown in Fig. 5.1(b). The qubit comprises the two-electron singlet (S) and $m = 0$ triplet (T_0) of the (1,1) charge state [Petta 2005]. A pulse cycle [Fig. 5.1(d)] first prepares a spin singlet in $(0, 2)$ by waiting at point P (near the edge of (0,2)) for $\tau_{\rm P} = 400$ ns, then moving to a separation point S (I), where S and T_0 (S and T_+) are nearly degenerate, for a time $\tau_{\rm S}$ ($\tau_{\rm I}$). Finally the system is brought to the measurement point M for a time $\tau_{\rm M}^{\rm max}$. If the separated electrons are in a singlet configuration when the system is pulsed to M, the system will return to $(0, 2)$, which will be detected by the rf-QPC. If the two electrons are in a triplet state, they will remain in $(1, 1)$ at point M, and detected accordingly. Coherent superpositions will be projected to the corresponding charge state during measurement. The rf-QPC is only energized during read-out, at point M [Fig. 5.1(d)].

4.3 Single-shot Measurement and Fidelity

The rf-QPC conductance is $\sim 5\%$ higher in (0,2) than in (1,1), yielding a charge sensitivity of 6×10^{-4} e/Hz$^{-1/2}$, i.e., unity signal-to-noise after 400 ns of integration. To increase fidelity, single-shot outcomes are averaged over a sub-interval $\tau_{\rm M}$ of the full measurement time $\tau_{\rm M}^{\rm max}$, $V_{\rm rf} = 1/\tau_{\rm M} \int_0^{\tau_{\rm M}} v_{\rm rf}(\tau) d\tau$. By designating a threshold voltage $V_{\rm T}$, outcomes can be classified as singlet for $V_{\rm rf} < V_{\rm T}$ or triplet otherwise. Optimization of $\tau_{\rm M}$ and $V_{\rm T}$ is described below.

Figure 4.2(a) shows 7000 consecutive one-shot measurements of the $S - T_0$ qubit with $\tau_{\rm S}$ ranging from 1 – 200 ns, stepped by ~ 6 ns every 200 cycles. For these data, the in-

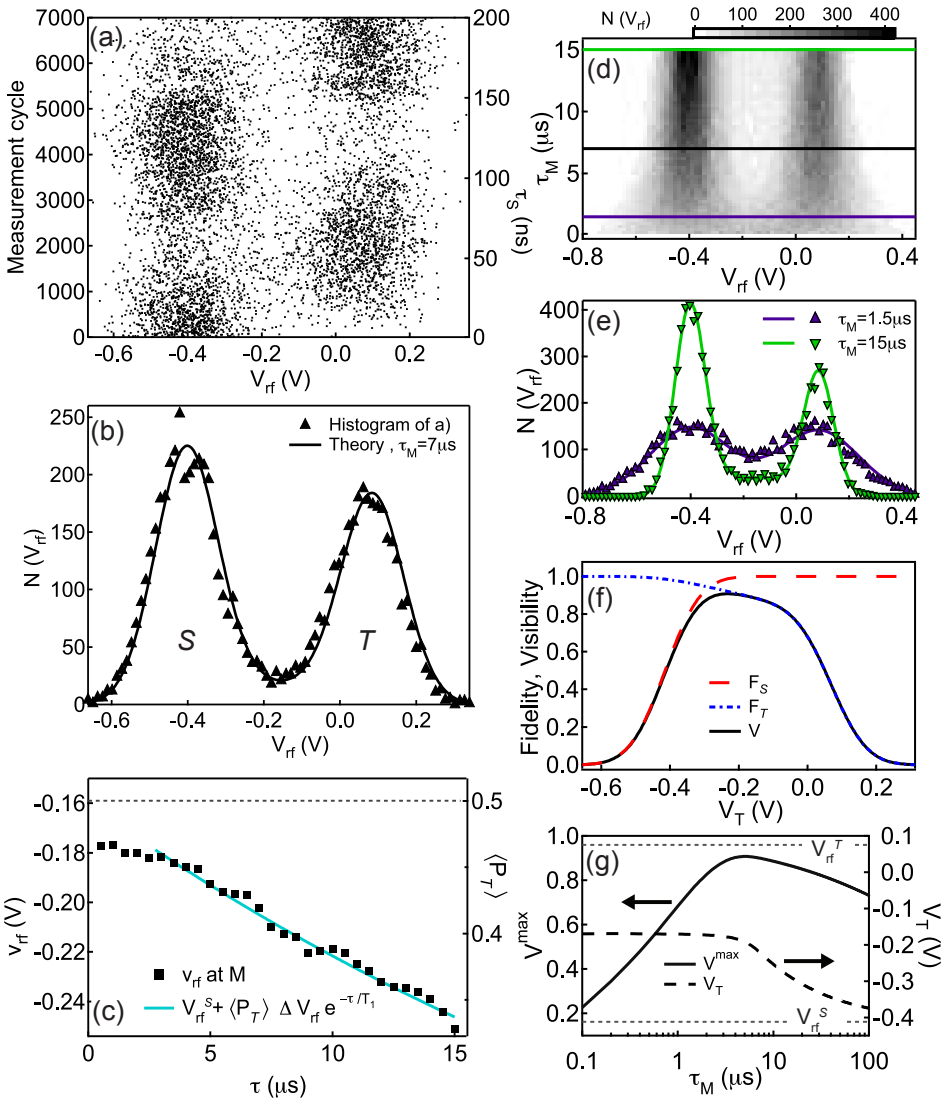

Figure 4.2: (a) 7000 consecutive single-shot measurements of $V_{\rm rf}$ using the pulse sequence in Fig. 5.1(d) with integration subinterval $\tau_{\rm M} = 7\ \mu$s and separation time, $\tau_{\rm S}$, incremented every 200 cycles. A background slope of $V_{\rm rf}$ with $\tau_{\rm S}$, due to a $\sim \mu$V gate voltage shift of point M with changing $\tau_{\rm S}$, is subtracted. The slope is determined from a control experiment with M outside the (1,1) - metastability region. (b) Histogram of the outcomes in (a), along with model (solid curve). Values for $V_{\rm rf}^S$ and$\Delta\ V_{\rm rf}$ are fit once using the 15 μs data in Fig. 5.2(e). The value $T_1 = 34\,\mu s$ and $\langle P_T\rangle = 0.5$ are from a fit to the relaxation data in Fig. 5.2(c). Note that $\langle P_T\rangle \sim 0.5$ is the theoretically expected value. (c) Instantaneous rf-QPC output $v_{\rm rf}(\tau)$ at time τ following pulsing to M, averaged over all cycles, along with a fit to the model, giving $T_1 = 34\,\mu$s. (d) Histograms $N(V_{\rm rf})$ (grayscale) for varying $\tau_{\rm M}$. (e) Horizontal cuts through d) along with model, with values of the parameters $V_{\rm rf}^S$, $V_{\rm rf}^T$ from a fit to the $\tau_{\rm M} = 15\ \mu$s data. (f) Fidelity of singlet, F_S, and triplet, F_T, and visibility $V = F_S + F_T - 1$ as a function of threshold, $V_{\rm T}$, for data in b). (g) Maximum visibility, $V^{\rm max}$, and optimal threshold, $V_{\rm T}$, as a function of measurement time, $\tau_{\rm M}$.

tegration subinterval, $\tau_{\rm M} = 7$ μs, was roughly half of the full measurement time, $\tau_{\rm M}^{\rm max} = 15$ μs. The histogram of single-shot outcomes (Fig. 5.2(b)), with voltage bin width $V_{\rm bin} \sim 10$ mV, is bimodal, with one peak at $V_{\rm rf}^S$, corresponding to the singlet ((0,2) charge state) outcome, and the other peak at $V_{\rm rf}^T$, corresponding to the triplet ((1,1) charge-state) outcome. The splittingΔ $V_{\rm rf} = V_{\rm rf}^T - V_{\rm rf}^S$ reflects the difference in output of the rf-QPC between (0,2) and (1,1) charge states, while the width, σ, of the two peaks reflects measurement noise [Reilly APL 2007]. However, the histogram is not simply the sum of two noise-broadened gaussians, because some states in (1,1) decay (with relaxation time T_1 [Johnson Nature 2005]) during the measurement subinterval. We model the full histogram $N(V_{\rm rf}) = N_{\rm tot}[n_S(V_{\rm rf}) + n_T(V_{\rm rf})]V_{\rm bin}$ as the sum of probability densities of singlet outcomes, $n_S(V_{\rm rf})$, and triplet outcomes, $n_T(V_{\rm rf})$, with $N_{\rm tot}$ the total number of measurements. The singlet probability density is modeled as a noise-broadened gaussian around $V_{\rm rf}^S$,

$$n_S(V_{\rm rf}) = (1 - \langle P_T \rangle)\, e^{-\frac{(V_{\rm rf} - V_{\rm rf}^S)^2}{2\sigma^2}} \frac{1}{\sqrt{2\pi}\sigma}, \tag{4.1}$$

where $\langle P_T \rangle$ is the triplet probability over all $N_{\rm tot}$ outcomes. Triplet outcomes, on the other hand, can take on values spread between $V_{\rm rf}^S$ and $V_{\rm rf}^T$ (and beyond, including measurement noise) to account for relaxation during the subinterval $\tau_{\rm M}$,

$$\begin{aligned} n_T(V_{\rm rf}) &= e^{-\tau_{\rm M}/T_1} \langle P_T \rangle\, e^{-\frac{(V_{\rm rf} - V_{\rm rf}^T)^2}{2\sigma^2}} \frac{1}{\sqrt{2\pi}\sigma} \\ &+ \int_{V_{\rm rf}^S}^{V_{\rm rf}^T} \frac{\tau_{\rm M}}{T_1} \frac{\langle P_T \rangle}{\Delta V_{\rm rf}} e^{-\frac{V - V_{\rm rf}^S}{\Delta V_{\rm rf}} \frac{\tau_{\rm M}}{T_1}} e^{-\frac{(V_{\rm rf} - V)^2}{2\sigma^2}} \frac{dV}{\sqrt{2\pi}\sigma}. \end{aligned} \tag{4.2}$$

The T_1 relaxation of the (1,1) triplet can be measured directly from the instantaneous rf-QPC output, $v_{\rm rf}(\tau)$, as a function of time τ following pulsing to point M (Fig. 5.2(c)). A fit of the ensemble-averaged rf-QPC output to the exponential form

$$v_{\rm rf}(\tau) = V_{\rm rf}^S + \langle P_T \rangle \Delta V_{\rm rf}\, e^{-\tau/T_1} \tag{4.3}$$

yields $\langle P_T \rangle = 0.5$ and $T_1 = 34\,\mu s$, using values for $V_{\rm rf}^S$ and$\Delta\ V_{\rm rf}$ determined from a fit of the $N(V_{\rm rf})$ model to the $\tau_{\rm M} = 15\ \mu$s histogram data [2], $V_{\rm rf}^S = -0.40$ V..

The tradeoff for optimizing the integration subinterval $\tau_{\rm M}$ is evident in Fig. 5.2(d), which shows histograms for a range of $\tau_{\rm M}$ from 0.25 μs to 15 μs. For short $\tau_{\rm M}$, the two peaks are blurred due to measurement noise; for long $\tau_{\rm M}$, the triplet peak loses strength due to relaxation. To optimize the readout, we first define fidelities, F_S and F_T, of pure singlet ($P_T = 0$) and pure triplet state ($P_T = 1$),

$$F_S = 1 - \int_{V_{\rm T}}^{\infty} n_S(V)dV,\ F_T = 1 - \int_{-\infty}^{V_{\rm T}} n_T(V)dV, \tag{4.4}$$

following Ref. [Elzerman 2004]. The integrals in Eq. (4.4) are the probabilities of misidentifying a pure singlet as a triplet and vice versa. Figure 2(f) shows these fidelities as well as the visibility,

$$V = F_S + F_T - 1, \tag{4.5}$$

for the $\tau_{\rm M} = 7\ \mu$s data [from Fig. 5.2(b)] as a function of the threshold voltage $V_{\rm T}$. For this value of $\tau_{\rm M}$, the maximum visibility, $\sim 90\%$, is achieved for $V_{\rm T}$ slightly less than the mean of $V_{\rm rf}^T$ and $V_{\rm rf}^S$ so that a triplet decaying towards the end of $\tau_{\rm M}$ still gets counted correctly. Optimal thresholds, $V_{\rm T}$, along with their associated maximum visibilities, $V^{\rm max}$, are plotted in Fig. 5.2(g) as a function of $\tau_{\rm M}$ using experimentally determined values for T_1, $V_{\rm rf}^T$, $V_{\rm rf}^S$, and $\sigma(\tau_{\rm M})$[2] [3]. The highest visibility, $\gtrsim 90\%$, is realized for $\tau_{\rm M} \sim 6\ \mu$s.

[2] For $\tau_{\rm M} = 1.5\ \mu$s, $\sigma = 152$ mV. For $\tau_{\rm M} = 7\ \mu$s, $\sigma = 82$ mV. For $\tau_{\rm M} = 15\ \mu$s, $\sigma = 56$ mV. σ is determined from the control experiment. A background slope of $V_{\rm rf}$ with $\tau_{\rm S}$, due to a $\sim \mu$V gate voltage shift of point M with changing $\tau_{\rm S}$, is subtracted. The slope is determined from a control experiment with M outside the (1,1) - metastability region. Other fit parameters:$\Delta\ V_{\rm rf} = 0.49$ V

[3] Values for $V_{\rm rf}^S$ and$\Delta\ V_{\rm rf}$ are fit once using the 15 μs data in Fig. 5.2(e). The value $T_1 = 34\,\mu s$ and $\langle P_T \rangle = 0.5$ are from a fit to the relaxation data in Fig. 5.2(c). Note that $\langle P_T \rangle \sim 0.5$ is the theoretically expected value.

4.4 Observation of Electron Spin Precession and nuclear Field Evolution

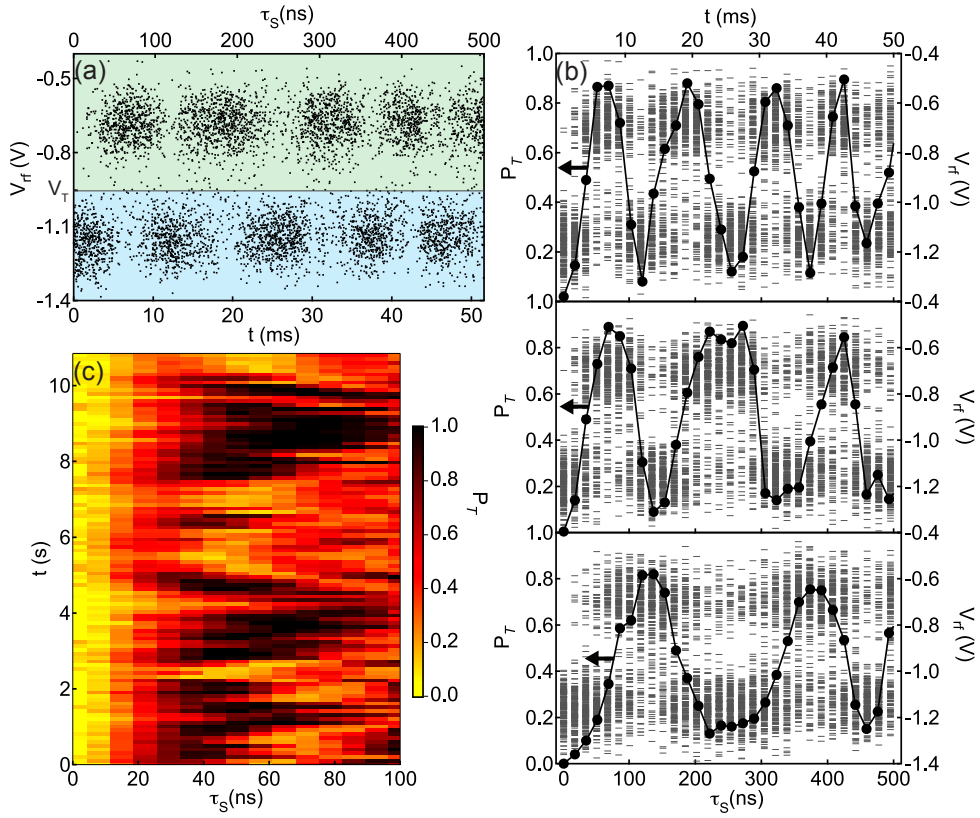

Figure 4.3: (a) 6000 consecutive single-shot $S - T_0$ measurements, $V_{\rm rf}$, with separation times $\tau_{\rm S}$ stepped by ~ 17 ns every 200 cycles, as a function of overall measurement time, t (bottom axis). Threshold $V_{\rm T}$ separates outcomes identified as singlet (blue) or triplet (green). Oscillations due to Overhauser fields are evident, with slightly evolving period. (b) Single-shot outcomes (gray markers) and triplet probabilities, P_T, (black circles) over $\tau_{\rm S}$, for three nominally identical runs taken 10 minutes apart. (c) Rapid acquisition of 108 P_T traces at times t. Probabilities P_T are determined from 400 measurements per $\tau_{\rm S}$.

Previous work using continous charge sensing showed inhomogenous dephasing of the $S-T_0$ qubit, which was attributed to precession with a broad frequency spectrum, driven by the fluctuating Overhauser field difference between the two dots [Petta 2005; Taylor PRB 2007]. For sufficiently fast single-shot repetition, Overhauser fields remain quasi-static over many single-shot measurements, leading to periodic $S-T_0$ precession, as seen in Fig. 5.3(a). Also evident is a variation of the precession period over ~ 50 ms, reflecting the slowly evolving

nuclear environment, consistent with previous measurement and theory [Reilly 2007].

Variation in the $S-T_0$ precession period is more clearly demonstrated in Figs. 5.3(b,c). Figure 3(b) shows three sets of precession data taken 10 minutes apart. Periods of the oscillating triplet probability, P_T, defined by the average of 400 binary outcomes (either S or T_0), correspond to longitudinal Overhauser field differences$\Delta\ B_z^{\rm nuc} = 1.3, 1.1, 0.4$ mT (top to bottom). The continuous evolution of the nuclear environment can be seen in Fig. 5.3(c), which shows P_T as a function of separation time $\tau_{\rm S}$—each row comparable to a panel in Fig. 5.3(b), but for $\tau_{\rm S}$ up to 100 ns rather than 500 ns—in slices taken every 100 ms [4]. The meandering light-dark pattern reflects the random evolution of the $S-T_0$ precession period on a ~ 1 s time scale, consistent with dipole-dipole mediated nuclear diffusion [Reilly 2007].

4.5 Ensemble Average, T_2^*

Assembling $P_T(\tau_{\rm S})$ statistics from single-shot measurements as a function of separation time $\tau_{\rm S}$ yields a time-averaged curve from which an inhomogeneous dephasing time T_2^* can be extracted [Petta 2005; Taylor PRB 2007]. Each point in Fig. 4.4(a) is an average over 1600 triplet-state return probabilities, each derived from 400 binary single-shot measurements. The individual $P_T(\tau_{\rm S})$ measurements are separated in time by ~ 20 s. A fit to the theoretical gaussian form,

$$P_T(\tau_{\rm S}) = P_T(0) + (V/2)[1 - e^{-(\tau_{\rm S}/T_2^*)^2}], \tag{4.6}$$

yields $T_2^* = 27$ ns, consistent with previous results [Petta 2005; Reilly 2007], visibility $V = 0.28$, and intercept $P_T(0) = 1 - F_S = 0.08$. These values yield a reasonable singlet fidelity, $F_S = 0.92$, but relatively low triplet fidelity $F_T = 0.36$ for this data (compared to Figs. 5.2,5.3) due to a short T_1 in this run.

[4] Each P_T value (pixel) in Fig. 5.3(c) is based on 1000 single-shot measurements. Each row of 15 probabilities is acquired in 80 ms, followed by 20 ms of dead time. For these measurements, $B = 100$ mT.

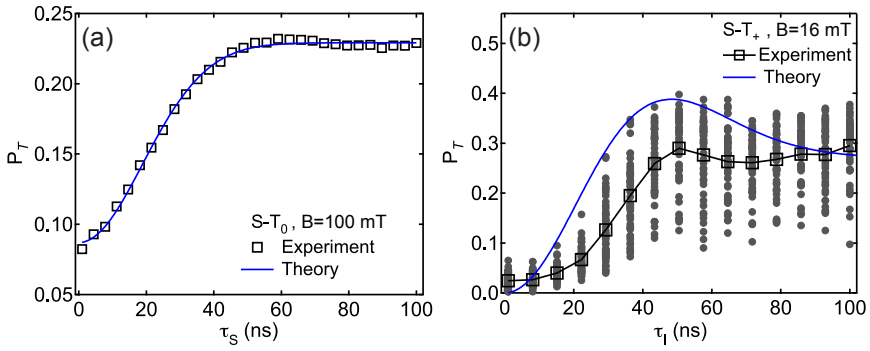

Figure 4.4: (a) Triplet probability P_T as a function of separation time $\tau_{\rm S}$ based on 1600 single-shot measurements per separation time. Fit (blue curve) gives $T_2^* = 27$ ns, $P_T(0) = 1 - F_S = 0.08$, $V = 0.28$ (see text). (b) P_T as a function of separation time $\tau_{\rm I}$ to the $S - T_+$ anticrossing at point I. Probabilities (gray circles) based on 400 single-shot binary measurements. At each $\tau_{\rm I}$, 50 values of P_T are taken 15 s apart and averaged (open black squares). Theory curve, Eq. (6), yields $B^{\rm nuc} = 0.7$ mT ($T_2^* = 37$ ns), with relatively poor agreement between experiment and theory (see text).

4.6 Fast Measurement of Spin Exchange between Electron Qubit and nuclear Bath

Finally, we investigate the triplet probability P_T after separating (0,2) singlets to the point I, where the (1,1) singlet state S crosses the T_+ triplet [see Fig. 5.1(b)]. Whereas mixing of S and T_0 at point S relies on the component of the Overhauser field difference *along* the total field direction, mixing of S and T_+ at point I relies on the component of the Overhauser field difference *transverse* to the total field. Evolution of transverse Overhauser fields are not inhibited by nuclear or electron Zeeman energy differences, and is relatively fast, set by nuclear dipole-dipole (~ 100 μs) and Knight-shift (~ 10 μs) energetics [Taylor PRB 2007; Taylor Thesis 2007; Reilly 2007; Hanson 2007]. As expected, we do not observe periodic precession between S and T_+. We note a variation over the course of the measurement in spin-flip probability at a fixed $\tau_{\rm I}$ and separation point I. This is likely due to changes in the position of the narrow $S - T_+$ resonance resulting from a small build-up of nuclear polarization during the measurement [Taylor Thesis 2007; Petta 2008].

Figure 4.4(b) shows probabilities P_T for the T_+ state as a function of $\tau_{\rm I}$. Each probability value (gray circle) in Fig. 4.4(b) is based on 400 binary single-shot measurements with $\tau_{\rm M} = 8$ μs. Series of $P_T(\tau_{\rm I})$ measurements were made over a range of $\tau_{\rm I}$ up to ~ 100 ns,

with an acquisition time ~ 50 ms per series. A total of 50 series, spaced by ~ 15 s to allow decorrelation of longitudinal Overhauser fields, were then averaged to give the black squares in Fig. 4.4(b).

At small external fields, when the $S - T_+$ anticrossing is in (1,1), the probability of detecting a triplet following separation for a time $\tau_{\rm I}$ can be written

$$P_T = P_T^0 + V \int d^3\mathbf{B}\, \rho(\mathbf{B})[(\Delta B_{\rm x}^2 + \Delta B_{\rm y}^2)/2(\hbar\omega/|g^*\mu_B|)^2] \sin^2(\omega\tau_{\rm I}), \tag{4.7}$$

where

$$\omega = |g^*\mu_B|/(2\hbar)[B_{\rm z}^2 + 2(\Delta B_{\rm x}^2 + \Delta B_{\rm y}^2)]^{1/2} \tag{4.8}$$

is the precession rate between S and T_+ at the center of the anticrossing,

$$\Delta B_{\rm x(y)} = [B_{\rm x(y)}^L - B_{\rm x(y)}^R]/2 \tag{4.9}$$

are transverse Overhauser field differences between left (L) and right (R) dots,

$$B_{\rm z} = [B_{\rm z}^L + B_{\rm z}^R]/2 \tag{4.10}$$

is the average longitudinal Overhauser field, V is readout visibility, and $g^* = -0.44$ is the effective electron g factor in GaAs. Assuming Overhauser fields $\mathbf{B} = (\ \Delta B_{\rm x}, \Delta B_{\rm y}, B_{\rm z})$ are gaussian distributed on long time scales,

$$\rho(\mathbf{B}) = (2\pi B^{\rm nuc})^{-3/2} e^{-(\mathbf{B}/B^{\rm nuc})^2/2}, \tag{4.11}$$

yields the form in Fig. 4.4(b) [5]. Setting $P_T^0 = 1 - F_S = 0$ and $B^{\rm nuc}$ to match the overshoot in the data yields $B^{\rm nuc} = 0.7$ mT $\sim \hbar|g^*\mu_B T_2^*|^{-1}$, corresponding to $T_2^* \sim 40$ ns, and $V = F_T \sim 0.7$. Unlike Fig. 4.4(a), theory and experiment do not match well for the $S - T_+$

[5] This form is expected to apply at low applied magnetic field, where the $S - T_+$ anticrossing is in (1,1). See Eqs. (7.1)-(7.3) in Ref. [Taylor Thesis 2007]. See EPAPS Document No. E-PRLTAO-103-020943 or Appendix D for a derivation of this equation.

mixing, due in part to the the buildup of average nuclear polarization, which shifts the $S - T_+$ resonance and lowers P_T.

Acknowledgments

We acknowledge support from IARPA/ARO, and the Department of Defense. Devices were made at Harvard's Center for Nanoscale Systems (CNS), a member of the NSF National Nanotechnology Infrastructure Network (NNIN). We thank J. M. Taylor and E. A. Laird for useful discussion, and J. Waissman for technical assistance.

Chapter 5

Fast Sensing of Double Dot Charge Arrangement and Spin State with an RF Sensor Quantum Dot

C. Barthel[1] M. Kjærgaard[1,2] J. Medford[1] M. Stopa[1] C. M. Marcus[1] M. P. Hanson[3] A. C. Gossard[3]

[1]Department of Physics, Harvard University, Cambridge, Massachusetts 02138, USA

[2]Nano-Science Center, Niels Bohr Institute, University of Copenhagen, Universitetsparken 5, DK-2100 Copenhagen, Denmark

[3]Materials Department, University of California, Santa Barbara, California 93106, USA

Single-shot measurement of the charge arrangement and spin state of a double quantum dot are reported, with measurement times down to ∼100 ns. Sensing uses radio-frequency reflectometry of a proximal quantum dot in the Coulomb blockade regime. The sensor quantum dot is up to 30 times more sensitive than a comparable quantum point contact sensor, and yields three times greater signal to noise in rf single-shot measurements. Numerical modeling is qualitatively consistent with experiment and shows that the improved sensitivity of the sensor quantum dot results from reduced screening and lifetime broadening [1].

---

[1]This chapter is adapted from Ref. [Barthel SQD 2010] with permission,

5.1 Introduction

Experiments on few-electron quantum dots [Hanson 2007], including spin qubits, have benefitted in recent years from the use of proximal charge sensing, a technique that allows the number and arrangement of charges confined in nanostructures to be measured via changes in conductance of a nearby sensor to which the device of interest is capacitively coupled [Field 1993; Ihn 2009]. Quantum point contacts (QPCs) have been widely used as charge sensors, allowing, for instance, high-fidelity single-shot readout of spin qubits via spin-to-charge conversion [Elzerman 2004; Barthel 2009]. Single electron transistors (SETs) based on metallic tunnel junctions, and gate defined sensor quantum dots (SQD), conceptually equivalent to SETs, have also been widely used as proximal sensors, and provide similar sensitivity and bandwidth [Schoelkopf 1998; Buehler 2005; Lu 2003; Fujisawa 2004]. As a typical application, measuring the state of a spin qubit via spin-to-charge conversion involves determining whether two electrons in a double quantum dot are in the $(1,1)$ or the $(0,2)$ charge configuration, where (left, right) denotes occupancies in the double dot [Fig. 1(a)], on time scales faster than the spin relaxation time [Barthel 2009].

In this chapter, we demonstrate the use of a sensor quantum dot for fast charge and two-electron spin-state measurement in a GaAs double quantum dot, biased near the (1,1)-(0,2) charge transition. We compare the performance of the SQD to conventional quantum point contact (QPC) sensors for dc and radio-frequency (rf) measurement. We find experimentally that the SQD is up to 30 times more sensitive, and provides roughly three times the signal to noise ratio (SNR) of a comparable QPC sensor for detecting the charge arrangement and spin state of a double quantum dot. Numerical simulations, also presented, give results consistent with experiment and elucidate the role of screening in determining the sensitivity of these proximal charge sensors.

5.2 Device and Measurement Setup

Double quantum dots with integrated sensors are defined by Ti/Au depletion gates on a $GaAs/Al_{0.3}Ga_{0.7}As$ heterostructure with a two-dimensional electron gas (density 2×10^{15} m^{-2}, mobility 20 m^2/Vs) 100 nm below the surface. The charge state of the double

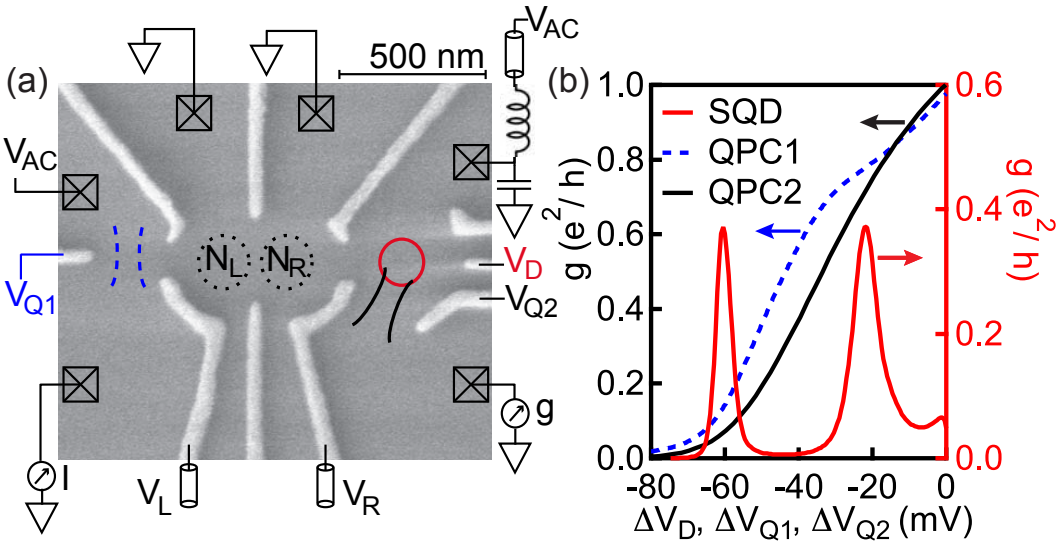

Figure 5.1: (Color online) (a) Micrograph of lithographically identical device. Gate voltages $V_{\rm L}$ and $V_{\rm R}$ control the double dot charge state $(N_{\rm L}, N_{\rm R})$ (see Fig. 5.2). Quantum point contact QPC1 (blue, dashed) controlled by gate voltage $V_{\rm Q1}$, sensor quantum dot (SQD) (red, solid), by plunger gate $V_{\rm D}$, can also be operated as a point contact (QPC2) (black, solid) apply gate voltage $V_{\rm Q2}$ to the bottom gate with top two grounded. QPC1(2) and SQD measured by dc transport in first device. SQD measured by rf reflectometry in subsequent cooldown of second identical device. (b) DC conductance, g, of QPC1,2 (left scale) and SQD (right scale) as a function of gate voltage changesΔ $V_{\rm D}$, $\Delta V_{\rm Q1}$, andΔ $V_{\rm Q2}$.

quantum dot is controlled by gate voltages $V_{\rm L}$, $V_{\rm R}$ [see Fig. 1(a)]. Three gates next to the right dot form the SQD, which is operated in the multi-electron Coulomb blockade (CB) regime, with center gate voltage $V_{\rm D}$ setting the SQD energy. A single gate next to the left dot forms a QPC sensor (denoted QPC1) whose conductance is controlled by gate voltage $V_{\rm Q1}$. A second QPC sensor (QPC2) results when the center and top gate voltages of the SQD are set to zero, with only the bottom gate set to $V_{\rm Q2}$.

Measurements were carried out in a dilution refrigerator at electron temperature $\sim$ 150 mK, configured for high-bandwidth gating, rf reflectometry and low-frequency (dc) transport. Low-frequency conductance was measured using a voltage bias of $\sim$ 50 μV at 197 Hz with a lock-in time constant of 100 ms. Two nominally identical devices were measured and showed similar behavior. In the first device, dc sensing was measured in QPC1, QPC2 and the SQD, along with single-shot rf reflectometry data for QPC1. The single-shot data for QPC1 in this device was discussed in detail in Ref. [Barthel 2009]. In the second device, single-shot rf reflectometry [Barthel 2009] for the SQD was measured.

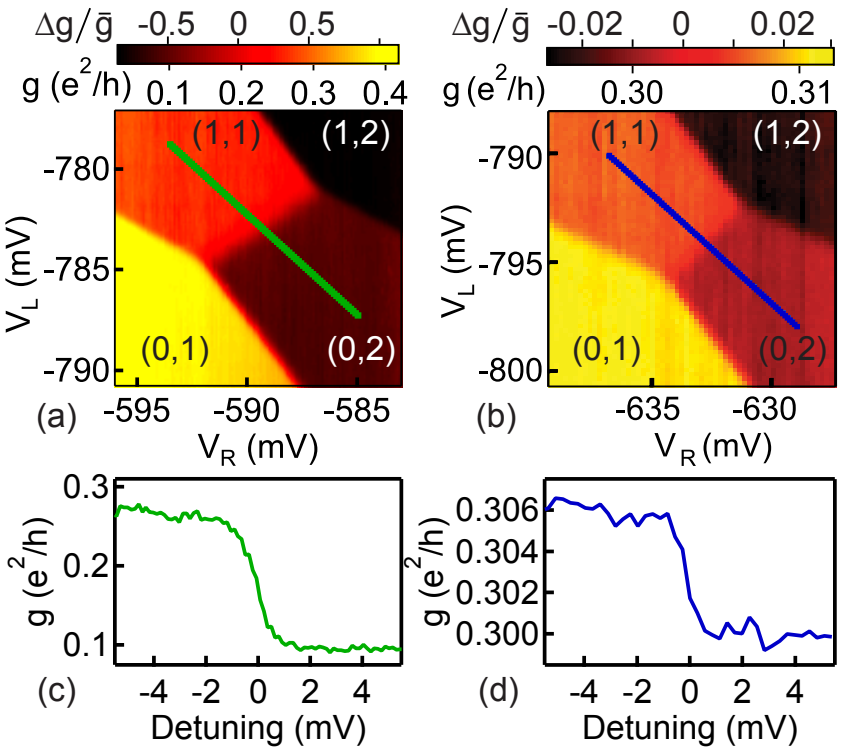

Figure 5.2: (Color online) (a) Sensor quantum dot (SQD) dc conductance g as a function of voltages $V_{\rm L}$ and $V_{\rm R}$, with charge occupancy $(N_{\rm L}, N_{\rm R})$ indicated. Note the large relative change in conductance,$\Delta\ g/\bar{g} \sim 0.9$ as double dot switches from (0,2) to (1,1). (b) QPC2 conductance shows a small ($\Delta g/\bar{g} \sim 3\%$) change as the dot switches from (0,2) to (1,1). A similar value is seen for QPC1 (not shown). (c, d) Cuts through (a), (b) respectively. All data is for Device 1.

5.3 DC Sensitivity

Conductance of the SQD shows CB peaks as a function of plunger gate voltage,$\Delta\ V_{\rm D}$, while conductances of QPC1 and QPC2 decrease smoothly, with $\sim 10\times$ lower maximum slope, as gate voltages$\Delta\ V_{\rm Q1(Q2)}$ are made more negative [Fig. 1(b)]. The greater slope of the SQD conductance versus gate voltage, compared to the QPC, is closely related to its higher sensitivity as a charge sensor (though not quantitatively, as lever arms to gates and dots differ). With $V_{\rm D}$ set on the side-wall of a CB peak, dc conductance of the SQD as a function of $V_{\rm L}$ and $V_{\rm R}$ indicates the charge state of the double dot [Fig. 2(a)]. Parasitic gating of the SQD is compensated by trimming $V_{\rm D}$ and $V_{\rm Q2}$ as $V_{\rm L}$ and $V_{\rm R}$ are swept, to keep the SQD conductance roughly constant on plateaus of fixed double dot charge arrangement. SQD conductance, centered around $\bar{g} = (g_{(1,1)} + g_{(0,2)})/2 \sim 0.2$ e^2/h, changes

byΔ $g_{\rm SQD} \sim 0.2$ e^2/h when the double dot charge arrangement changes from $(0,2)$ to $(1,1)$ (Fig. 2(c),. Figure 2(d) shows corresponding [2] changes in QPC2 conductance, which changes byΔ $g_{\rm QPC2} \sim 0.01$ e^2/h around $\bar{g} \sim 0.3$ e^2/h for the same charge rearrangement, consistent with values in the literature. The ratio of conductance changes,Δ $g_{\rm SQD}/\Delta g_{\rm QPC2} \sim 30$, is a measure of the relative sensitivity of SQD and QPC2 to the double dot charge state.

5.4 Fast Single-shot Measurements

To demonstrate fast measurement of a spin qubit via spin-to-charge conversion, the SQD is configured as the resistive element in an rf reflectometry circuit [Reilly APL 2007], following Ref. [Barthel 2009], and biased via V_D on the sidewall of a CB peak. The reflected rf amplitude, $v_{\rm rf}$, tracks SQD conductance. Gate pulses applied to $V_{\rm L}$ and $V_{\rm R}$ first prepare the ground state singlet in $(0,2)$, then separate the spins by moving to point S, deep in $(1,1)$, for a time $\tau_{\rm S} = 1-200$ ns [3], allowing precession between $(1,1)S$ and $(1,1)T_0$ driven by hyperfine fields, then move to the measurement point M in (0,2) for $\tau_{\rm M}^{\rm max} = 5$ μs (Fig. 2(a) and Ref. [Barthel 2009]). At M, only the singlet configuration of the two spins can rapidly move to the (0,2) ground state; spin triplets remain trapped in $(1,1)$ for the spin relaxation time [Barthel 2009].

With rf excitation applied to the SQD only during the measurement interval at point M, the reflectometry signal, $v_{\rm rf}$, is digitally integrated over a subinterval of duration $\tau_{\rm M}$ to yield a single-shot measurement outcome $V_{\rm rf}$. From histograms of 3×10^4 $V_{\rm rf}$ measurements (with 0.7 mV binning), probabilities, P, of single-shot outcomes can be estimated for each value of $\tau_{\rm M}$. As seen in Figs. 3(a,b), measurement noise decreases with increasing integration time, allowing distinct peaks—indicating singlet [i.e., (0,2)] and triplet [i.e., (1,1)] outcomes—to be distinguished for $\tau_{\rm M} > 100$ ns. The difference between singlet and triplet output voltages,

[2] Adjusting $V_{\rm Q2}$ and $V_{\rm D}$ to switch between a QPC and a SQD, shifts the charge stability diagram by ~ 30 mV.

[3] The separation time $\tau_{\rm S}$ is stepped from 1 to 200 ns, every 1000 cycles for a total of 30,000 cycles.

the signal

$$\Delta V = V_{\rm rf}^T - V_{\rm rf}^S \tag{5.1}$$

reflects the rf sensitivity of the SQD to the single-charge motion from (1,1) to (0,2).

Experimental $P(V_{\rm rf})$ curves for the SQD are in good agreement with theoretical models [Barthel 2009], as shown in Fig. 3(b). Fits of the model give values for the spin relaxation time, $T_1 = 13$ μs, the mean triplet probability, $\langle P_T \rangle = 0.46$, the peak width, $\sigma_{\rm rf}$, and the peak positions, $V_{\rm rf}^S$ and $V_{\rm rf}^T$. The resulting signal to noise ratio,

$$\mathrm{SNR} = \Delta \mathrm{V}/\sigma_{\rm rf} \tag{5.2}$$

is shown in Fig. 3(c) as a function of $\tau_{\rm M}$, along with the SNR for QPC1. A direct comparison must take into account that the SQD data in all panels of Fig. 3 used -99 dBm applied rf power ($\sim$ 0.15 mV), while the QPC1 data in Fig. 3(c) used -89 dBm applied rf power ($\sim$ 0.45 mV), values chosen to maximize the SNR for each. For both QPC1 and SQD, the output signal$\Delta\, V$ saturated at higher powers, due in part to broadening of the conductance features due to heating and finite bias.

SNR for both the SQD and QPC1 improve with increasing integration time, as shown in Fig. 3(c). Fitting the measured SQD signal to noise ratios to the form Eq. 5.2, with

$$\sigma_{\rm rf} = \sigma_0 \sqrt{1\mu\mathrm{s}/(\tau_{\rm M} + \tau_0)}, \tag{5.3}$$

yields an intrinsic integration time, $\tau_0 = 190$ ns, due to the $\sim$ 1.5 MHz bandwidth of the reflectometry circuit, a signal,$\Delta\, V_{\rm SQD} = 33$ mV, and a characteristic width, $\sigma_0 = 5$ mV, the measurement noise for one microsecond total integration time. The ratio$\Delta\, V/\sigma_0$ represents a characteristic SNR, which is 6.6 for this SQD. A similar measurement of the characteristic SNR for QPC1, at 10 dB higher applied rf power, yields a value 2.2 [4], with $\Delta V_{\rm QPC1} = 10$ mV and $\sigma_0 = 4.5$ mV.

[4]For QPC1 in Ref. [Barthel 2009], the fit parameters for the histograms, are $T_1 = 34$ μs, $\tau_0 = 700$ ns, and $\langle P_T \rangle \sim 0.5$.

For both SQD and QPC1, analysis [Korotkov 1999] predicts signals,$\Delta\ V$, consistent with measured values, and widths, σ_0, due to shot noise that are considerably lower than the measured peak widths. Specifically, $\sigma_0 \sim 1.5(3)$ mV and ~ 3 mV are expected for SQD (QPC1) [5]. This is roughly one tenth (half) of the total noise for the SQD (QPC1). The remaining measurement noise for both sensors is due to charge-, gate- and instrumentation noise, predominantly from the cryogenic amplifier[5] [Reilly APL 2007]. We conclude, based on the single-shot data, that the measured SQD offers improved SNR compared to a comparable QPC sensor, $\mathrm{SNR_{SQD}}/\mathrm{SNR_{QPC1}} \sim 3$. The improvement is not as large as the relative improvement in sensitivity at dc,$\Delta\ g_{\mathrm{SQD}}/\Delta g_{\mathrm{QPC1}} \sim 10$, mainly due to a lower rf power saturation of the SQD SNR and the experimental noise floor of the measurement setup.

5.5 Numerical Simulation

To investigate QPC and SQD performance numerically, we consider the sensitivity, s, as the change in conductance in response to a change in voltage, either applied to a gate or arising from a charge rearrangement. Modeling the specific device geometry, for QPC1,

$$s_{\mathrm{QPC}} \equiv \frac{\partial g}{\partial V_{\mathrm{Q1}}} = \frac{\partial g}{\partial \phi_{\mathrm{SP}}} \frac{\partial \phi_{\mathrm{SP}}}{\partial V_{\mathrm{Q1}}}, \tag{5.4}$$

where ϕ_{SP} is the electrostatic potential at the saddle point of QPC1. For the SQD,

$$s_{\mathrm{SQD}} \equiv \frac{\partial g}{\partial V_{\mathrm{D}}} = \frac{\partial g}{\partial \phi_{\mathrm{dot}}} \frac{\partial \phi_{\mathrm{dot}}}{\partial V_{\mathrm{D}}}, \tag{5.5}$$

where ϕ_{dot} is the electrostatic potential in the center of the SQD.

For the QPC, the conductance, g, and its derivative with respect to potential, is calculated as a thermal average over the transmission probability, following Ref. [Fertig 1987].

[5]The contribution from thermal fluctuations to intrinsic sensor noise is negligible. The cryogenic amplifier contributes 60% (40%) of the total noise for SQD (QPC1).

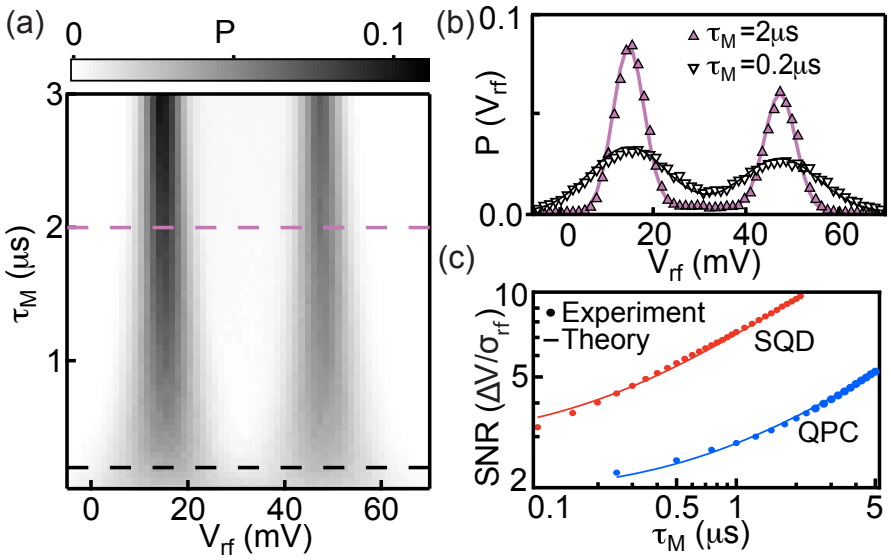

Figure 5.3: (Color online) (a) Probability density P of single-shot outcomes, $V_{\rm rf}$, (0.7 mV binning) as a function of integration time, τ_M, of the rf - charge signal $v_{\rm rf}$. The separation time $\tau_{\rm S}$ is stepped from 1 to 200 ns, every 1000 cycles for a total of 30,000 cycles. Measured with SQD, Device 2. The left [right] peak corresponds to the (0,2) [(1,1)] charge state and therefore singlet [triplet] measurement outcomes [Barthel 2009]. (b) Cuts of $V_{\rm rf}$ along the dashed lines in (a), along with theoretical curves [Barthel 2009]. (c) Signal to noise ratio (SNR), defined as peak separation$\Delta\, V$ divided by peak width σ as a function of measurement integration time τ_M for QPC1 (Device 1, -89 dBm rf power) and SQD (Device 2, -99 dBm rf power), along with theory curves (see text).

The width of the riser between conductance plateaus scales as

$$\mathcal{E} \equiv \sqrt{\hbar^2 U_x/2m}, \tag{5.6}$$

where U_x is the curvature of the saddle potential in the direction of the current. The self-consistent calculation presented below yields $\mathcal{E} \sim 0.2$ meV, an order of magnitude greater than k_BT. Thus the riser width is roughly independent of temperature. The SQD conductance is modeled by a master equation [Beenakker CB 1991] assuming transmission via a single orbital level in the dot. This approach is applicable, given the single-particle level spacing is large, ~ 200 μeV, but is only valid for small tunneling rate, γ, from the dot to the leads, such that $\hbar\gamma \ll k_BT$. In the experiment, a larger coupling is used, such that $\hbar\gamma \sim k_BT$. This gives rise to some quantitative discrepancy between the model and the experiment, but the qualitative comparison between SQD and QPC performance remains

valid.

The lever-arm terms in the definitions of sensitivity, $\partial\phi/\partial V_D$ for the SQD and $\partial\phi/\partial V_{Q1(2)}$ for the QPCs, depend on positions of nearby conductors that screen the interaction between source of the voltage and the potential at the target point. For QPC1(2), a change of $V_{\mathrm{Q1(Q2)}}$ is screened as charge in the leads of the QPC flow in or out of the saddle region and *opposes* the change of ϕ_{SP} caused by the gate voltage change. In contrast, the SQD lever arm is primarily determined by screening from other gates, rather than the 2DEG itself because the dot is isolated by tunnel barriers and the charge is fixed by CB. Numerical calculation below gives a lever arm that is typically ~ 20 times greater for an SQD than for a QPC. Thus 2DEG screening substantially influences sensor response.

Conductances of the SQD and QPCs are calculated using the SETE code [SETE code; Stopa 1996], which simulates the 3D electronic structure of the device within the effective-mass local-density-approximation to density functional theory. The calculation produces the total free energy of the SQD as a function of V_D and N, enabling a calculation of the conductance in the single-level CB regime [Stopa 1993]. Figure 4(a) shows a plot of the calculated SQD conductances, and their difference, between the cases where the double dot charge is held in the (0,2) and (1,1) states, as a function of gate voltage offset$\Delta\ V_D$. For this calculation, the ratio $\hbar\gamma/k_BT$ is set to unity, based on experimental peak conductance values [Fig. 1(b)]. We note, however, that the fractional change of conductance,$\Delta\ g/\bar{g}$, across the transition from (0,2) to (1,1) does not depend on $\hbar\gamma/k_BT$. For QPC1, the evolution of the potential profile with varying V_{Q1} is calculated with SETE. The (1,1) and (0,2) conductances in Fig. 4(b) are evaluated by solving the transverse Schrödinger equation in slices through the QPC and evaluating a 1D WKB expression for the transmission.

In the experiment, V_D and V_{Q1} are not swept, rather they are held at their most sensitive point and the conductance (through QPC or SQD) is allowed to change due to the change in double dot state. The most sensitive points of the sensors are at the extrema of$\Delta\ g$. Here, the ratio $|\Delta g|/\bar{g}$ is ~ 1.4 for the SQD and ~ 0.1 for QPC1, roughly consistent with experiment.

A color scale plot of the 2D electron density for typical gate voltages is shown in Fig. 4(c).

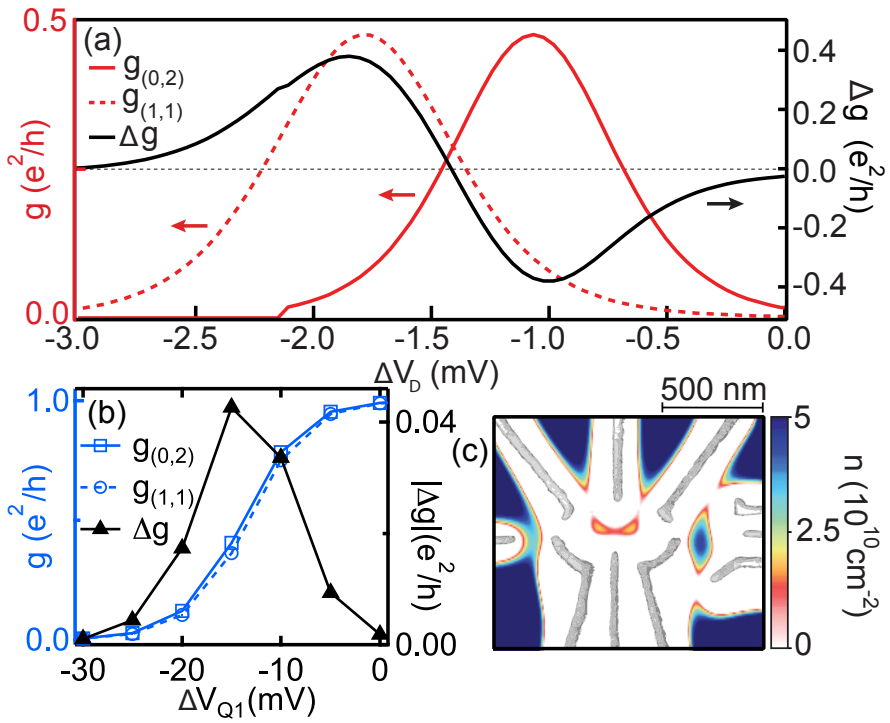

Figure 5.4: (Color online) (a) Conductance (simulation) through the SQD as function of the gate voltage V_D, for the two double dot charge-states $(1,1)$ and $(0,2)$. (b) Conductance through QPC1 at 5 mV intervals (lines are guide to the eye). (c) Electron density profile for typical gate voltages in the (1,1) configuration, with superimposed micrograph of device. The color scale is centered near $2.5 \times 10^{10}\text{cm}^{-2}$ to accentuate the charge in the dots and the saddle point of QPC1.

5.6 Conclusion

In conclusion, by taking advantage of the increased sensitivity and SNR of a sensor quantum dot in the CB regime (compared to a proximal QPC), we have demonstrated single-shot spin-to-charge readout of a few-electron double quantum dot in $\sim 100\,\text{ns}$ [6] with $SNR \sim 3$ (Fig. 3), representing an order of magnitude improvement over previous results [Barthel 2009]. Numerical simulation based on density functional theory yields good qualitative agreement with experiment, and elucidates key differences between a quantum dot and a QPC as a proximal charge sensor. Reduced screening and smaller characteristic energy needed to change transmission in the quantum dot compared to the QPC are responsible for its im-

[6] The measurement time is limited by the measurement bandwidth, not the time needed to obtain a SNR of unity.

proved performance.

Acknowledgments

We acknowledge funding from ARO/iARPA, the Department of Defense and IBM. MK acknowledges support from Augustinus Foundation, Højgaard Foundation and Stefan Rozental and Hanna Kobylinski Rozental Foundation. This work was performed in part at the Center for Nanoscale Systems (CNS), a member of the National Nanotechnology Infrastructure Network (NNIN), which is supported by the National Science Foundation under NSF award no. ECS-0335765. Computational support from the NNIN computation project (NNIN/C) is gratefully acknowledged. We thank Hendrik Bluhm, Edward Laird and David Reilly for useful discussion.

Chapter 6

Singlet-Triplet Qubit Relaxation and Initialization in a magnetic Field Gradient

C. Barthel[1,3] J. Medford[1,3] H. Bluhm[1] A. Yacoby[1] C. M. Marcus[1] M. P. Hanson[2] A. C. Gossard[2]

[1]Department of Physics, Harvard University, Cambridge, Massachusetts 02138, USA

[2]Materials Department, University of California, Santa Barbara, California 93106, USA

[3] These authors contributed equally to this work.

The measurement visibility and triplet relaxation time, T_1, of a singlet-triplet qubit in a double quantum dot are studied as function of magnetic field gradients induced by spin polarization of GaAs nuclei. For applied magnetic fields between 10 mT and 2 T, a nuclear field gradient is always observed after a nuclear polarization pump-cycle. The field gradient results in a reduced visibility of measured singlet-triplet precessions, which for long time averages reproduces the phenomenology previously attributed to a suppression of singlet-triplet dephasing. Performing fast measurements, with a high sensitivity sensor quantum dot (SQD), we study the dependence of the triplet relaxation time during measurement on magnetic field gradient, gate voltage configuration during measurement and applied magnetic field. We develop a simple model describing charge relaxation after singlet-triplet mixing that agrees well with the data. The initialization fidelity of a singlet decreases with increasing field gradients, presumably due to finite times over which the system is separated into two dots, and recombined into one dot. We intentionally reduce the initialization

fidelity in $S - T_0$ precession experiments, thereby performing a weak measurement of the nuclear magnetic field gradient. The findings are relevant for quantum information processing, where high measurement and initialization fidelities in the presence of magnetic field gradients are desired [1].

[1]This chapter is adapted from a manuscript in preparation for submission [Barthel T1 2010].

6.1 Introduction

Spin states of confined electrons are of interest for the investigation of basic quantum mechanics, decoherence and controlled entanglement, as probes of mesoscopic nuclear spin environments, and as qubits in quantum information processing [Loss 1998]. The singlet-triplet basis of a pair of electron spins in two coupled quantum dots has been suggested as a logical qubit, as it is inherently protected against collective dephasing [Levy 2002]. Sub-nanosecond operations on the qubit have been realized, using the exchange energy between singlet and triplet states to perform rotations around one of the qubit bloch sphere axes [Petta 2005]. Qubit rotations around a second independent axis, needed for universal control, can be induced by a magnetic field difference between the two quantum dots. A field difference for these rotations can be realized via a micro magnet on top of the double dot [Pioro-Ladrière 2007], and has recently been realized via a gradient in the nuclear polarization of the host material [Foletti 2009]. Fast measurement of a qubit state has been demonstrated for two-electron spin states [Meunier 2006; Barthel 2009], as well as for single-electron spin states [Elzerman 2004; Amasha 2008].

Aside from being a useful tool to manipulate the qubit, the Overhauser fields from the nuclei also are the major source of qubit decoherence [Petta 2005]. The interaction between electron spins and nuclear spins in GaAs has been studied optically [Paget 1977] and in electronic transport measurements where the nuclear spin state showed hysteretic behavior and strongly influenced the electronic properties [Ono 2004; Baugh 2007]. In pulsed measurements, the time evolution and statistics of polarized and unpolarized nuclear states have been studied [Reilly Diff. 2008; Reilly 2007], and the nuclear spins have been identified as a mechanism of electron spin relaxation [Johnson Nature 2005]. Spin relaxation limits the fidelity of qubit measurement [Barthel 2009], therefore it is important to understand how magnetic field gradients, from micro-magnets or nuclear polarizations, affect the qubit relaxation time at the readout stage.

In Ref. [Reilly 2008], it was observed that a nuclear pump-cycle, exchanging spin between the electrons and the nuclear bath, increased the probability, P_S, to measure a singlet outcome after evolution of a separated singlet state, which is sensitive to nuclear field

gradients. It was conjectured that the pump-cycle reduced the fluctuating nuclear field difference between the two quantum dots by preparing a special nuclear state, stable over long time scales. This interpretation is consistent with various theoretical works [Ramon 2007; Ribeiro 2008; Stopa 2010], while other experimental and theoretical work suggest that nuclear pump-cycles generally build up field gradients [Foletti 2009; Gulland 2010].

In this chapter, we suggest an alternative explanation for the increased singlet measurement probability observed in Ref. [Reilly 2008], based on a nuclear field gradient induced reduction of the triplet relaxation time, resulting in vanishing measurement visibility for large nuclear polarizations. We investigate the buildup of nuclear polarization by electrical pump-cycles for a range of directions and magnitudes of applied magnetic field and find that for all investigated experimental parameters, a gradient in nuclear polarization is induced together with an average polarization.

A reduction in the visibility of measured singlet-triplet precessions with increasing nuclear field gradient is observed for all parameters. The visibility is studied as function of nuclear field gradient, applied magnetic field, and gate voltage configuration during the measurement. Simultaneously, the triplet relaxation time at the measurement point is measured in time domain. The dominant part of the visibility reduction for large nuclear polarizations is due to an increased triplet relaxation rate during the measurement, independent of applied magnetic field. We find good agreement with a simple model describing triplet decay, via charge relaxation after singlet-triplet mixing driven by the field difference. By introducing a ramp-time, over which an initial singlet state is separated to occupy two dots and recombined into one dot after evolution, we intentionally reduce the initialization fidelity in $S - T_0$ precession experiments. Thereby a weak measurement of the nuclear magnetic field gradient is performed. The precession data as function of ramp-time gives evidence that a finite pulse rise-time decreases the initialization and readout fidelity of the qubit in the presence of nuclear polarization.

The remainder of this chapter is organized as follows. In section 6.2 we discuss the double dot system under investigation and the technical setup. The theory of the two electron qubit system, the nuclear pumping and the probe-cycle, as employed in previous

work, are explained in the first part of section 6.3. In section 6.4 we discuss the mechanisms of relaxation during the measurement and the simple model, that we introduce to describe the experimental results of this paper. The effects of finite pulse rise- or ramp-times on the initialization fidelity are discussed in the final part of section 6.3. Experimental methods and our results are discussed in section 6.5, beginning with the measurement of nuclear gradients and precession visibilities. We then discuss the connection between visibility, relaxation time and nuclear field difference in section 6.6. Data showing the influence of finite ramp- and rise- times on singlet-triplet precession visibilities are presented in section 6.7 before we discuss different parameters for all of which the same phenomenology - nuclear field gradient, reduced relaxation time and visibility - were observed in section 6.8.

6.2 System

The double quantum dot is formed by Ti/Au depletion gates on a GaAs/$Al_{0.3}Ga_{0.7}As$ heterostructure with a two-dimensional electron gas (2DEG), with density 2×10^{15} m^{-2}, mobility 20 m^2/Vs, 100 nm below the surface. A magnetic field, B, is applied by a 3-axes magnet and varied over a wide range of magnitudes and directions to investigate the effects of the pump-cycle, see text below. The direction of the applied field defines the spin quantization axis z. For the data presented in this paper the field direction is shown in Fig. 1(a), and the magnetic field magnitude is $B = 200$ mT, except where noted otherwise.

As described elsewhere [Barthel SQD 2010; Reilly APL 2007], a proximal radio-frequency sensor quantum dot (rf-SQD), on the right in the micrograph, is sensitive to the charge state of the double dot. The SQD is only energized during the measurement, and yields a sub-μs time resolution output signal, v_{rf}, via reflectometry, from which the charge state of the double dot is inferred. A Tektronix AWG5014 arbitrary waveform generator allows fast pulsing of the gate voltages, V_{L} and V_{R}, which set the electrical potential in the left and right quantum dot and control the double dot charge state, $(N_{\mathrm{L}}, N_{\mathrm{R}})$, where N_{L}, N_{R} are the number of electrons in the left, right dot. The charge state is constrained to (1,1) and (0,2) in this work and the two-electron spin qubit is controlled via the energy detuning, ϵ, between the

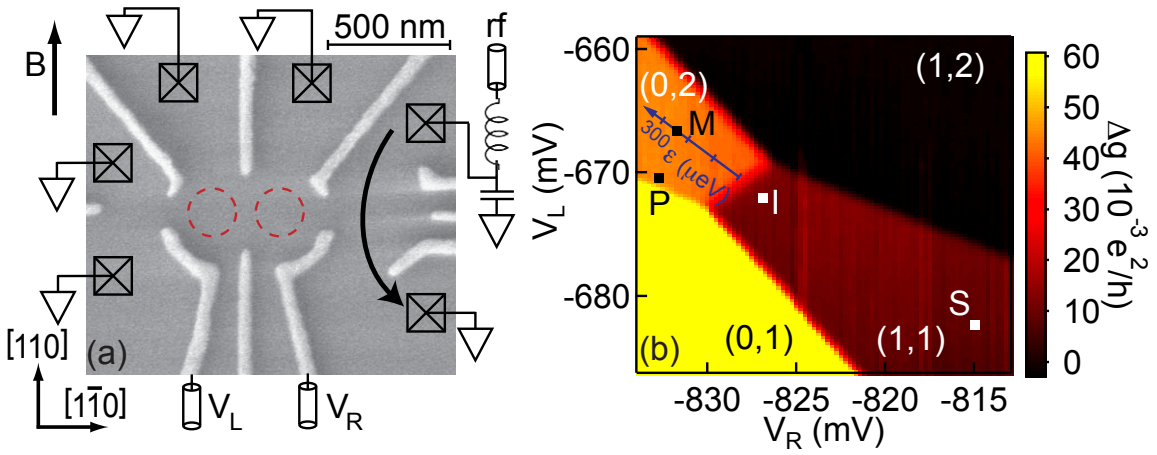

Figure 6.1: (a) (Color online) (a) Micrograph of lithographically identical device. Gate voltages, V_{L} and V_{R}, set the electrostatic energy of left and right dot. A sensor quantum dot on the right allows fast measurement of the double dot charge state via rf reflectometry. The direction of magnetic field, B, is indicated, as well as the GaAs crystal axes. (b) Change of sensor dc conductance$\Delta\ g$, with double dot charge state $(N_{\mathrm{L}}, N_{\mathrm{R}})$, constrained to (1,1), (0,2) in this work. The qubit state is controlled by the (1,1)-(0,2) energy detuning, ϵ, set by gate voltages V_{L} and V_{R} along the diagonal axis through the markers S, M. The scaling of detuning is $|\epsilon| = \eta\sqrt{\Delta V_{\mathrm{L}}^2 + \Delta V_{\mathrm{R}}^2}$, with a lever arm $\eta = 40$ μeV/mV and voltage detunings, ΔV_{L}, ΔV_{R}, from the (1,1)-(0,2) charge degeneracy. Markers indicate gate voltages during pump- and probe-cycles. Singlet preparation at point P. Pump: $S - T_+$ mixing at point I, see text. Probe: Separation of singlet for $S - T_0$ mixing at point S and measurement at point M at variable detuning, 80 μeV $< \epsilon_{\mathrm{M}} <$ 260 μeV.

(1,1) and (0,2) charge state. The detuning is varied via the gate voltages, V_{L} and V_{R}, and scales as $|\epsilon| = \eta\sqrt{\Delta V_{\mathrm{L}}^2 + \Delta V_{\mathrm{R}}^2}$, with a lever arm $\eta = 40$ μeV/mV, calibrated in dc transport measurements through the double dot [Johnson PRB 2005; Van der Wiel 2003]. The gate voltage detunings,$\Delta\ V_{\mathrm{L}}$ and$\Delta\ V_{\mathrm{R}}$, are measured from the (1,1)-(0,2) charge degeneracy along the diagonal axis defined by the points S and M in Fig. 1(b). Changes in gate voltages not only affect the detuning, but also alter the inter-dot and dot-lead tunnel couplings. This effect is neglected in the following analysis, assuming changes$\Delta\ V_{\mathrm{L}}$ and$\Delta\ V_{\mathrm{R}}$ only affect the energy detuning, ϵ, but possible implications are discussed where applicable.

6.3 Theory, Nuclear Polarization, $S - T_0$ - Precession Measurements

Energy levels of the system as function of detuning, ϵ, from the (1,1) - (0,2) charge degeneracy are shown in Fig. 2(a). The qubit comprises the two-electron singlet, S, and the magnetic quantum number, $m = 0$, triplet, T_0, of the (1,1) charge state [Petta 2005]. Preparation of a singlet state is achieved dissipatively at point P, see Figs. 6.1(b) and 6.2(a), through relaxation into the (0,2) singlet state involving electron exchange with the leads [Petta 2005]. A (0,2) singlet can be separated into a (1,1) singlet, S, by following the lower branch of the singlet anti-crossing through $\epsilon = 0$.

Nuclear polarizations can be created electrically by repeated ramping of ϵ through the anti-crossing of singlet S and $m = 1$ triplet, T_+ [Foletti 2009; Reilly Diff. 2008; Reilly 2008]. In the nuclear pump-cycle, a singlet state is prepared, and the detuning, ϵ, is ramped through ϵ_{I}. When following the lower branch of the level-crossing an electron spin is flipped by hyperfine interaction, see inset of Fig. 6.2(a). Due to spin conservation a nuclear spin is flipped simultaneously. Subsequently the system is rapidly brought back to $\epsilon > 0$, without spin flip. The system is reset to a singlet state at point P, via electron exchange with the leads rather than electron-nuclear spin flips, resulting in a net nuclear spin flip per pump-cycle.

At large negative detuning, ϵ_{S}, the qubit states S and T_0 are nearly degenerate. A difference in magnetic field,$\Delta\ B_z$, between left and right dot, e.g. from nuclear Overhauser fields, induces precession between the two states, at the $S - T_0$ precession frequency,

$$f_{\mathrm{S}} = \frac{|g|\,\mu_{\mathrm{B}}\Delta B_{\mathrm{z}}}{h}, \tag{6.1}$$

with the Planck constant, h, the Bohr magneton, μ_{B}, the bulk electron g-factor in GaAs, $g = -0.44$. A frequency shift due to the residual $S - T_0$ exchange energy splitting, J_{S} [2],

[2] J_{S}, estimated to be $J_{\mathrm{S}} \sim 10$ neV $\pm$ 5 neV, from the drop of V_{S} at the lowest measured field differences,

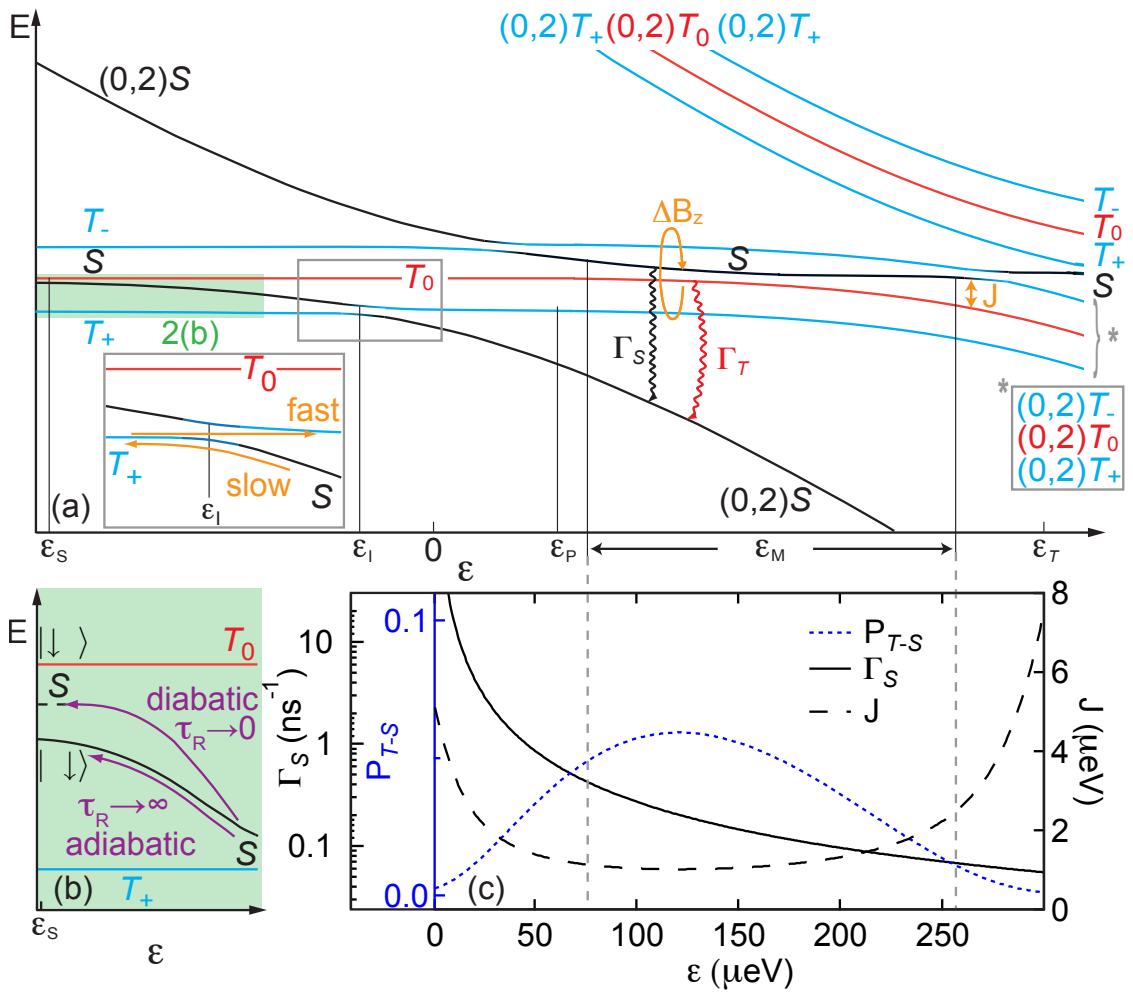

Figure 6.2: (a) (Color online) (a) Energy level diagram as function of detuning, ϵ, charge state is (1,1) unless noted. Pulse-cycle detunings, $\epsilon_{\rm P}$ of singlet preparation, $\epsilon_{\rm I}$ of $S-T_+$ resonance, and $\epsilon_{\rm S}$, where the system is pulsed for $S-T_0$ precession, are labeled. The relaxation channels of triplet state, T_0, during measurement at $\epsilon_{\rm M}$ are indicated: Charge relaxation,Γ_S, after $S-T_0$ mixing by nuclear field difference,$\Delta B_{\rm z}$, and processes not involving$\Delta B_{\rm z}$, at rateΓ_T. The $S-T_0$ mixing is suppressed by the exchange energy splitting, J, due to two anti-crossings, at $\epsilon=0$ between singlet states of (1,1)-(0,2), and at $\epsilon=\epsilon_T\sim 300$ μeV between triplet states of (1,1)-(0,2). Inset: Illustration of pump-cycle. (b) Ramping the detuning to $\epsilon_{\rm S}$ in finite ramp time, $\tau_{\rm R}$, for an initial singlet state, S, yields an admixture of the ground state of the nuclear field gradient, $|\uparrow\downarrow\rangle$. Only the singlet (triplet) state is sensitive to$\Delta B_{\rm z}$, resulting in a reduced visibility, V, of measured $S-T_0$ precessions. (c) Charge relaxation rate,Γ_S, of metastable (1,1) singlet state, Eq. (6.6), and the singlet admixture, P_{T-S}, Eq. (6.4) , of an initial triplet state, mixed by$\Delta B_{\rm z}=15$ mT, and suppressed by the exchange energy, J, Eq. (6.5), plotted as function of detuning, ϵ. The plots use experimental parameters.

---

results in a shifted frequency $f_{\rm S}^*=\sqrt{f_{\rm S}^2+(J_{\rm S}^2/h)^2}$, a negligible correction at the relevant frequencies.

at point S can be neglected, as $J_S \sim 10$ neV ~ 0.5 mT is much smaller than the Zeeman energy of the typical$\Delta\ B_z$ in this work [Petta 2005; Laird 2006; Coish 2005]. At finite J_S, the qubit precesses at a lower than one visibility,

$$V_S = \frac{\Delta B_z^2}{\Delta B_z^2 + (J_S/g^*\mu_B)^2}, \tag{6.2}$$

for unit fidelity singlet initialization [Laird 2006; Coish 2005], however $V_S \sim 1$ for the values of$\Delta\ B_z$ in this work. The sensitivity of the qubit at point S to nuclear gradients is leveraged in a probe-cycle [Reilly 2007; Barthel 2009; Foletti 2009]. The cycle first prepares a spin singlet in $(0, 2)$, then the system is brought to the separation point S for a time τ_S, and finally brought to the measurement point M. If the separated electrons are in a singlet configuration when the system is pulsed to M, the system returns to $(0, 2)$, but if the two electrons are in a triplet state, it remains in $(1, 1)$ at point M. Superpositions are projected to one of the two charge states during measurement. The different charge states of singlet and triplet are measured, allowing to determine the spin state.

6.4 Relaxation Model

However, a triplet state is detected correctly only if it does not relax to the (0,2) singlet state before it can be measured. The relaxation pathways of a triplet state at the measurement point M are illustrated in the energy diagram in Fig. 2(b). The difference in nuclear Overhauser fields,$\Delta\ B_z$, mixes an initial triplet state, T_0, with the singlet state, S, which then rapidly relaxes to the (0,2) singlet, (0,2)S, with charge relaxation rateΓ_S. Processes not involving a precession into the singlet state occur on slower time scales and are summarized by the relaxation rate,Γ_T. Adding these two rate contributions to the triplet relaxation, we construct a simple model for the detuning and nuclear gradient dependence of the triplet relaxation time,

$$T_1 = \left(P_{T-S}\,\Gamma_S(\epsilon_M) + (1 - P_{T-S})\,\Gamma_T\right)^{-1}. \tag{6.3}$$

At the measurement point, M, an exchange energy splitting, J, between the singlet and triplet state suppresses the $S - T_0$ mixing, such that only a small fraction, P_{T-S}, of the initial triplet population is in a singlet state at a given time. At large exchange, and small relaxation rates, the evolution at M can be described by the eigenstates of the coherent evolution of the qubit inΔ B_z and J, with a triplet-like eigenstate and a singlet-like eigenstate [Taylor PRB 2007]. For an initial triplet state, the population of the singlet-like eigenstate is negligible and the evolution reduces to the relaxation of the triplet-like eigenstate. Following the analysis in Ref. [Taylor PRB 2007], P_{T-S} is calculated from the singlet projection of the triplet-like eigenstate

$$P_{T-S} = \frac{1}{2}\left(1 - \frac{J(\epsilon_{\mathrm{M}})}{\sqrt{\Delta B_z^2 + J(\epsilon_{\mathrm{M}})^2}}\right) . \tag{6.4}$$

The exchange, J, is function of the energy detuning, ϵ_M, of the point M, and is due to two charge state anti-crossings. The first anti-crossing is between the singlet states of the (0,2) and (1,1) charge configuration at $\epsilon = 0$; the second anti-crossing, at $\epsilon = \epsilon_T$, is between the $m = 0$ triplet states of the (0,2) and (1,1) charge configuration. The exchange at $\epsilon > 0$ cannot be measured directly and is approximated with the expression

$$J = \frac{t_S^2}{\epsilon + \sqrt{4\,t_S^2 + \epsilon^2}} - \frac{t_T^2}{(\epsilon - \epsilon_T) - \sqrt{4\,t_T^2 + (\epsilon - \epsilon_T)^2}} \tag{6.5}$$

from Ref. [Taylor PRB 2007], where t_S is the tunnel coupling for singlet states, and t_T is the tunnel coupling for triplet states. Equation (6.5) neglects the change in tunnel couplings due to changes in ϵ via gate voltage pulses, which is believed to give deviations from this functional form [Laird 2006].

The detuning dependence of the charge relaxation rate,Γ_S, has been discussed and experimentally studied in Ref. [Fujisawa 1998]. There, a decrease in relaxation rate with increased detuning, roughly faster than ϵ^{-1} but slower than ϵ^{-2}, was found and compared to expected power laws for different dissipation mechanisms. For piezoelectric interaction with 3D (2D) phonons, a power law,$\Gamma_S \propto \epsilon^{-1}$ (ϵ^{-2}), is expected [Fujisawa 1998]. As an

approximate description of the ϵ-dependence of the charge relaxation we use

$$\Gamma_S = \alpha\epsilon^{-1} + \beta\epsilon^{-2}. \tag{6.6}$$

The singlet charge relaxation rate,Γ_S, Eq. (6.6), the exchange, J, Eq. (6.5), and the singlet admixture, P_{T-S}, of an initial triplet state, Eq. (6.4), are shown as function of detuning, ϵ, in Fig. 6.2(c). Experimental parameters, discussed in section 6.5, are used in the plots.

We now discuss the effects of finite pulse rise times. In order to perform $S-T_0$ precession experiments, or for qubit initialization in quantum information processing, a singlet state, S, typically is initialized by electron separation from an $(0,2)S$ singlet state, as discussed above. Figure 6.2(b) shows a close-up of the level diagram at large negative detuning, $\epsilon_{\rm S}$, where S and T_0 are nearly degenerate and split by residual exchange, $J_{\rm S}$, smaller than the typical Zeeman splitting between the two eigenstates in the nuclear Overhauser fields, $|\uparrow\downarrow\rangle$ and $|\downarrow\uparrow\rangle$. The arrows in $|\uparrow\downarrow\rangle$ indicate the electron spin in the left (right) dot being parallel (anti-parallel) to the quantization axis,$\Delta B_{\rm z} > 0$ is assumed without loss of generality. In that notation the triplet / singlet state is $T/S = (|\uparrow\downarrow\rangle \pm |\downarrow\uparrow\rangle)/\sqrt{2}$ and in the limit, $J_{\rm S}/\Delta B_{\rm z} \to 0$, the nuclear field eigenstates become the eigenstates of the total Hamiltonian, as illustrated in Figure 6.2(b). A singlet, separated infinitely slowly with a ramp time, $\tau_{\rm R} \to \infty$, is adiabatically loaded into the ground state of the nuclear field, $|\uparrow\downarrow\rangle$ [Petta 2005; Taylor PRB 2007]. In the limit of instantaneous separation, with a ramp time, $\tau_{\rm R} \to 0$, a pure singlet state is initialized. For finite ramp- or rise-times, a singlet is initialized with a smaller than one fidelity, with some admixture of the nuclear eigenstates. Similarly, the recombination of the two electrons into one dot, after evolution in point S, only maps the S, T_0 state onto the (0,2), (1,1) charge state with unity fidelity for an instantaneous change of detuning, ϵ. For a finite ramp time, the visibility of singlet and triplet is reduced due to admixture of the nuclear eigenstates, analogous to the separation. In the final part of this paper, the influence of ramp- and rise-time on initialization fidelity, $F_{\rm I}$, incorporating visibility reduction due to the finite duration of both separation and recombination, is investigated.

6.5 Time evolution of nuclear Gradient and $S - T_0$ Visibility

To study the nuclear gradients built by the electron-nuclear spin flips, pump-probe experiments are performed. The nuclear state is prepared by a pump-cycle, with a ~ 4 MHz repetition rate, ramping through ~ 10 μeV around ϵ_I in 100 ns. The pump-cycle is repeated ~ 240 million times over 60 s. The waveform generator then immediately performs a sequence of probe-cycles, with varying $\tau_{\rm S}$, to extract the nuclear field difference from $S - T_0$ precessions. The singlet measurement probability, P_S, is determined from single-shot measurements, following the procedure described in Ref. [Barthel 2009]. After preparation in $(0, 2)S$ at P, the probe-cycle cycle separates the singlet to point S, see Figs. 6.1(b), 6.2(a), without nominal ramp time, $\tau_{\rm R} = 0$. The system is held at detuning, $\epsilon_{\rm S} \sim -700$ μeV, for the separation time, $\tau_{\rm S}$, and is then brought back to the measurement point M, where the charge signal, $v_{\rm rf}$, is recorded over the total measurement time, $\tau_{\rm M}^{\rm max} \sim 10\mu$s. The charge signal, $v_{\rm rf}$, is then integrated over ~ 300 ns, yielding single-shot measurement outcomes, $V_{\rm rf}$, which are identified as singlet or triplet outcomes by comparison to a threshold voltage, as discussed in Ref. [Barthel 2009]. For each separation time, $\tau_{\rm S}$, 100 single-shot measurements are performed, and the singlet measurement probability, P_S, is calculated as the percentage of singlet outcomes. Figure 6.3(a) shows P_S as function of $\tau_{\rm S}$ and time,$\Delta\ t$, after the pump-cycle. The separation time, $\tau_{\rm S}$, is stepped from 1 ns to 100 ns in 80 steps, for a total of 8000 single-shot measurements before the data is saved and processed. Sets of 8000 cycles, corresponding to a column in Fig. 6.3(a), are acquired every second, and are shown for two values of$\Delta\ t$ in Fig. 6.3(b). Measurements immediately after the pump-cycle,$\Delta\ t \lesssim 50$ s, show an almost unity singlet measurement probability, P_S, while after longer times,$\Delta\ t$, high frequency, low visibility oscillations become visible. At long times,$\Delta\ t \gtrsim 300$s, close to unity visibility $S - T_0$ precessions with frequencies corresponding to equilibrium nuclear field differences,$\Delta\ B_{\rm z}$, are observed. Fourier transforms (FFT) of P_S are calculated and the normalized Fourier amplitude $A_{\rm FFT}$ is plotted as function of frequency, $f_{\rm S}$, and time after pumping,$\Delta\ t$, in Fig. 6.3(c). The Fourier transforms have clear maxima, as illustrated by two vertical cuts through the data in Fig. 6.3(c) at$\Delta\ t = 150$ s and$\Delta\ t = 300$ s, shown in Fig. 6.3(d). The frequency with maximum FFT component is correlated for two adjacent

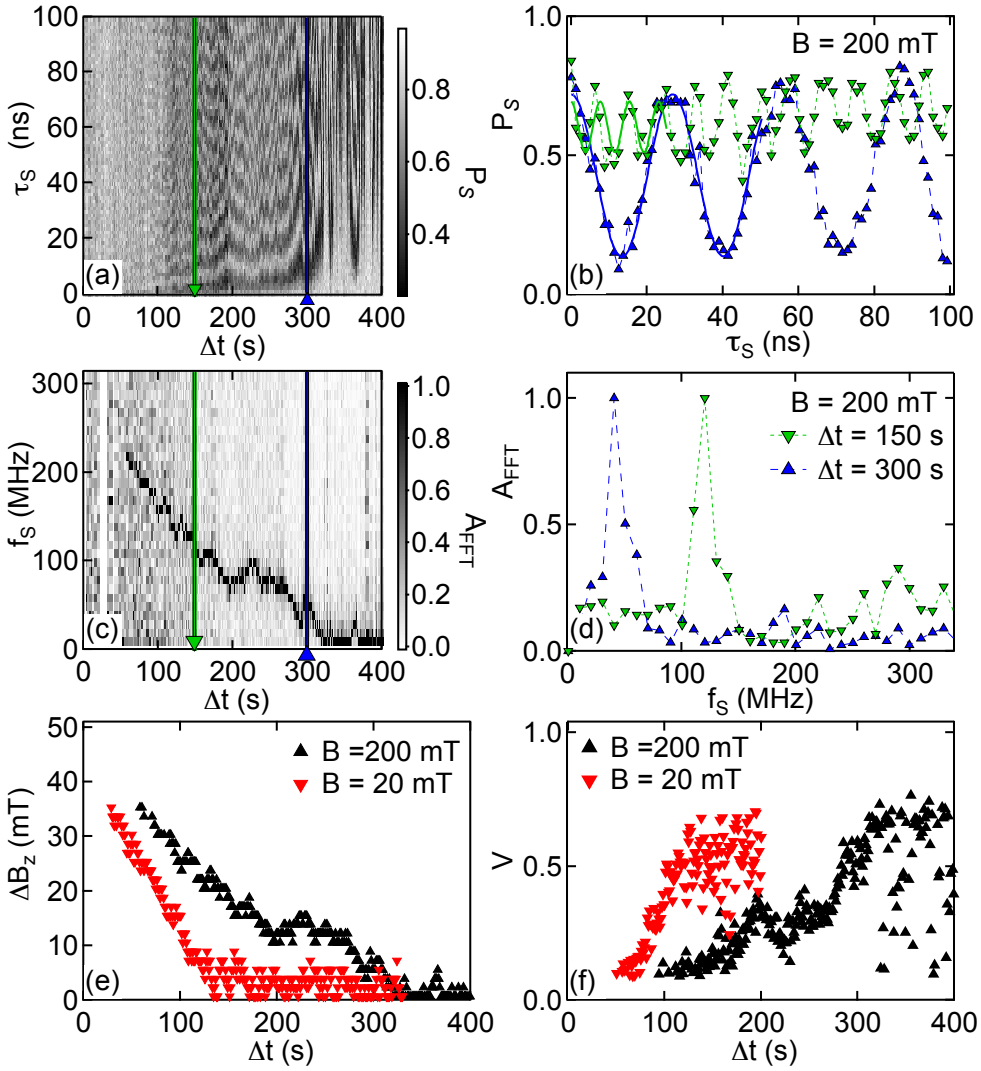

Figure 6.3: (Color online) (a) Probability, P_S, of singlet measurement outcome as function of $S - T_0$ mixing time, τ_S, and time,Δ t, after a 60 s, ~ 4 MHz pump-cycle; taken at $B = 200$ mT. Note the close to unity singlet measurement probability with low visibility, high frequency oscillations at smallΔ t. (b) Vertical cuts through (a), showing $P_S(\tau_S)$ curves, from which visibilities, V, and nuclear field differences,Δ B_z, are extracted via cosine fits, Eq. (6.7), forΔ $t = 150$ s and 300s. (c) Normalized Fourier-amplitudes, A_{FFT}, of (a), as function of frequency, f_S and time,Δ t, after pumping. (d) Vertical cuts through (c), for $\Delta t = 150$ s and 300 s. (e) The nuclear field difference,Δ B_z (black markers), between left and right dot as function of time,Δ t after pumping. The gradient,Δ B_z, is extracted from (c,d) by the relation (6.1), yieldingΔ $B_z \sim f_S$ mT/(6.16 MHz). The field difference for equivalent data at applied magnetic field, $B = 20$ mT, is shown as well (red, gray markers). At lower applied field the gradient decays faster, consistent with nuclear spin diffusion [Reilly Diff. 2008; Reilly 2007]. (f) Visibility, V, of measured $S - T_0$ oscillations as function ofΔ t for data in (a) (black), and equivalent data at $B_{ext} = 20$ mT (red, gray), corresponding to data in (e).

columns and decreases with time after pumping,$\Delta\ t$, as expected for a decaying nuclear field gradient,$\Delta\ B_z$. The values of nuclear field difference,$\Delta\ B_z$, from FFT peak positions are used as starting points for fits of

$$P_S = P_0 + 1/2\, V \cos\left(2\pi f_S \tau_S\right) \tag{6.7}$$

to the time domain precession data, as shown in Fig. 6.3(b), with frequency, f_S, given by Eq. (6.1). The nuclear field differences,$\Delta\ B_z$, extracted from the fits of Eq. (6.1) agree with the values from Fourier transform peak positions within one FFT bin size ($\sim$ 1 mT). For the cut at$\Delta\ t \sim 150$ s the visibility is $V = 0.2$, and the extracted nuclear field difference is$\Delta\ B_z \sim 20$ mT, while for the cut at$\Delta\ t \sim 300$ s, $V = 0.6$, and$\Delta\ B_z \sim 6$ mT [3]. Figure 6.3(e) shows the nuclear field difference,$\Delta\ B_z$, corresponding to the frequency, f_S, of maximum Fourier amplitude, A_{FFT}, in Fig. 6.3(c), according to Eq. (6.1). For an identical pump-probe experiment, performed at applied field, $B = 20$ mT, the nuclear field difference,$\Delta\ B_z$, from FFT peak positions is shown as well. Note that the decay of the field difference with time,$\Delta\ t$, is faster for the 20 mT data, consistent with nuclear spin diffusion [Reilly 2007; Reilly Diff. 2008]. Visibilities, V, extracted from fits, Eq. (6.7), are shown as function of$\Delta\ t$ in Fig. 6.3(f) .

6.6 Triplet Relaxation Time as Function of magnetic Field Difference

To investigate the dependence of the visibility on the magnetic field difference and the mechanism reducing the visibility, pump-probe measurements are performed for nine values of measurement point detuning, ϵ_M, after a 60 s, 4 MHz pump-cycle. Measured visibilities, V, are shown in Fig. 6.4(a) as function of the simultaneously measured nuclear field difference, ΔB_z, for three of the nine values of ϵ_M. The visibility sharply decreases with increasing

[3] Other parameters are, $P_0 = 0.6$ for$\Delta\ t = 150s$, and $P_0 = 0.4$ for$\Delta\ t = 150s$.

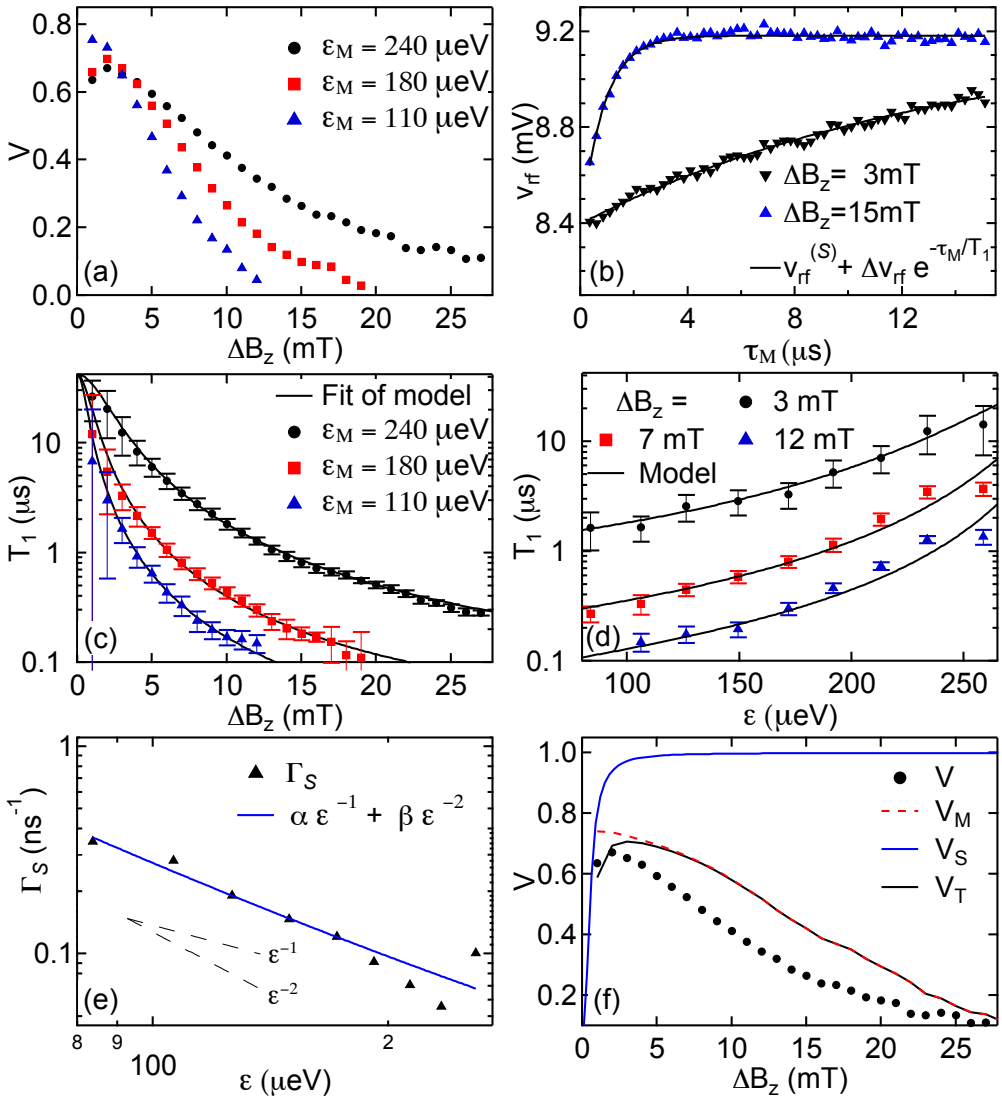

Figure 6.4: (Color online) (a) Visibility, V, of $S - T_0$ precession as function of$\Delta\ B_z$, for three out of nine values of detuning, ϵ_M. (b) Average rf-voltage amplitude, v_{rf}, as function of , τ_M, spent at ϵ_M after $S - T_0$ mixing at ϵ_S. The rf voltage is averaged over 8000 cycles, $\tau_S = 1 - 100$ ns. The triplet relaxation time, T_1, is extracted via exponential fits with $v_{rf}^S \sim$ 9 mV,$\Delta\ v_{rf} \sim -1$ mV. For$\Delta\ B_z = 3$ mT, $T_1 \sim 13\ \mu$s, while for$\Delta\ B_z = 15$ mT, $T_1 \sim 0.8\ \mu$s. (c) Measured relaxation time, T_1, of triplet T_0 at ϵ_M, as function of$\Delta\ B_z$. Solid lines are a simultaneous fit of Eq. (6.3) to T_1 data at nine detunings ϵ_M. Fit parameters are$\Gamma_S(\epsilon_M)$, see (e), triplet relaxation rate$\Gamma_T \sim (40\mu s)^{-1}$, and the T_0 charge tunnel coupling, $t_T = 12\ \mu$eV, which sets $J(\epsilon_M)$, Eq. (6.5). (d) T_1 as function of ϵ_M, with model for T_1, using Eq. (6.6) for$\Gamma_S(\epsilon)$ with α, β from (e). (e) Singlet relaxation rateΓ_S, extracted via simultaneous fit of Eq. (6.3) to data in (c). Solid line is a fit to Eq. (6.6), with $\alpha \sim 11\ \mu\text{eV ns}^{-1}$ and $\beta \sim 1600\ \mu\text{eV}^2\,\text{ns}^{-1}$. (f) Visibility, V, from fits to $S - T_0$ precession data, see Fig. 3(b), for $\epsilon_M = 240\ \mu$eV, with expected total visibility, V_T, Eq. (6.8). The single-shot measurement visibility, V_M, calculated from T_1 and measurement SNR. The intrinsic singlet visibility, V_S, Eq. (6.2), due to finite exchange, $J_S \sim 10$ neV ~ 0.5 mT, at ϵ_S [Laird 2006].

magnetic field differences, while the curves for smaller detuning, $\epsilon_{\rm M}$, fall off with$\Delta\ B_{\rm z}$ more rapidly. The total $S-T_0$ precession visibility, $V_{\rm T}$, is reduced from unity due to two expected mechanisms,

$$V_{\rm T} = V_{\rm M}\, V_{\rm S}, \tag{6.8}$$

where the measurement visibility, V_M, captures the imperfect fidelity of the single-shot measurement, as discussed in Ref. [Barthel 2009]. The intrinsic visibility, $V_{\rm S}$, due to finite exchange, $J_{\rm S}$, at the point S, Eq. (6.2), is $V_{\rm S} \sim 1$ for all but the smallest nuclear field differences,$\Delta\ B_{\rm z} \lesssim 1$ mT. The measurement visibility, $V_{\rm M}$, is calculated from the experimental parameters following the analysis in Ref. [Barthel 2009], and depends on the triplet relaxation time, T_1, at the measurement point. In order to determine the dependence of T_1 on $\Delta B_{\rm z}$, the relaxation of a triplet state at the measurement point is monitored via the charge signal, $v_{\rm rf}$, which is recorded with 100 ns time resolution over total time, $\tau_{\rm M}^{\rm max} = 4\ \mu$s. After 200 s, the total time spent at M is increased from 4 μs to 15 μs, while the time resolution is changed from 100 ns to 250 ns, in order to measure short and long relaxation times, T_1, optimally using oscilloscope memory. Figure 6.4(b) shows the rf voltage signal, $v_{\rm rf}$, averaged over 8000 probe-cycles, with $\tau_{\rm S}$ ranging from 1 to 100 ns, as function of the time, $\tau_{\rm M}$, spent at the measurement point M. The voltage, $v_{\rm rf}$, decays from $v_{\rm rf}^{(S)} + \Delta v_{\rm rf}$, corresponding to an equal mixture of charge states (0,2) and (1,1), to $v_{\rm rf}^{(S)}$, corresponding to the (0,2) charge state. The exponential fit yields a value of $T_1 \sim 13\ \mu$s for data taken at$\Delta\ B_{\rm z} = 3$ mT and a significantly smaller value of $T_1 \sim 0.8\ \mu$s for the data taken at$\Delta\ B_{\rm z} = 15$ mT.

The triplet relaxation time, T_1, is shown as function of nuclear field gradient,$\Delta\ B_{\rm z}$, in Fig. 6.4(c) for three different values of measurement point detuning, $\epsilon_{\rm M}$. Like the visibility, the triplet relaxation time, T_1, decreases sharply with increasing$\Delta\ B_{\rm z}$, and with decreasing $\epsilon_{\rm M}$ as shown in Fig. 6.4(d) for three different values of$\Delta\ B_{\rm z}$. To test whether the observed nuclear field dependence agrees with the model, a fit of Eq. (6.3) is performed simultaneously for nine values of $\epsilon_{\rm M}$, with $\Delta B_{\rm z}$ as independent variable. The exchange, $J(\epsilon_{\rm M})$, at point M is set by Eq. (6.5), and contains one fit parameter, the triplet tunnel coupling, $t_T \sim 12\ \mu$eV. Assuming Eq. 6.5, the singlet tunnel coupling, $t_S \sim 10\ \mu$eV, is estimated from the detuning,

$\epsilon_{\rm I}$, of the S - T_+ resonance footnoteAt $\epsilon_{\rm I}$, the exchange energy, $J_{\rm S}$, is equal to the Zeeman energy of T_+. Comparison with $J_{\rm S} = t_S^2/(\epsilon_{\rm I} - \sqrt{4t_S^2 + \epsilon_{\rm I}^2})$, from Ref. [Taylor PRB 2007], yields an estimate of t_S.. The energy detuning, $\epsilon_T \sim 300$ μeV, of the triplet charge transition is determined from dc transport measurements [Johnson PRB 2005; Van der Wiel 2003]. The fit, together with the measured parameters, yields the ϵ dependence of exchange energy, $J(\epsilon)$, shown in Fig. 6.2(c). The bare triplet relaxation rate,$\Gamma_T \sim (40\ \mu{\rm s})^{-1}$, is fitted to be equal for all detunings, an estimation that is justified by the weak dependence of Eq. (6.3) onΓ_T for$\Delta B_{\rm z} > 1$ mT and because measured values of T_1 agree with each other within the errors at small$\Delta B_{\rm z}$. For the singlet charge relaxation rate,$\Gamma_S(\epsilon_{\rm M})$, one fit parameter is used for each detuning, $\epsilon_{\rm M}$, yielding the values shown in Fig. 6.4(e). The rate,Γ_S, decreases with increasing detuning, and a fit of Eq. (6.6), yielding $\alpha \sim 11$ $\mu{\rm eV\,ns^{-1}}$ and $\beta \sim 1600$ $\mu{\rm eV^2\,ns^{-1}}$, shows reasonable agreement with the data. At $\epsilon_{\rm M} \sim 150$ μeV, the contributions from 2D and 3D phonons are about equal. The charge relaxation rates are consistent with the values measured in Ref. [Fujisawa 1998], when taking into account the difference in tunnel couplings, t_S. Deviations from the form (6.6) are expected, e.g. due to resonances from finite lengths in the phonon environment [Fujisawa 1998]. Figure 6.4(d) shows the model, Eq. (6.3), with$\Gamma_S(\epsilon)$ from Eq. (6.6), using α and β from the fit in Fig. 6.4(e). Note that the extracted values of α and β are rough estimates, as the functional form of $J(\epsilon_{\rm M})$, Eq. (6.5), is only approximate. The detuning dependence of$\Gamma_{\rm S}$, assuming Eq. 6.6 and using the obtained fit parameters α and β, is shown in Fig. 6.2(c). Since$\Gamma_S \propto t_S^2$ [Fujisawa 1998], and roughly $J \propto t_S^2$ (t_T increases with t_S), the first and dominant term in Eq. (6.3) becomes $\propto \Delta B_{\rm z}^2/t_S^2$ for$\Delta B_{\rm z} < J$. Contrary to intuition, a more transparent tunnel barrier yields longer triplet relaxation times, which is beneficial for quantum information processing, where large tunnel couplings enable fast operations [Petta 2005; Foletti 2009].

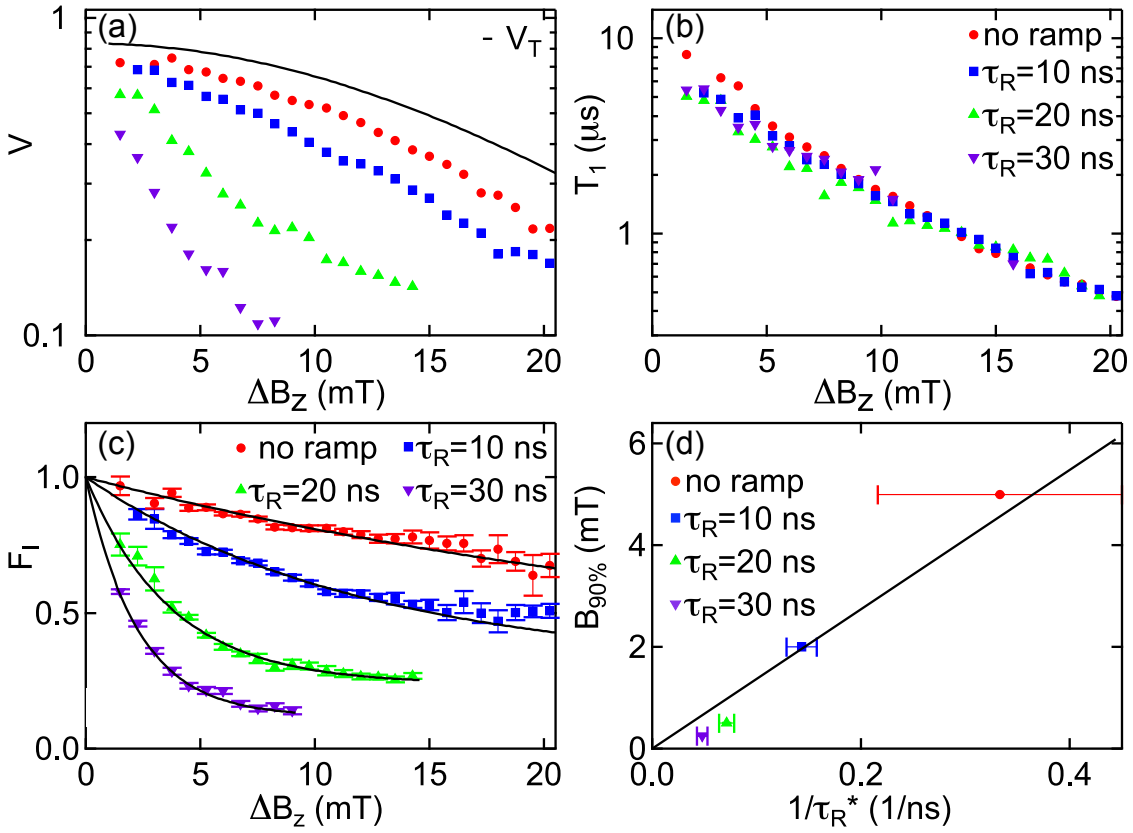

Figure 6.5: (Color online) (a) Measured Visibility, V, of $S-T_0$ precession over field gradient, ΔB_z, for precession experiments, in which the singlet is separated from energy detuning ϵ_M to ϵ_S over different ramp times τ_R. The expected total visibility, V_T, calculated from the measured relaxation time, T_1 (b), as discussed for Fig. 4(f), is shown as a solid line and does not depend on ramp time, τ_R. For $\tau_R = 40$ ns the $S - T_0$ precessions can no longer be clearly distinguished from the noise floor. (b) Singlet relaxation time, T_1, as function of nuclear field difference,$\Delta\ B_z$, showing no dependence on ramp time, τ_R. (c) Initialization fidelity, $F_I = V/V_T$, of (1,1) singlet as function of nuclear field gradient for different τ_R, calculated from data in (a). The solid lines are fits, $F_I = e^{-\Delta B_z/B_W} + F_0$, with a phenomenological width, B_W, to extract the initialization range, $B_{90\%}$, the field difference for which the singlet initialization fidelity is down to $F_I = 0.9$, see text. (d) Initialization range, $B_{90\%}$, the nuclear field difference, for which $F_I = 0.9$, as function of inverse effective ramp time, $1/\tau_R^*$, where $\tau_R^* \sim 0.7\,\tau_R$, see text. Extrapolation of the linear fit (solid line), see text, suggests that F_I is independent of$\Delta\ B_z$ for $\tau_R \to 0$. The effective ramp time for the data with no nominal ramp time is estimated to be $\tau_R^* \sim 3$ ns $\pm\, 2$ ns, and is set by the bandwidth of the coaxial cables.

6.7 Finite Pulse Rise-Time Effects, Singlet Initialization Fidelity

Comparison of the measured visibility, V, shown in Fig. 6.4(f), with the expected total visibility, V_T, from Eq. (6.8), calculated from measured triplet relaxation times, T_1, shows

qualitative agreement. The theory curve, V_{T}, slightly overestimates the measured visibility except for low values of$\Delta\ B_{\mathrm{z}}$. We speculate that this deviation is due to imperfect initialization (separation) and recombination of a singlet state, reducing the measured visibility,

$$V = V_{\mathrm{T}} F_{\mathrm{I}}. \tag{6.9}$$

The initialization fidelity, F_{I}, captures the reduction in visibility due to an admixture of the nuclear ground state because the separation of the singlet is not completely diabatic, see Fig. 6.2(b), and the analogous reduction because the recombination of the two electrons into one dot is not diabatic either. To test this hypothesis, pump-probe experiments with an intentional ramp time, τ_{R}, are performed. As discussed above, a 4 MHz pump-cycle is executed for 60 s. During the subsequent probe-cycles, a prepared singlet is separated from the (0,2) charge state at M to the (1,1) charge state at point S over the ramp time, τ_{R}. After evolution in the nuclear field difference,$\Delta\ B_{\mathrm{z}}$, the system is ramped back to the point M, over the same ramp time. The singlet measurement probability, P_S, is measured for the same parameters as the data in Fig. 6.4, and the triplet relaxation time, T_1, is measured as discussed for Fig. 6.4(b). As a control, a pump-probe experiment without nominal ramp is performed under the same conditions. The measured visibilities, V, are shown in Fig. 6.5(a), together with the expected visibility, V_{T}, calculated from the measured T_1, using Eq. (6.8) and following Ref. [Barthel 2009]. The relaxation time, T_1, does not depend on τ_{R} as shown in Fig. 6.5(b). The initialization fidelity, F_{I}, shown in Fig. 6.5(c), is calculated as the ratio, $F_{\mathrm{I}} = V/V_{\mathrm{T}}$, of measured and expected visibility. For larger ramp times, F_{I} falls off with$\Delta\ B_{\mathrm{z}}$ more rapidly. Due to the finite rise time of the pulses, the data with no nominal ramp time has an estimated effective ramp time, $\tau_{\mathrm{R}}^{*} \sim 3$ ns, and a fidelity, $F_{\mathrm{I}} < 1$, at finite nuclear field differences. For the data with nominal ramp times, the effective ramp time, $\tau_{\mathrm{R}}^{*} \sim 0.7\,\tau_{\mathrm{R}}$, is estimated from the fraction of the ramp that is spent in (1,1) at exchange energies, comparable to the Zeeman energy corresponding to$\Delta\ B_{\mathrm{z}}$. To characterize the decline in fidelity with$\Delta\ B_{\mathrm{z}}$, we define the initialization range, $B_{90\%}$, the maximum nuclear field gradient for which the fidelity, $F_{\mathrm{I}} \geqslant 0.9$. A phenomenological exponential curve is fitted to the fidelities shown in Fig. 6.5(c) to extract $B_{90\%}$, which

increases with increasing effective ramp rate, $1/\tau_{\mathrm{R}}^{*}$, as shown in Fig. 6.5(d)[4]. The increase in $B_{90\%}$ is approximately linear in $1/\tau_{\mathrm{R}}^{*}$. A linear fit, shown in Fig. 6.5(d) agrees reasonably well with the data. This suggests that the smaller than unity fidelity for the probe-cycle without nominal ramp time is due to the finite pulse rise time. For higher bandwidth coaxial cables, a larger singlet initialization fidelity may be obtained, even in the presence of magnetic field gradients. Moreover the $S - T_0$ precession data at finite ramp-times constitutes a weak measurement of the nuclear field gradient,$\Delta\ B_{\mathrm{z}}$, with the initialization fidelity, F_{I}, as coupling parameter [Aharonov 1988; Romito 2008].

6.8 Magnetic Field Dependence, alternative Interpretation of Unity Singlet Return Probability after nuclear Pumping

Pump probe experiments have been performed in six cool-downs of four devices for three different magnetic field directions, along all three crystal axes, indicated in Fig. 6.1(a), and at a wide range of magnetic field magnitudes between 10 mT and 2 T. For data shown in this paper, B is applied along the direction given in Fig. 6.1(a). At all fields, the same qualitative phenomenology, i.e. a nuclear field gradient and an average nuclear polarization of comparable magnitude, have been observed, while at no field value a suppression of nuclear field fluctuations was found. We speculate that the phenomenology reported in Ref. [Reilly 2008] was the result of a nuclear field gradient,$\Delta\ B_{\mathrm{z}}$, much larger than the equilibrium field fluctuations, suppressing the measurement visibility. Drifts of the measurement point M result in changes of sensor conductance and measurement visibility, that mimic a reduction of P_{S} for long separation times, as observed and interpreted as a T_2^{*} envelope in Ref. [Reilly 2008]. The fast, low-visibility precession would not be distinguishable from a

[4]The saturation values, F_0, used in fits in Fig. 6.5(c), may be spurious since visibilities are approaching the noise levels. Initialization range, $B_{90\%}$, is used to obtain a width insensitive to errors in low F_{I} values at high$\Delta\ B_{\mathrm{z}}$. For no ramp, $F_0 \sim 0.3$, $B_{\mathrm{W}} \sim 31$ mT; for $\tau_{\mathrm{R}} = 10$ ns, $F_0 \sim 0.3$, $B_{\mathrm{W}} \sim 12$ mT; for $\tau_{\mathrm{R}} = 20$ ns, $F_0 \sim 0.2$, $B_{\mathrm{W}} \sim 4$ mT; for $\tau_{\mathrm{R}} = 30$ ns, $F_0 \sim 0.1$, $B_{\mathrm{W}} \sim 2$ mT. In Fig. 6.5(d), the slope of the linear fit is ~ 14 mT ns.

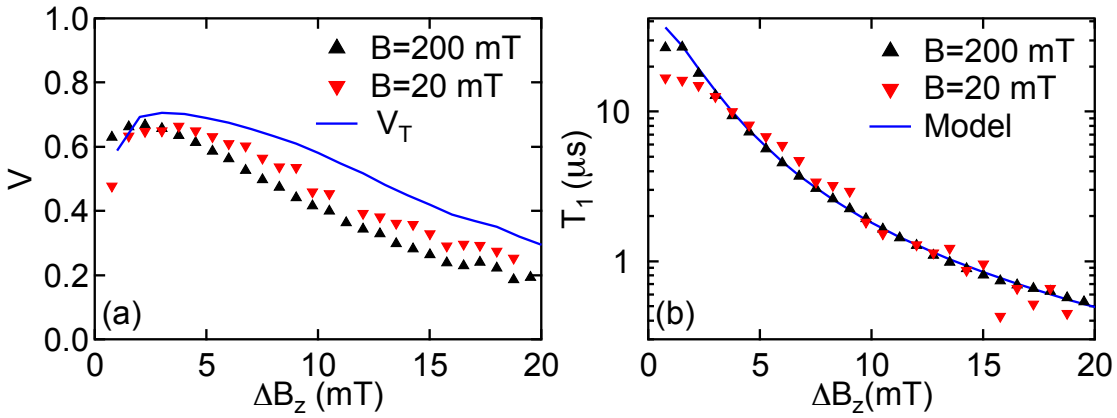

Figure 6.6: (Color online) (a) Parametric plot of measured visibility, V, shown in Fig. 3(f), against measured nuclear field difference,$\Delta\ B_z$, shown in Fig. 4(e), for two different applied magnetic fields, B. The solid line is the expected total visibility, V_T, from the simultaneously measured relaxation time, T_1, see Fig. 3(f). (b) Measured triplet relaxation time, T_1, as function of measured nuclear field difference,$\Delta\ B_z$, for two different applied magnetic fields, with the model, Eq. (6.3). The corresponding visibility is shown in (a) and the time dependence of polarization and visibility is shown in Fig. 3. The$\Delta\ B_z$ dependence of V and T_1 does not depend on the applied magnetic fields.

suppression of dephasing without the fast measurement techniques that are employed in this paper.

Different applied magnetic fields change the time constant at which nuclear polarizations decay, see Fig. 6.3. However the dependence of visibility, V, and triplet relaxation time, T_1, on the nuclear field difference, shown in Fig. 6.6(a) and (b), do not change with applied magnetic field, B.

6.9 Conclusion

In conclusion, a nuclear field gradient is always found for an electron nuclear spin pump-cycle. A magnetic field difference,$\Delta\ B_z$, reduces the relaxation time of a triplet state during the measurement and appears to furthermore degrade the initialization fidelity of a (1,1) singlet state that is separated from a (0,2) singlet with a finite ramp- or rise-time. The $S - T_0$ measurement visibility reduction due to field gradients offers an alternative explanation of the experiments discussed in Ref. [Reilly 2008], without requiring new physics or exotic nuclear states. For applications of spin qubits in quantum information pro-

cessing, where magnetic field gradients are promising tools in the realization of quantum gates [Foletti 2009; Pioro-Ladrière 2007], it is desirable to engineer the exchange profile to allow long triplet lifetimes, e.g. by having an (0,2) singlet-triplet splitting slightly larger than the measurement detuning. In the presence of a magnetic field difference, the device should be tuned to a large inter-dot tunnel coupling with a measurement point chosen at large detuning, where exchange protects the triplet and the charge relaxation rate is small. To mitigate errors from finite pulse rise times, an initialization of the qubit via an adiabatic initialization of $|\uparrow\downarrow\rangle$, followed by a $\pi/2$ pulse, may be preferable over the diabatic initialization used here and in Refs. [Petta 2005; Foletti 2009; Reilly 2007]. We would like to point out that the results of this paper do not imply a short relaxation time of the qubit while it is operated in the (1, 1) state, where T_1 is much longer and expected to be independent of magnetic field gradient [Amasha 2008].

Acknowledgments

We acknowledge funding from ARO/iARPA, the Department of Defense. This work was performed in part at the Center for Nanoscale Systems (CNS), a member of the National Nanotechnology Infrastructure Network (NNIN), which is supported by the National Science Foundation under NSF award no. ECS-0335765. We thank D.J. Reilly, J.M. Taylor and S. Foletti for useful discussion.

Chapter 7

Dynamic Decoupling and interlaced Operation of a Singlet-Triplet Qubit

C. Barthel[1,3] J. Medford[1,3] C. M. Marcus[1] M. P. Hanson[2] A. C. Gossard[2] [1]Department of Physics, Harvard University, Cambridge, Massachusetts 02138, USA

[2]Materials Department, University of California, Santa Barbara, California 93106, USA

[3] These authors contributed equally to this work.

We demonstrate interlacing of Carr Purcell (CP) spin echo sequences with coherent operations on a singlet-triplet qubit, formed by the spins of a two-electron GaAs double quantum dot. Qubit operations are performed using exchange and the Overhauser nuclear field difference between the two dots. The initial and final states of these operations are preserved from decoherence over tens of microseconds. Different decoupling sequences, Hahn echo (HE), CP, Concatenated dynamical decoupling (CDD) and Uhrig dynamical decoupling (UDD) are compared in their effectiveness to preserve an initialized singlet state. We find that for our system and setup the coherence time achieved employing a CP sequence is as high as for a CDD sequence and significantly higher than the time achieved with a UDD sequence, for similar numbers of π-pulses. Coherence times $\gtrsim 100$ μs are observed for a CP spin echo sequence [1].

---

[1]This chapter is adapted from a manuscript in preparation for submission [Barthel T2 2010].

7.1 Introduction

The singlet-triplet basis of a pair of electron spins in two coupled quantum dots has been suggested as a logical qubit for quantum information processing [Loss 1998; Levy 2002]. The qubit is inherently protected against collective dephasing [Levy 2002], and more importantly allows for all-electrical sub-nanosecond operations, using the exchange energy between singlet and triplet states to perform rotations around one of the qubit blochspere axes [Petta 2005]. Qubit rotations around a second independent axis, needed for universal qubit control, can be induced by a magnetic field difference between the two quantum dots, for example from a micro magnet on top of the double dot [Pioro-Ladrière 2007], and have recently been realized via a gradient in the nuclear polarization of the host material [Foletti 2009]. Fast measurement of a qubit state has been demonstrated for two-electron spin states [Meunier 2006; Barthel 2009], and also for single electron spin states [Elzerman 2004; Amasha 2008]. Aside from being a useful tool to manipulate the qubit, the Overhauser fields from the nuclei also are the major source of qubit dephasing [Petta 2005]. The fluctuations of nuclear fields have been shown to be slow [Reilly 2007], and a Hahn spin echo pulse sequence has been used to extend the coherence time of a singlet to up to ~ 30 μs [Hahn 1950; Petta 2005; Bluhm T_2 2010]. Carr Purcell (CP) spin echo pulse sequences have been used to extend qubit coherence times up to ~ 200 μs [Carr 1954; Meiboom 1958; Bluhm T_2 2010]. Theoretical work suggests that, under the assumptions of certain dephasing power spectra, spin echo sequences more complex than CP could further increase coherence times [Witzel CDD 2007; Uhrig 2007].

In this rapid communication we demonstrate the protection of a generalized singlet-triplet superposition from decoherence by interlacing qubit rotations about two different Bloch sphere axes into two CP spin echo pulse sequences. For nuclear Overhauser field driven rotations around the x-axis of the qubit Bloch sphere, and exchange energy driven rotations around the z-axis of the Bloch sphere, oscillations in singlet return probability are preserved up to 60 μs, comparable to singlet coherence times. Finally, we compare the coherence times of a singlet, protected by a single Hahn echo (HE), a CP echo sequence with 16 π-pulses [Carr 1954; Meiboom 1958; Bluhm T_2 2010], a 5th order Concatenated

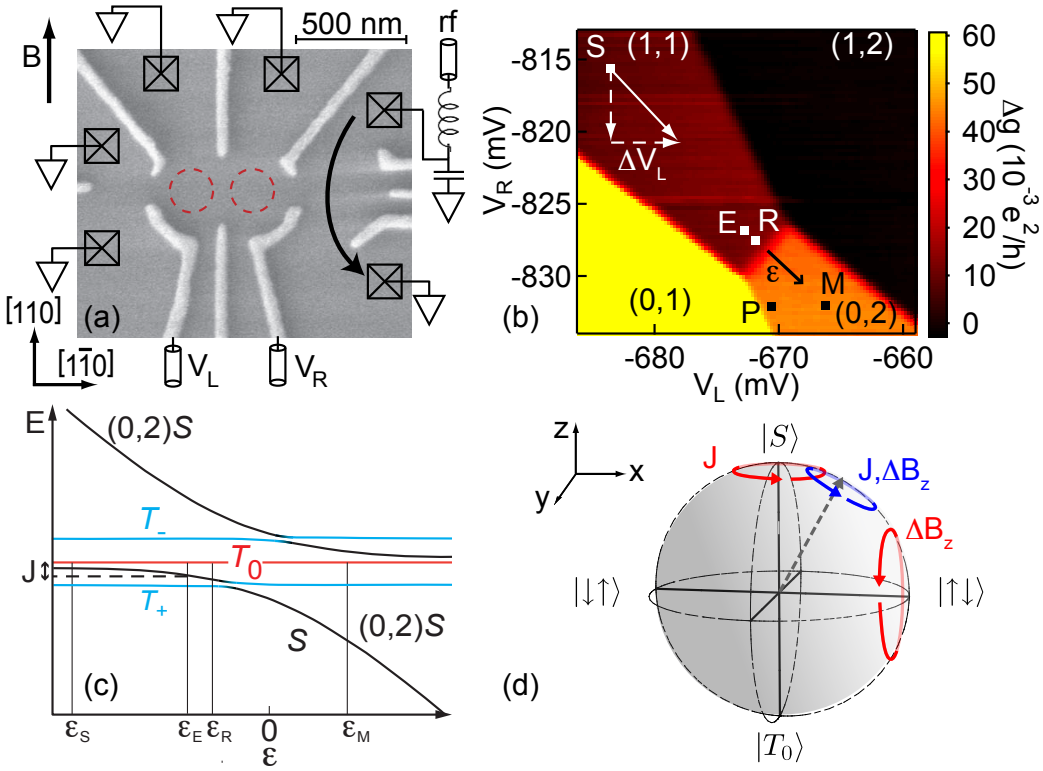

Figure 7.1: (a) (Color online) (a) Micrograph of lithographically identical device. Gate voltages, $V_{\rm L}$ and $V_{\rm R}$, set the electrostatic energy of left and right dot. A rf-sensor quantum dot (SQD) on the right allows to measure the double dot charge state. (b) SQD dc conductanceΔ g, with double dot charge state $(N_{\rm L}, N_{\rm R})$. The markers indicate gate voltage configurations during the experimental pulse-sequence. The detuning ϵ is controlled via voltage-pulsesΔ $V_{\rm L}$ andΔ $V_{\rm R}$ from the dc-average S, along the diagonal axis through the markers S, M. (c) Energy level diagram as a function of detuning, ϵ. Pulse-cycle detunings, $\epsilon_{\rm P}$ of singlet preparation, $\epsilon_{\rm E}$ of exchange oscillations, $\epsilon_{\rm R}$ of mapping ramps, and π-pulses, and $\epsilon_{\rm S}$ of dephasing configuration. (d) Bloch sphere of the singlet-triplet qubit, with mechanisms of rotation indicated, exchange energy, J, or a magnetic field difference,Δ $B_{\rm z}$, drive rotations around the qubit z-axis or x-axis respectively. A rotation around the z-axis by π (π-pulse) refocuses spin evolution [Hahn 1950].

dynamical decoupling (CDD) sequence with 21 π-pulses [Witzel CDD 2007], and a 22nd order Uhrig Decoherence Decoupling (UDD) sequence with 22 π-pulses [Uhrig 2007]. We find that for our system and setup the CP sequence is best suited to extend the coherence of an initial singlet in the studied system, yielding a coherence time equal to that for the CDD sequence with a larger number of pulses. The UDD sequence produces significantly shorter coherence times than CDD and CP.

7.2 System and Setup

The double quantum dot and sensor are defined by Ti/Au depletion gates on a GaAs / $Al_{0.3}Ga_{0.7}As$ heterostructure with a two-dimensional electron gas (density 2×10^{15} m^{-2}, mobility 20 m^2/Vs) 100 nm below the surface. An in-plane magnetic field, $B = 750$ mT, is applied perpendicular to the dot connection axis, as indicated in Fig. 7.1(a). Measurements were carried out in a dilution refrigerator (electron temperature ~ 150 mK), configured for high-bandwidth gating and rf reflectometry. As described elsewhere [Barthel SQD 2010; Reilly APL 2007], a proximal radio-frequency sensor quantum dot (rf-SQD) is sensitive to the charge state of the double dot, yielding an output signal, $v_{\rm rf}$, via reflectometry, with sub-microsecond time resolution. The charge state of the double quantum dot is controlled by gate voltages $V_{\rm L}$, $V_{\rm R}$ [see Figs. 7.1(a) and 7.1(b)], that can be pulsed on ns-timescale by a Tektronix AWG 5014 arbitrary waveform generator. The gate voltage configurations during pulse cycles are indicated by markers in Fig. 7.1(b). To reduce the effect of gate voltage drifts, the dc average of the gate voltages is set to the S, where the system spends the longest time during spin echo experiments, via a compensation pulse between measurement and preparation. Gate voltage drifts, due to capacitive coupling of the fast pulses, have been found to reduce qubit coherence times [Bluhm T_2 2010]. The qubit energies are set by the detuning, ϵ, controlled by settingΔ $V_{\rm L}$ andΔ $V_{\rm R}$ along the axis connecting the points M and S in Fig. 7.1(b). During the experimental pulse cycle, the plunger gate voltages are pulsed byΔ $V_{\rm L}$ andΔ $V_{\rm R} \sim -\Delta V_{\rm L}$ relative to the dc average at point S, to set the system to the configurations marked in Fig. 7.1(b).

7.3 Energy Level Diagram and experimental Pulse Cycle

To understand the evolution of the system during the experimental cycle, it is instructive to consider the energy level diagram as a function of detuning, ϵ, shown in Fig. 7.1(c). The system is prepared in a singlet state through relaxation into the (0,2) singlet at point P [Petta 2005]. Rapid separation of the electrons, by pulsing ϵ to $\epsilon_{\rm S}$, initializes a (1,1) singlet state, S. A slow, adiabatic sweep of ϵ from $\epsilon_{\rm R}$ to $\epsilon_{\rm S}$ maps a singlet, $S = (|\uparrow\downarrow\rangle - |\downarrow\uparrow\rangle)/\sqrt{2}$, onto the ground state of the nuclear Overhauser fields, $|\uparrow\downarrow\rangle$ [Petta 2005]. At $\epsilon_{\rm S}$, the resid-

ual exchange energy splitting, J_S, between singlet and triplet states is small, and the qubit precesses in the magnetic field difference,$\Delta\ B_z$, between the two dots. This precession constitutes a rotation around the x-axis of the qubit Bloch sphere, see Fig. 7.1 and Ref. [Foletti 2009] at frequency $f_S = |g^*|\,\mu_B \Delta B_z/h$, with the bulk g-factor of GaAs, $g^* = -0.44$. The magnetic field difference originates from the hyperfine interaction with GaAs nuclei, and data is post-selected for$\Delta\ B_z = 3$ mT from runs with randomly fluctuating nuclear fields. A second axis of rotation, along the z-axis of the Bloch sphere, is realized by pulsing the gate voltages from point S to point E, with an exchange energy, $J_E > |g^*|\,\mu_B \Delta B_z$ [Petta 2005; Foletti 2009]. Due to the magnetic field gradient,$\Delta\ B_z$, the rotation axis is slightly tilted away from the z-axis and the frequency is $f_E = 1/h\sqrt{J_E^2 + (g^*\mu_B \Delta B_z)^2}$. After evolution at ϵ_S andϵ_E, the projection of the final state onto the singlet is measured by rapidly pulsing the detuning to ϵ_M [Petta 2005; Barthel 2009]. If the qubit is in a singlet state, the two electrons are recombined into one dot, following the lower branch of the anticrossing at $\epsilon = 0$, while a triplet state remains locked in the (1,1) charge state [Petta 2005]. The qubit state is then inferred from the double dot charge state, measured via the conductance of the adjacent charge sensor [Petta 2005; Barthel 2009; Barthel SQD 2010].

A qubit at detuning ϵ_S is subject to dephasing due to interactions with the randomly fluctuating nuclear spins. Since the nuclear fields evolve slowly compared to pulse cycle durations [Reilly 2007], a spin echo, a π-rotation on the Bloch sphere, extends the coherence [Petta 2005; Bluhm T_2 2010]. The π-rotations are realized via z-rotations by pulsing the system to detuning ϵ_E. In a HE sequence, a π-pulse is performed after time $\tau_D/2$ spent at ϵ_S. The system is then rapidly brought back to S for the time $\tau_D/2$. Multiple π- pulses extend the coherence to longer times, as suggested in Refs. [Carr 1954; Meiboom 1958] and experimentally demonstrated in Ref. [Bluhm T_2 2010]. For the CP spin echo sequence, N_π π-pulses are performed, each with an equal dephasing and rephasing time, before and after the pulse [Carr 1954; Meiboom 1958]. For quantum information processing, arbitrary qubit states need to be protected from decoherence, and decoupling schemes known to preserve initial singlet states from dephasing need to be combined with operations. As an initial step towards that goal we interlace gate operations with CP spin echo sequences to preserve the state of the qubit.

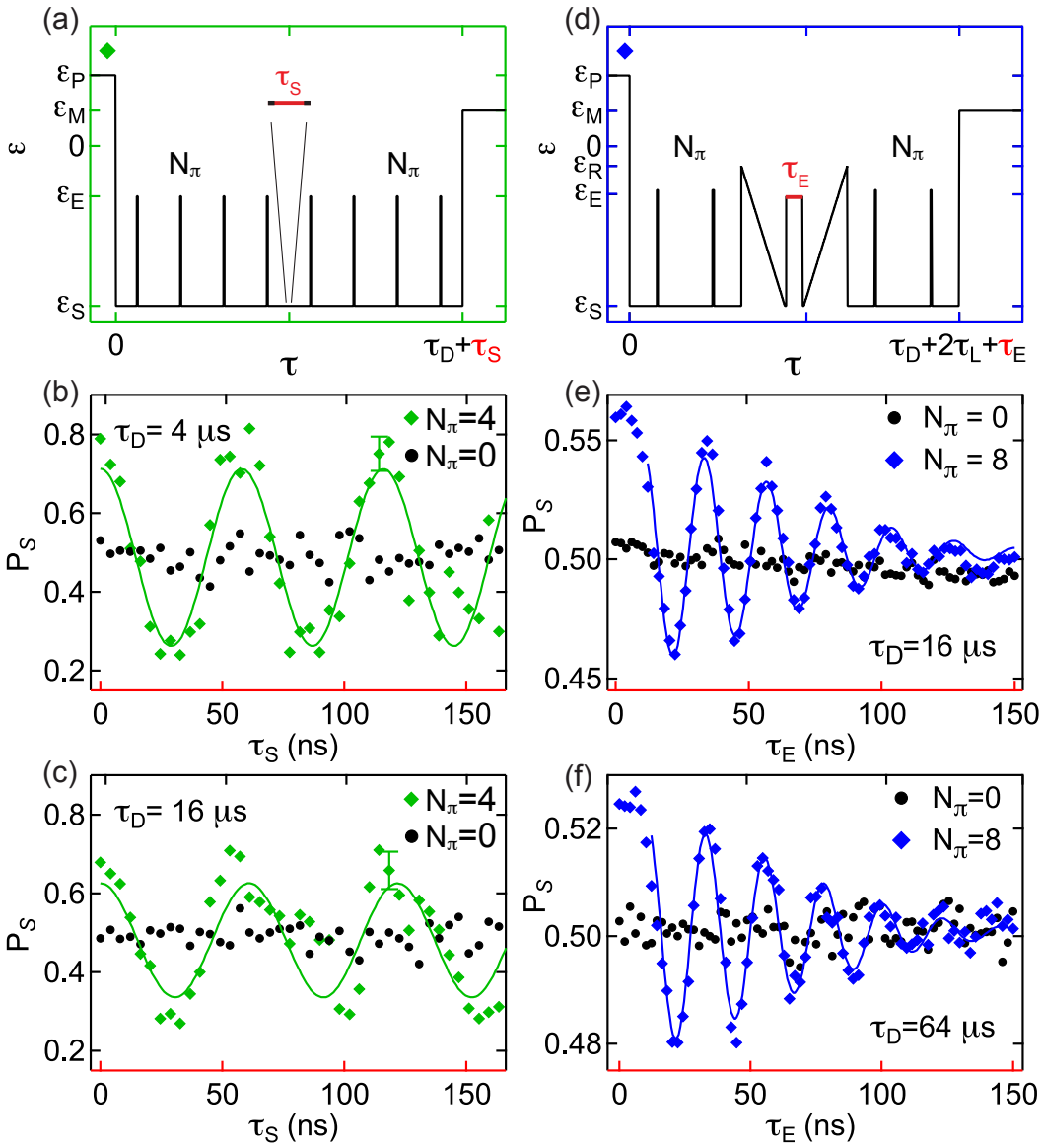

Figure 7.2: (a) Pulse sequence of ϵ, controlled byΔ $V_{\rm R}$, $\Delta V_{\rm L}$, cycling through $\epsilon_{\rm P}$, $\epsilon_{\rm S}$, $\epsilon_{\rm E}$, and $\epsilon_{\rm M}$. A free evolution at $\epsilon_{\rm S}$ is embedded in between two CP spin echo sequences with N_π π-pulses. (b) Singlet probability, P_S, as function of $\tau_{\rm S}$ for $N_\pi = 4$ (green, grey squares) and $N_\pi = 0$ (black circles), with $\tau_{\rm D} = 4$ μs. Cosine fit is shown as solid line, see text. Error bar is from Poissonian statistics of 100 single-shot measurements per probability. (c) Identical to (b) but $\tau_{\rm D} = 16$ μs. (d) Pulse sequence of ϵ. After an N_π-pulse CM sequence, a singlet state is mapped to $|\uparrow\downarrow\rangle$, by pulse to R and ramp back to S, before evolution at E for $\tau_{\rm E}$. Finally, $|\uparrow\downarrow\rangle$ ($|\downarrow\uparrow\rangle$) is mapped to S (T_0), N_π-pulse CP sequence preserves outcome, ϵ is pulsed to $\epsilon_{\rm M}$ to measure P_S. (e) Singlet probability, P_S, as function of $\tau_{\rm S}$ for $N_\pi = 8$ (blue, grey squares) and $N_\pi = 0$ (black circles), with $\tau_{\rm D} = 16$ μs, from 600×100 single-shot measurements, the solid line is a cosine fit with Gaussian envelope, see text. Poissonian error is smaller than markers. (f) Identical to (e) but $\tau_{\rm D} = 64$ μs.

7.4 Interlaced Operations

Interlaced x-rotations are demonstrated by placing a qubit operation time, τ_S, in between two CP spin echo sequences. The pulse sequence is schematically shown in Fig. 7.2(a), a singlet state is diabatically initialized, and a series of four Hahn echos forms a 4-pulse CP sequence, preserving the intial singlet state for the time $\tau_D/2$. Subsequently the operation time, τ_S, is spent at ϵ_S. The random but constant$\Delta\ B_z$ induces qubit rotation around the x-axis of the Bloch sphere, starting at a singlet state. The outcome of the x-rotation is preserved by a second 4-pulse CP sequence. Finally, the singlet probability, P_S, is measured from 100 single-shot outcomes [Barthel 2009; Barthel SQD 2010], after a rapid pulse to ϵ_M. Figure 7.2(b) shows the singlet measurement probability as a function of the operation time, τ_S, for a total dephasing time, $\tau_D = 4\ \mu$s. Equivalent data without π-pulses, effectively a free precession over 4 μs - 4.2μs, is shown as a control, and does not show oscillations in probability. Increasing τ_D to 16 μs decreases the visibility of the oscillations, as shown in Fig. 7.2(c). Rapidly ($\sim$ 1 Hz) repeated measurements show varying oscillation frequencies that are correlated for consecutive traces, as expected for nuclear field gradients. We note that the rotation frequency is random in these experiments, but post-selection, for$\Delta\ B_z \sim$ 3 mT in Figs. 7.2(b) and (c), is possible via fast single-shot measurements [Barthel 2009]. The oscillations are fitted well by the fit function $P_S = 0.5\ (1 + V\cos(\tau_S \Delta B_z g^* \mu_B/\hbar))$, with $\Delta B_z \sim 3$ mT, and with visibilites $V \sim 0.5$ and $V \sim 0.4$ in Figs. 7.2(b) and (c) respectively. The dephasing time, $T_2 \sim 40\ \mu$s, for 8 π-pulses, explains the ratio of the two visibilities. Accounting for the dephasing time and the ~ 0.7 visibility of $S - T_0$ precessions [2], without π-pulses and with $\tau_D = 0$, leaves a residual smaller than unity visibility $V_\pi \sim 0.9$, which we attribute to imperfection of the π-pulses due to tilts of the rotation axis by the nuclear field gradient, as illustrated in Fig. 7.1(d) [3].

[2]The visibility of bare $S - T_0$ precession is due to measurement fidelity, finite exchange at ϵ_S, and initialization.

[3]Finite J_S, ΔB_z result in eigenstates at S and E, and hence rotation axes, to be non-orthogonal, reducing visibility of exchange oscillations, and the fidelity of π-pulses. Increased π-pulse visibility is possible by using

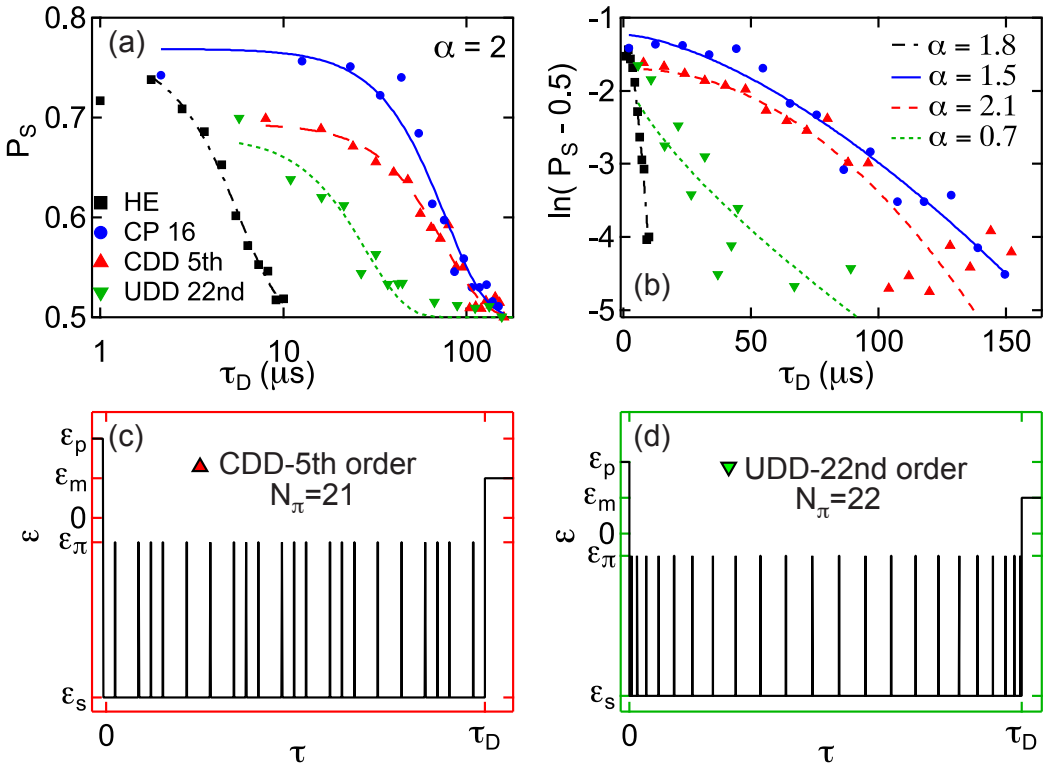

Figure 7.3: (Color online) (a) Echo recovery amplitude, P_S, as function of total dephasing time, $\tau_{\rm D}$, for Hahn echo, CDD, CP, UDD with fits, $P_S = 0.5\,(1 + V\,e^{-(\tau_{\rm D}/T_2)^2})$, yielding $T_2^{\rm HE} \sim 6$ μs, $T_2^{\rm CDD} \sim 80$ μs, $T_2^{\rm CP} \sim 80$ μs, $T_2^{\rm UDD} \sim 30$ μs. See text for other parameters. (b) Logarithmic plot of data in (a) with power law fits extracting the best fit power α in the decay law $P_S = 0.5\,(1 + V\,e^{-(\tau_{\rm D}/T_2)^{\alpha}})$, see text for other parameters.(c) Pulse sequence of ϵ, controlled byΔ $V_{\rm R}$, $\Delta V_{\rm L}$, cycling through detunings $\epsilon_{\rm P}$, $\epsilon_{\rm S}$, $\epsilon_{\rm E}$, and $\epsilon_{\rm M}$, for the 5th order CDD sequence. (d) Pulse sequence of ϵ for 22nd order UDD sequence.

Interlaced qubit rotations around the z-axis are demonstrated, using the pulse sequence illustrated in Fig. 7.2(d). A singlet state is diabatically initialized, followed by an 8-pulse CP sequence. The singlet, protected by the initial CP sequence, is adiabatically loaded into the state $|\uparrow\downarrow\rangle$, by rapidly pulsing the detuning from $\epsilon_{\rm S}$ to $\epsilon_{\rm R}$, and slowly ramping back to $\epsilon_{\rm S}$. A rotation around the Bloch sphere z-axis is now realized by a fast gate-pulse to $\epsilon_{\rm E}$, where the qubit oscillates at frequency $f_{\rm E}$ over the time $\tau_{\rm E}$, before the gates are pulsed back to S. A slow ramp of detuning from $\epsilon_{\rm S}$ to $\epsilon_{\rm R}$, followed by a rapid jump back to S, maps states $|\uparrow\downarrow\rangle$ / $|\downarrow\uparrow\rangle$ onto singlet / triplet. Note that the phase is not perfectly conserved, as this mapping procedure is not unitary. For use in a quantum computation scheme the transition between S and $|\uparrow\downarrow\rangle$ would be replaced by a x-rotation via controlled

larger $J_{\rm E}$, via increased inter-dot tunnel coupling.

ΔB_z, as realized in Ref. [Foletti 2009]. The singlet-triplet superposition, with amplitudes resulting from the z-rotation encoded in its probability amplitudes, is preserved over a time $\tau_D/2$ by a second 8-pulse CP sequence. The singlet probability is measured via a diabatic pulse to ϵ_M, as discussed above, and subsequently averaged over 600 runs to yield an electron- and nuclear ensemble. Figure 7.2(e) shows the singlet measurement probability for a total dephasing time $\tau_D = 16$ μs, with 8-pulse CP before and after the z-axis rotation, as function of the rotation time, τ_E. A control experiment without spin echoes (black markers) shows no oscillations. Equivalent data for $\tau_D = 64$ μs is shown in Fig. 7.2(f). A fit of $P_S = 0.5\left(1 + V\cos\left(J_E/\hbar\tau_E\right)e^{-(\tau_E/T_2^*)^2}\right)$ agrees well with the data, and yields $J_E \sim 0.2$ μeV, and $T_2^* \sim 100$ ns due to gate and charge noise during the exchange operations and shifts in oscillation frequency and -axis due to the fluctuatingΔ B_z, see Fig. 7.1(d). The visibilities, $V \sim 0.09$ for Fig. 7.2(c), and $V \sim 0.06$ for Fig. 7.2(c), are rather low [4]. The visibility of bare exchange oscillations is $V \sim 0.3$, because of finiteΔ B_z during exchange rotation, and J_S at ϵ_S [5]. The remaining loss in visibility is due to $T_2 \sim 80\mu$s, the smaller than one fidelity of the mapping pulse, and of the 16 π-pulses [5]. A larger tunnel coupling between the quantum dots should enable significantly higher visibilities.

7.5 Comparison of different Decoupling Sequences

Performing a CP spin echo sequence strongly improves the coherence time of a separated singlet, from $T_2^{HE} \sim 6$ μs for a single Hahn echo to $T_2^{CP} \sim 80\mu$s for a CP sequence with 16 π-pulses. A singlet is initialized by a diabatic gate-pulse to ϵ_S, after a Hahn (CP) echo with total time τ_D spent at S, the singlet echo recovery amplitude, P_S, is measured as the percentage of singlet outcomes via a fast gate-pulse to ϵ_M [Petta 2005; Hahn 1950]. The singlet echo recovery amplitude, measured from an ensemble of single-shot measurements, is shown

[4] An offset $t_0 \sim 10$ ns, due to finite pulse-rise time is taken into account for the fit.

[5] Finite J_S, ΔB_z result in eigenstates at S and E, and hence rotation axes, to be non-orthogonal, reducing visibility of exchange oscillations, and the fidelity of π-pulses. Increased π-pulse visibility is possible by using larger J_E, via increased inter-dot tunnel coupling.

in Fig. 7.3(a) with an empiric fit of $P_{\rm S} = 0.5\left(1 + Ve^{-\tau_{\rm D}^2/T_2^2}\right)$ [6]. The mechanism of singlet dephasing determines the functional form of the falloff; $P_S = 0.5\left(1 + V\, e^{-(\tau_{\rm D}/T_2)^\alpha}\right)$ is a more general dephasing time dependence. For a white dephasing spectrum one expects an exponential decay, $\alpha = 1$ while for coherence solely limited by hyperfine interaction $\alpha \sim 4$ is expected [Witzel 2006; Yao 2006], and has been experimentally observed [Bluhm T_2 2010]. We perform a power law fit to the logarithm of the singlet probability, as shown in Fig. 7.3(b). For both the HE and CP pulse sequence the best fit is in reasonable agreement with a Gaussian, with $\alpha^{\rm HE} \sim 1.8$ and $\alpha^{\rm CP} \sim 1.5$. These powers and comparison of coherence times to Ref. [Bluhm T_2 2010] suggest that the coherence time is limited by inhomogeneous broadening due to gate voltage drifts and noise shifting the electron wavefunction in the nuclear field gradient. For a 32-pulse order CP sequence a coherence time of $T_2^{\rm CP} \sim 120$ μs is realized in the device discussed in this paper, while in Ref. [Bluhm T_2 2010] a coherence time $T_2 \sim 200$ μs has been realized.

In Ref. [Witzel CDD 2007] and Ref. [Uhrig 2007] it has been suggested that more complex pulse sequences outperform a CP pulse sequence for a similar number of π-pulses. The CDD pulse sequence of nth order is recursively created from two sequences of $(n-1)$th order with an additional π-pulse in between them for odd n, the first order is a regular Hahn-echo, and the 2nd order is identical to a CP sequence with two π-pulses. The pulse cycle with a 5th order CDD sequence, with a total number of 21 π-pulses, is shown in Fig 7.3(c). The nth order UDD sequence is created, by placing n π-pulses at times $\delta\tau = \tau_{\rm D}\, \sin^2\left[j\pi/(2n+2)\right]$, where j is the index of the π-pulse. is shown for $n = 22$ in Fig 7.3(d). Singlet echo recovery amplitudes for the 5th order CDD and 22nd order UDD sequence are shown in Fig. 7.3(a) with Gaussian fits, yielding $T_2^{\rm CDD} \sim 80\mu$s for the CDD sequence and $T_2^{\rm UDD} \sim 30$ μs for the UDD sequence [7]. The CDD sequence, with a higher number of π-pulses, does not

[6] Other parameters in Fig. 7.3(a) are: $V^{\rm HE} \sim 0.6$, $V^{\rm CP} \sim 0.6$, $V^{\rm CDD} \sim 0.4$, $V^{\rm UDD} \sim 0.4$. Other parameters in Fig. 7.3(b) are: $V^{\rm HE} \sim 0.6$, $T_2^{\rm HE} \sim 5$ μs; $V^{\rm CP} \sim 0.6$, $T_2^{\rm CP} \sim 70$ μs; $V^{\rm CDD} \sim 0.4$, $T_2^{\rm CDD} \sim 80\mu$s; $V^{\rm UDD} \sim 0.4$, $T_2^{\rm UDD} \sim 17$ μs.

[7] Other parameters in Fig. 7.3(a) are: $V^{\rm HE} \sim 0.6$, $V^{\rm CP} \sim 0.6$, $V^{\rm CDD} \sim 0.4$, $V^{\rm UDD} \sim 0.4$. Other parameters in Fig. 7.3(b) are: $V^{\rm HE} \sim 0.6$, $T_2^{\rm HE} \sim 5$ μs; $V^{\rm CP} \sim 0.6$, $T_2^{\rm CP} \sim 70$ μs; $V^{\rm CDD} \sim 0.4$, $T_2^{\rm CDD} \sim 80\mu$s;

yield a longer coherence time than the CP sequence, while the coherence time achieved for the UDD sequence is significantly shorter than for CDD and CP. The discrepancy to the improvement predicted for UDD in Ref. [Uhrig 2007] may be due to gate voltage drifts[8] as discussed in Ref. [Bluhm T_2 2010], or due to the assumption of an ohmic dephasing power spectrum with a sharp cutoff in Ref. [Uhrig 2007], while the actual power spectrum is of form $\propto 1/f^2$ [Reilly 2007]. For a dephasing power spectrum closer to the experiment the optimal spin echo pulse sequence has been predicted to be very similar to a simple CP sequence [Pasini 2009], while in Ref. [Lee 2008] it was found that UDD is the optimal sequence for nuclear dephasing in GaAs quantum dots.

Acknowledgments

We acknowledge funding from ARO/iARPA, the Department of Defense. This work was performed in part at the Center for Nanoscale Systems (CNS), a member of the National Nanotechnology Infrastructure Network (NNIN), which is supported by the National Science Foundation under NSF award no. ECS-0335765. We thank Hendrik Bluhm, Sandra Foletti, David Reilly and W. Witzel, for useful discussion.

$V^{\mathrm{UDD}} \sim 0.4$, $T_2^{\mathrm{UDD}} \sim 17$ μs.

[8] Due to the irregular spacings of π-pulses, $\delta\tau_{\mathrm{j}+1} - \delta\tau_{\mathrm{j}}$, the UDD sequence may be more sensitive to drifts and finite rise times of the pulsed gate voltages.

Appendix A

Fabrication of Nano-Scale Quantum Dot Devices

A.1 Overview

In this appendix, I am discussing the fabrication recipe that I used, in its most recent version, from **November 07 2006**, given in a step by step guide, that can be easily reproduced. The devices measured in chapters 3, 4, 5, 6, 7 were all fabricated using the recipe discussed below.

In one of the two devices in chapter 3 a second metal layer, Permalloy with 84% Nickel and 16% Iron, was deposited on an insulator layer, to create a micro-magnet on top of the double dot device. The method used to fabricate the micro-magnet and the difficulties of the process are discussed in section A.3. For the fabrication back in 2007 the "Raith" e-beam writer was used. Also see Jeff Miller's e-beam guide (available on Marcus group website [1], under member information).

A.2 Fabrication of Double Quantum Dots

Fabricating quantum dot devices requires patience, discipline and a high tolerance for frustration. The process involves many steps (see section A.4) during any of which the device can be ruined, due to trivial incidents. I found that it is important not to cut corners

[1] marcuslab.harvard.edu

and to religiously follow the recipe. Small deviations can not only result in failure, but they will also make the process less comparable to previous and following attempts, making trouble-shooting impossible.

I fabricated all devices discussed in chapters 3 - 7, using the wafer G050329A, grown by Micah Hanson in the Gossard group at University of California Santa Barbara. This wafer showed very good behavior, few switching noise and high reproducibility between cool-downs.

During Titanium deposition it is important to increase the thermal evaporator power slowly when heating up boat and material, as the boat may otherwise break. Blow-drying with nitrogen gas should only be performed with the chip firmly but gently pressed against a cleanroom wipe. The recipe for metal layer photolithography (see section A.4) has a comparably low yield ($< 80\%$) which is problematic, because this process needs to be performed twice. One of these steps has to be performed at the very end of the fabrication process, which may ruin a week of work. I recommend to replace this process by a different process of metal deposition that produces an undercut without the need for the photo-resist LOR3.

A.3 Magnetic Top Layer

The magnetic top layer is the most difficult step in the fabrication of the double dots with micromagnets (CB3), on which part of the experiments described in chapter 3 were performed. On top of one of the devices in chapter 3 Permalloy (84% Ni, 16% Fe) was deposited via thermal evaporation using the CNS evaporator TE4. In the following I list a few suggestions for future generations of quantum dot devices with micromagnets.

- The Permalloy quite quickly degrades the boats of the evaporator, so it is hard to deposit more than 100 nm (400 nm are optimal to maximize the magnetic field gradient [Monzon 1997].). Keeping the deposition rate as low as possible (< 1 Å/s) reduced this problem slightly.
  - One solution may be to use electron beam evaporation to deposit the Permalloy.

  - A better solution may be to switch to Cobalt or a different single-element ferromagnet.
  - A different boat material or thickness may help too. For the fabrication of CB3 two 0.015" Tungsten boats were used.

- The Permalloy cracks the insulator layer, therefore only a small (micron-size) micromagnet was deposited on CB3. The e-beam connector layer is made from Titanium-Gold. (Separate e-beam exposure and metal deposition are necessary for the ~ 50 μm micromagnet and the ~ 500 μm Ti-Au connector layer.) The photolithography bond pad layer connecting to the connector layer and used to ground the micromagnet is also as made from Titanium-Gold.

- The magnetic field gradient was rather small, and potentially absent on some of the devices.
  - One solution may be to use electron beam evaporation to deposit the Permalloy.
  - A better solution may be to switch to Cobalt or a different single-element ferromagnet.
  - A different boat material may help too.
  - A thicker anti-oxidation layer of gold on top of the micromagnet may better prevent surface oxidation.
  - I suggest a change to the design in Ref. [Pioro-Ladriere 2008], which creates a $\gtrsim 2\times$ larger magnetic field gradient for equal thickness and material.

A.4 Fabrication Recipe

Mesa Etch

- prepare 2 chips, real chip and GaAs junk
- 1 a) Photolithography - one layer S1813 - see Photolithography-Mesa-Recipe
- 5 b) Plasma-Clean 5 s, 110 W (directly before etch)
- 1 c) Mesa-Etch - see Mesa-Etch recipe

Ohmic contacts

- 2 a) Photolithography - one layer LOR3, one layer S1818 - see Photolithography-Recipe
- 2 b) Oxygen Plasma-clean 110 W, 5 s
- 2 c) Metal deposition - see Ohmics-Metal-deposition
- 2 c) Liftoff in SVC 175 at 80 degree Celsius until liftoff complete (< 1hour) - see Liftoff
- 2 d) Clean in IPA for 5 mins, blow-dry with Nitrogen
- 2 e) Thermal Annealing - see Ohmics-Annealing-Instructions

3. and 4. Gates and connector-layer

- If the chip has few devices combine step 3. and 4.
- Do the e-beam step of 3.
- Switch to the 120 micron aperture and do step 4.
- Then deposit both together in one evaporation
- For 22 devices of the double-dot -ESR kind (04/07/06-Chris-ESR) the gates take 55 minutes of writing, the connection layer writes in 20 minutes - The device CB4 takes 3.1 minutes each at dose 1.48*250 (numbers for Raith)
- Scale and plan accordingly

3. Gates

- 3 a) Do a dose-test on junk-GaAs-material - see E-Beam-Recipe and Dose-Test-Instructions
- 3 b) Do real E-Beam exposure, using the optimum parameters from dose-test - see E-Beam-Recipe
- 3 c) Develop in 1:3 MIBK:IPA for 60 s, IPA for 30 s, blow-dry

- 3 d) UV-ozone clean in prep-room hood 120 s (when using PMMA 950K A4, for C3 do 60s)
- 3 e) Metal deposition 50 Angstrom Ti, 150 Angstrom Gold - see gates metal deposition
- 3 f) Liftoff in Acetone > 2 hours (ideally overnight)

NO SONICATION AFTER THIS STEP - only emergencies

4. Connector layer

- 4 a) Expose the connector layer using the 120 micron aperture, either use multiplier 1.4 or result from dose-test in step 3 a) (Bigger features tend to need less dose though)
- 4 b) Develop in 1:3 MIBK:IPA for 60 s, IPA for 30 s, blow-dry
- 4 d) UV-ozone clean in prep-room hood 120 s
- 4 e) Metal deposition 50 Angstrom Ti, 150 Angstrom Gold
- 4 f) Liftoff in Acetone > 2 hours (possibly overnight)

5. Photolithography layer

- 5 a) Photolithography - one layer LOR3, one layer S1818 - see Photolithography-Recipe
- 5 b) Plasma-Clean 5 s, 110 W (directly before Metal deposition)
- 5 c) Metal deposition - see Photolithography-Metal-Deposition-Insctructions
- 5 d) Liftoff in SCV 175 at 80 degree Celsius < 1 hr - see Liftoff
- 5 d) Clean in IPA for 5 minutes, blow-dry

Below here only for 2 - layer chips

6. Insulator-Layer (if a second metal layer is needed)

- 6 a) 3 -solvent clean, no sonication
- 6 b) Test deposition of 35 nm (ESR) on junk GaAs and Silicon - see ALD-Instructions
- 6 c) Observe GaAs layer under microscope, check homogeneity
- 6 d) Measure thickness of layer on Silicon chip with ellipsometer
- 6 e) Scale number of cycles according to height deviations
- 6 f) Deposit on real chip - see ALD-instructions

7. Top-gates

- 7 a) Perfor dose-test on previously insulator-deposited junk GaAs - 10 micron aperture - see E-Beam-Recipe
- 7 b) Do real E-Beam exposure, using the optimum parameters from dose-test - see E-Beam-Recipe at 10 micron - Magnetic-Ebeam-Recipe
- 7 d) Develop in 1:3 MIBK:IPA for 120 s, IPA for 10 s, blow-dry
- 7 e) UV-ozone clean in prep-room hood 120 s (for PMMA 950 K A4)
- 7 f) Metal deposition of 5 nm of Titanium, 250 nm Permalloy at < 0.1 nm/s and a 15 nm of Gold as a anti-oxidation cap, see Magnet-Layer-Metal-Deposition-Recipe
- 7 g) Liftoff in Acetone > 12 hours

8. Connector layer

- 8 a) Expose the connector layer using the 10 micron aperture, either use multiplier 1.4 or result from dose-test in 7 a) (Bigger features tend to need less dose though) see E-Beam-Recipe
- 7 d) Develop in 1:3 MIBK:IPA for 120 s, IPA for 10 s, blow-dry
- 7 e) UV-ozone clean in prep-room hood 120 s (for PMMA 950 K A4)
- 7 f) Metal deposition of 5 nm of Titanium, 250 nm Gold at < 0.1 nm/s , see Magnet-Layer- Metal-Deposition-Recipe
- 7 g) Liftoff in Acetone > 12 hrs

9. Magnetic photolithography layer

- 9 a) Photolithography - 1 layer LOR3, one layer S1818 - see Photolithography-Recipe
- 9 b) Plasma-Clean 5 s, 110 W(directly before Metal deposition)
- 9 c) Metal deposition - see Photolithography-Metal-Deposition-Instructions
- 9 d) Liftoff in SCV 175 at 80 degree Celsius < 1 hr - see Liftoff
- 9 d) Clean in IPA for 5 minutes, blow-dry

A.5 Detailed Fabrication Steps

1. Device photolithography for mesas

1.1 Switch on mask aligner

- Let Lamp warm up for $>$ 30 minutes.

1.2. Three solvent clean

Sonicate during all three solvent cleans.

1. TCE 5 mins
2. Acectone 5 mins
3. IPA 5 mins
4. Blow-dry with compressed Nitrogen gas, careful not to blow away chip - press chip down on paper

1.2. Singe on center of a hotplate at 200 degree Celsius for 5 mins

1.3. Spin resists

- Spin junk chip first.

- Cover drain of spinner!

1. Spin 1813
    - 500 RPM for 5 s (1 s spin-up)
    - 4000 RPM for 60 s (1 s spin-up)
2. Bake @ 115 degree Celsius for 2 mins

1.4. Develop

1. Use mask aligner to perform photolithography with appropirate mask, expose for 4 seconds
2. Rinse in CD 26 for 60 seconds
3. Rinse in DI water for 20 secs
4. Blow dry with compressed Nitrogen gas

1.5. Finish and prepare for etch

1. Observe under RED FILTER optical microscope or under alignment microscope
2. Plasma-Clean @ 110 W for 5 secs (at about 0.9 Torr before discharge starts)

Starting over, in case of accident

Just do a 3-solvent clean with sonication → chip will be clean.

2. Mesa-etch-recipe

2.1. Mixing

- Get H_2O_2 bottle from refrigerator, and Marcus-glass-ware box
- mix 1:8:240 H_2SO_4:H_2O_2:H_2O, stir
- prepare one to two beakers of DI water

2.2. If you do not know the approximate etch-rate

(e.g. if you have not used the chemicals recently)

- Do etching procedure (2.3.) on a GaAs junk chip first
- Determining etch-rate by measuring time, and the etched depth (via profilometer)
- If you know the material well, skip and directly proceed with real chip

2.3. Etch

1. Measure and write down the height of 4 mesa-resist piles at opposite edges of chip
2. Dunk chip into solution for time t, where $t = h/(3\,a)$
   - h is the desired height (for 110 nm 2DEG depth $\sim$ 140 nm)
   - a is the known (or measured on junk chip) etch rate
   - My last etch: $a = 128\text{nm}/43\text{ s}$
3. use profilometer to measure the four mesas measured before etch
4. recalculate a and proceed with second etching step, for $t = h/(2\,a)$, where h is the distance still missing
5. When desired height is reached, liftoff resist in acetone for 5 mins in sonication, clean in IPA, blow-dry
6. Measure height of mesas, calculate average a

2.4. Clean up and bring H_2O_2 back to fridge

3. Photolithography for metal liftoff

(for Ohmic contacts or top gate contact layer)

3.1 Switch on Mask aligner

- Let Lamp warm up for > 30 minutes.

3.2. Three solvent clean

Sonicate during all three solvent cleans.

1. TCE 5 mins
2. Acectone 5 mins
3. IPA 5 mins
4. Blow-dry with compressed Nitrogen gas, careful not to blow away chip - press down on paper

3.2. Singe on center of a hotplate at 200 degree Celsius for 5 mins

3.3. Spin resists

- Spin junk chip first.
- Cover drain of spinner!

1. Spin LOR3A
    - 500 RPM for 5 s (1 s spin-up)
    - 4000 RPM for 60 s (1 s spin-up)
2. Bake @ 170 degree Celsius for 5 mins
3. Spin S1818
    - 500 RPM for 5 s (1 s spin-up)
    - 4500 RPM for 60 s (1 s spin-up)
4. Bake @ 115 degree Celsius for 2 mins

3.4. Develop

1. Use mask aligner to perform photolithography with appropriate mask, expose for 4 seconds
2. Rinse in CD 26 for 60 seconds keep it steady
3. Rinse in DI water for 20 secs
4. Blow dry with compressed Nitrogen gas
5. Bake @ 125 degree C for 5 mins
6. Rinse in CD 26 for 1 min, keep sample steady
7. Rinse in DI water for 20 secs
8. Blow-dry with compressed Nitrogen gas

3.5. Finish and prepare for metal deposition

1. Observe under RED FILTER optical microscope
2. Plasma-Clean at 110 W power, for 5 secs (at about 0.9 Torr, before discharge starts)

4. Metal-deposition for ohmic contacts

- DO A JUNK CHIP FIRST

4.1 Electron-beam plasma clean

- 5s at 110 W
- Do NOT do UV-clean instead!

Minimize time between 4.2. and 4.3.!

- Perform 4.2 and 4.3 for junk-chip first, then for the real chip
- Prepare Metal deposition before etching in step 2. (vent and open evaporator EE3)

4.2. Ammonium-Hydroxide-etch

1. Fill glass beaker with Ammonium-Hydroxide from 30% bottle (29 % works too)
2. Dip chip into glass beaker with base for 2 seconds - use timer!
3. Clean in DI water and blow-dry thoroughly

4.3. Prepare metal deposition

1. Attach chip to holder with double sided tape, make the tape dirty (otherwise chip does not come off)
2. Open evaporator and confirm metal positions / place Marcus sources into evaporator
3. Load sample into evaporator, pump down below 10^{-5} mbar

4.4. Metal gas-out

- When pressure reached low 10^{-6} mbar, switch on power supply
- Gas out all sources by evaporating a few nanometers each (with shutter closed!)

4.5. Evaporate metal

- Wait for pressure to go down again, then deposit:

1. 5 nm of Pt at 0.1 nm/s
2. 160 nm of Au at 0.3 nm/s
3. 80 nm of Ge at 0.25 nm/s

4. 53 nm of Pt at 0.15 nm/s
5. 51 nm of Au at 0.3 nm/s

4.6. Unload sample after switching off power, and venting

5. Metal liftoff for photo-lithography layers

1. Prepare SVC 175
   - let sit on hotplate at 80 deg Celsius for $>$ 5 minutes
2. Liftoff - CHIP MUST NOT GET DRY!
   (a) Lower chip in SVC
   (b) Check after 20 mins, squirt IPA onto submerged chip (Do not let it dry!)
   (c) Park chip in IPA, replace SVC
   (d) Observe chip (still in IPA) under microscope
   (e) Go on in steps of 10 mins / 20 mins, repeating the IPA / replacement step until liftoff complete
   (f) Observe in IPA to check whether the metal has indeed been completely lifted off and that there are no LOR stains
   (g) Throw in fresh SVC for 5 mins, if there is metal or resist left
3. Leave in IPA for 5 mins
4. Blow-dry

6. Annealing of ohmic contacts

1. Switch On Annealer
2. Put in junk material with metal film on top
   - choose recipe CB1, which is just Jason's JRP1 copied over in early June 06
   - check recipe - should go up to 525 deg Celsius
   - pay attention that the actual temperature reaches the set temperature during test-run
   - take out chip after cooldown is finished
3. Observe under microscope - should look like the chip in the notebook (not cleanroom) from 04/11/06 "bubbly"
4. repeat 2. with real chip
5. Switch off Annealer

- Test Ohmic contacts in 4 K dunker

7. Electron beam recipe

7.1. Three solvent clean, if this is the first e-beam layer

Sonicate during all three solvent cleans.

1. TCE 5 mins
2. Acectone 5 mins
3. IPA 5 mins
4. Blow-dry with compressed Nitrogen gas, careful not to blow away chip - press down on paper

7.2. Prebake at 170 degree C for 2 minutes

7.3. Spin 950k PMMA A4

- Spin 500 R.P.M. for 5 seconds, 1 second spin-up - Put on resist in this step
- Spin 4000 RPM for 60 seconds with a 1k/second acceleration.

7.4. Bake for 15 minutes at 170 degree C

7.5. Load sample into the Raith.

Put a small amount of silver paint on the corners of the chip for coarse focusing, do not use Acetone to solve paint. Let dry for 5-10 minutes.

7.6. Tune up the Raith

Follow Jeff Miller's e-beam guide. See Marcus lab member information page.

7.7. Expose pattern

- Use Voltage 30 kV, Area dose = 250, line dose = 1500, step size of 6 nm.
- For gates use 10 micron aperture and do focusing on burnt spots (see Jeff's e-beam guide)
- For connector layer use 120 micron aperture and 20 nm step size
- Focus roughly at 10 micron and save the positions. (With the 120 aperture the beam exposes too fast, rough focusing on alignment marks is sufficient.)

Remark on dose tests

Expose a dose matrix with a dose factor ranging from 1 to 2 (or 2.2) in steps of 0.04. Expose the first dose-test over a 50x50 microns. For the remainder of the dose test restrict the pattern to 10 x 10 microns around the center. This way, the dose test runs faster. (see dose test instructions)

7.8. Expose features

- Create position-list according to translations between mesas on chip.
- Use one of the alignment marks as zero-point of your coordinate system.

7.9. Develop for 60 seconds in 1:3 MIBK:IPA

7.10. Rinse in IPA for 30 seconds and blow dry.

7.11. UV ozone clean

Using the cleaner in Marcus lab sample prep-room hood for 120 seconds.

7.12. E-Beam evaporation, immediately after previous step.

Using TE-3 or TE-5 in CNS cleanroom.

- 50 angstroms of Ti at 0.5 Angstrom per second.
- 150 angstroms of Au at 0.5 Angstroms per second.

7.13. Liftoff in acetone for > 2 hours.

Spray with isopropanol and blow dry. Do not let acetone dry on the chip or it will be ruined.

8. Metal-deposition for e-beam gates

Using TE-3 or TE-5 in CNS cleanroom.

8.1. Load sample into thermal evaporator

1. Open evaporator, close all pumps, then vent
2. Load Ti into crucible holder 2, Gold into crucible holder 3
3. Add backup of Ti into crucible 1
4. Attach chip to holder with double sided tape, make the tape dirty
5. Pre-pump using roughing pump, down to 2E-1Torr
6. Close roughing valve, open high vacuum valve

8.2. Metal gas-out

after about 30 mins to 1 hr

1. Degas Ion-gauge
2. when reached the low 10E-6 or ideally high 10E-7 pressures ($\leq 2 \times 10^{-6}$ Torr) switch ON Power supply
3. turn up current slowly, wait until current equilibrates (approx 10 A / 10 secs)

4. Ti: careful - will not melt until really high current and then practically explode and jump to 3 nm/s, observe boat with sun glasses TUNE down current immediately Ti melts anywhere btw. 150 and 190 Amp with 0.15" Tungsten boats
5. gas out all sources (shutter closed)
6. possibly evaporate 10 nm of Titanium again which lowers the pressure strongly

8.3 Evaporate metal

- Wait for pressure to go down again, for about 1 hour.

Deposit:

- 5 nm of Ti at 0.05 nm/s
- 15 nm of Au at 0.05 nm/s

8.4 Unload sample

- Switch off power
- CLOSE "HIGH VAC", cryopump valve
- Vent evaporator
- Take sample off carefully, use razor-blade, don't lever it up but circle around it protruding deeper underneath each time

9. Insulator-layer, via Atomic Layer Deposition (ALD)

1. Load sample into ALD in sample preparation room
   (a) close stop-valve, set flow to 100
   (b) open after at room pressure
   (c) put sample in the center
   (d) close lid, open stop valve
   (e) OPEN precursor valve
2. Set cycles
   (a) Set flow to 20
   (b) Set delay to 5 mins
   (c) Set valve 0 open time to 0.1 s
   (d) Set valve 1 open time to 0.1 s
   (e) Set pump time to 5 seconds each
   (f) Set Expose time to 0 seconds
   (g) Set number of cycles
      - Assume 0.9 nm / cycle but compare to values in logbook, do a test-run if in doubt or if thickness is critical.

Date	Substrate	Cycles	Thickness	Deposition rate	Comments
04/24/06	Si-wafer	31 ± 1 nm	342	0.091 nm / cycle	-
04/25/06	Si-testchip	39.5 nm	427	0.093 nm/cycle	-
04/29/06	Si-testchip	33.8 nm	390	0.087 nm/cycle	-

Table A.1: ALD deposition rate from past depositions.

3. Press Start
4. Wait
5. Close Stop Valve when done - set flow to 100
6. Take out sample, Close lid and set flow to 20
7. **Close precursor**

10. Metal-deposition for magnetic top layer

10.1. Load sample into TE 4

1. Open evaporator, close all pumps, then vent the system.
2. Load Permalloy, 84% Ni, 16% Fe into crucible holders 1 and 2 (backup boat)
3. Load gold into crucible holders 3 and 4 (backup boat)
4. Attach chip to holder with double sided tape, make the tape dirty to avoid breaking of chip during removal.
5. Prepump roughing pump until 2E-1Torr
6. Close roughing valve, open high vacuum valve

10.2. Metal gas-out

After pumping for about $0.5 - 1$hours, after reaching the low 10^{-6} Torr pressures

1. Switch ON Power supply
2. Turn up current slowly, wait until current equilibrates (approx 1 A / s)
3. Out-gas all sources (shutter closed!)

10.5. Evaporate Metal

Wait for pressure to go down again for about 1 hour.

- Deposit:
  - 5 nm of Titanium
- Shutter closed:
  - 10 nm of Permalloy

- Open shutter
  - 100 nm of Permalloy at < 0.1 nm/s
  - 15 nm of Gold at 0.1 nm/s as a cap against oxidation

10.6. Take out after switching off power and venting CLOSE HIGH VAC FIRST!

10.7. Take sample off carefully (use razor-blade)

11. Metal deposition on photolithography layers (non-ohmic)

(for top gate contact layer)

11.1. Load sample into TE 3

1. Open evaporator, close all pumps, then vent
2. Load Ti into crucible holder 2, Gold into crucible holder 3
3. Attach chip to holder with double sided tape, make the tape dirty
4. Prepump roughing pump until 2×10^{-1}Torr
5. Close roughing valve, open high vacuum valve

11.2. Metal gas-out

After about 30 mins, when low 10^{-6} Torr pressures are reached (around 2×10^{-6} Torr) switch on power supply.

- Turn up current slowly, wait until current equilibrates (~ 0.1 nm/s)
- Out-gas all sources (shutter closed)
- Evaporate 10 nm of Titanium again which lowers the pressure strongly

11.3. Evaporate metal

Wait for pressure to go down again, for about 1 hour. Deposit:

- 5 nm of Ti at 0.05 nm/s
- 200 nm of Au at 0.3 nm/s

(The height of the Gold-layer should be 10 nm higher than the highest mesa.)

11.4. Take out after switching off power, CLOSING HIGH VAC valve, and venting

11.5. Take sample off carefully (use razor-blade)

Appendix B

Reflectometry for fast Quantum Dot Charge-Sensing and Single-Shot Measurements

B.1 Introduction

B.1.1 Motivation

For charge measurements in quantum dots, in particular for applications in spin measurements for quantum information processing, it is desirable to detect the conductance of a charge sensor at high bandwidth and with low noise [Schoelkopf 1998]. The charge sensor in question can be a quantum point contact (QPC) [Reilly APL 2007], a single electron transistor (SET) [Schoelkopf 1998], or a sensor quantum dot (SQD) [Barthel SQD 2010], conceptually similar to a SET. Aside from high bandwidth it is also desirable to work at high frequencies because of 1/f noise from the electronics and from the sample itself, e.g. charge noise in a GaAs two dimensional electron gas.

The high resistance of the charge sensors, which are typically operated at conductances, $g < 0.5$ e^2/h, where they are most sensitive to their local electric potential [Field 1993; Barthel SQD 2010], poses a fundamental challenge obtaining high bandwidth and operation frequencies in charge detection setups. At the typical conductances, $g \sim 0.25e^2/h$, the resistance is, $R \sim 100$ kΩ, which together with the typical capacitances, $C > 100$pF, of dilution refrigerator dc wiring, sets an upper limit for the applied frequencies for sensing currents and for the bandwidths that can be obtained. The bandwidth f_{RC} for a QPC

measured at $g \sim 0.25\ \mathrm{e}^2/\mathrm{h}$ with fridge wiring capacitance $C \sim 500\mathrm{pF}$ is

$$f_{\mathrm{RC}} = \frac{1}{2\pi\, R\, C} = \frac{1}{2\,\pi\, 100\,\mathrm{k\Omega}\, 500\,\mathrm{pF}} \sim 3\ \mathrm{kHz}. \tag{B.1}$$

B.1.2 Reflectometry

Reflectometry is one of the key constituents that enabled the fast and sensitive measurements in chapters 4 - 7. As discussed in section B.1.1 it is desirable to measure electronic systems at higher frequencies to avoid $1/f$ noise, a goal that is complicated by the low RC bandwidth of high impedance devices [Eq. B.1]. The reflectometry setup used in the experiments of this thesis was only slightly modified after being implemented by David Reilly as described in Ref. [Reilly APL 2007]. RF-reflectrometry was originally developed, implemented and described in Ref. [Schoelkopf 1998].

In reflectometry the resistance of the device of interest, like a charge sensor, is measured indirectly via the damping of a resonant rf-circuit. The so called tank circuit, schematically shown in Fig. B.1(b), is an LCR circuit, and behaves as a resistance matching network when used in reflectometry measurements.

In rf- or microwave circuits electromagnetic waves are reflected at interfaces between elements that have different impedance Z. If the impedances of the source circuit, e.g. rf-generator and coaxial connections, are equal to the coupled element, the power emitted from the sources is completely absorbed by the coupled element. This is the case for a standard rf-terminator which, at 50 Ω, absorbs the power emitted from a 50 Ω transmission line, e.g. a standard coaxial cable, completely. Otherwise, part of or all of the power is reflected back into the source. The reflection coefficient, for the voltage amplitude, at an interface between a source with impedance Z_0 and a circuit element with impedance Z is

$$\Gamma = \frac{Z - Z_0}{Z + Z_0}, \tag{B.2}$$

as derived in great detail in Ref. [Pozar 1988].

The key of using a tank circuit in the measurement of high electronic devices is to match a certain set-resistance of the measured device to the source, such that $Z = Z_0$.

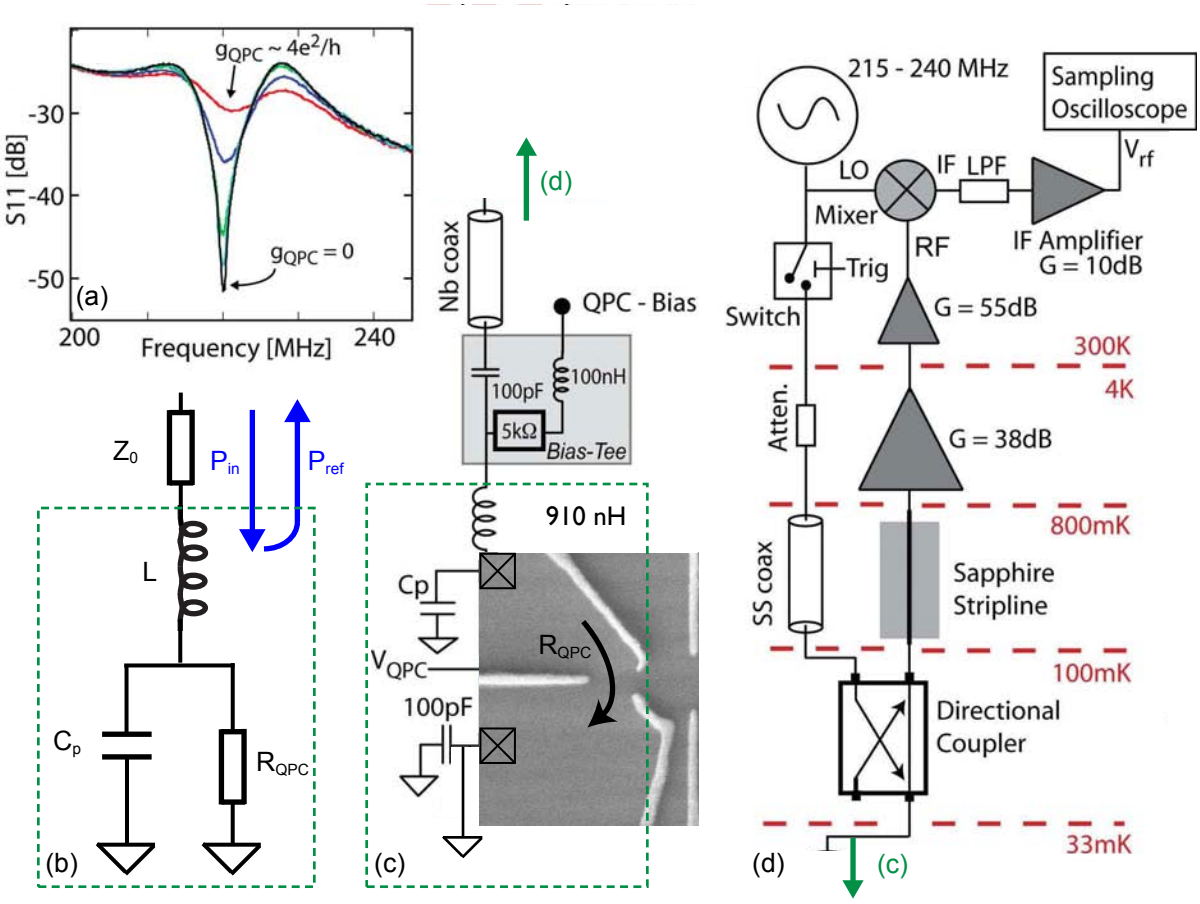

Figure B.1: Reflectometry, principle (a) Reflection coefficient, S_{11}, of a tank circuit, in a reflectometry setup with a QPC as resistive element, as function of the excitation frequency. Curves of S_{11} are shown for different QPC conductances, g_{QPC} (and hence resistances). For "infinite" QPC resistance, $g_{\mathrm{QPC}} \sim 0$ (black curve) the absorption at resonance frequency, f_{R}, is strongest, while the dip reflection coefficient gets less pronounced for smaller resistances (green and blue traces), and disappears for $g_{\mathrm{QPC}} \sim 4e^2/h$ (red trace). (b) Schematic drawing of a tank circuit with a QPC as resistive element. The reflected rf-power, P_{ref}, for constant input rf-power P_{in} depends on the resistance of the charge sensor, R_{QPC}. The inductor with inductance, L, and the capacitance, C_{p}, usually from bond pads, wires and stray-capacitance determine the resonance frequency, f_{R}, see Eq. B.3, and the matched resistance of minimum reflection. (a), (c) and (d) are adapted from Ref. [Reilly APL 2007], (b) is adapted from Ref. [Cassidy 2008].

When the device resistance changes from the set-resistance, the input impedance of the full circuit, Z [1], and therefore the reflected rf-amplitude change as well. The logarithmic

[1]The impedance Z is the input impedance, of the tank-circuit as a whole - indicated by the dashed green box in Fig. B.1(b). The input impedance is the impedance measured from the input of the tank-circuit to ground, as described in Ref. [Horowitz 1989].

power reflection coefficient, $S11 = \log(\Gamma^2)$, of a tank circuit with an attached QPC is shown in Fig. B.1(a). At a resonant frequency the reflection coefficient is highly sensitive to the device conductance.

The resonant frequency, f_{R}, is determined by the components of the tank circuit, schematically shown in Fig. B.1(b). The source, the coaxial cable connecting to the rf-generator, is indicated by the resistor at the top (rectangle) and typically, as well as in the experiments in this thesis, has the value $Z_0 = 50\ \Omega$. The tank circuit is formed by an inductor in series with a capicitance C_{p}, parallel to the ohmic resistance, R_{QPC}, of the measured device. Note that the resonant frequency

$$f_{\mathrm{R}} = \frac{1}{2\,\pi\sqrt{L\,C_{\mathrm{p}}}} \tag{B.3}$$

does not depend on the resistive element for large resistances and capacitances. At smaller resistance of the sensor and smaller capacitances, both cases are not relevant for this application, correction terms containing R_{QPC} alter the resonant frequency [Pozar 1988; Cassidy 2008]. For the matching to work, two free parameters are needed, as the imaginary part of Z needs to be zero, and the real part needs to be 50 Ω. The input impedance of matching network can be calculated, as laid out in Refs. [Horowitz 1989; Cassidy 2008], as

$$Z = i\,\omega\,L + \frac{1}{1/R_{\mathrm{QPC}} + i\,\omega\,C_{\mathrm{p}}}. \tag{B.4}$$

At the resonance frequency the imaginary part of the impedance vanishes and the input impedance of the tank circuit is

$$Z \sim \frac{L}{R_{\mathrm{QPC}}\,C_{\mathrm{p}}}. \tag{B.5}$$

The impedance [Eq. (B.5)] needs to be matched to the impedance of the source circuit, $Z_0 \sim 50\Omega$, to maximize the signal. If the input impedance for matched sensor resistance at resonance frequency is equal to the source output impedance, the whole rf-power is absorbed. Changes in R_{QPC} then lead to large changes in reflected voltage amplitude.

The capacitance, C_{P}, is not under direct experimental control as it results from stray capacitances of bond wires and inductor, and from the capacitance of the 2DEG and the

Ohmic contacts. Therefore, C_{P} will vary between nominally identical devices, and to some extent even between different cool-downs of the same device (but only by few percent). The typical value of the tank circuit capacitance for the devices in this thesis is $C_{\mathrm{P}} \sim 0.5$ pF, see Appendix C.

The matching resistance is therefore controlled via the rf-frequency and the inductance, L. The cold amplifier, see section B.2, has a finite gain bandwidth of typically ~ 40 MHz around a center frequency which was ~ 230 MHz for the amplifier used in the experiments in chapters 4-7. In general one frequency, f_{R}, that is suitable for the application [2] is chosen when designing or ordering the customized rf-amplifier.

With the frequency constrained to the amplifier gain window after design, the inductance, L, is the only parameter that can be changed for fine-tuning during device cool-down. However, most coils develop a self-capacitance at high inductances, usually quoted as self-resonant frequency. This limits the freedom in the choice of matched resistance R_{QPC}, and it is not always possible to achieve $R_{\mathrm{QPC}} \sim 100$ kΩ, as desirable for charge sensors. It is advisable to reduce the capacitance C_{p} by keeping bondwires of the sensors short and avoiding cross coupling to wires of other connections. For the experiments in chapters 4 - 7, the inductance was $L = 910$ nH. Matching was achieved for $g \sim 0.4\mathrm{e}^2/\mathrm{h}$, ideal for charge sensing.

The inductors were obtained from coilcraft [3]. Free test-kits of inductors with a wide range of inductances can be ordered from them by email.

B.2 Reflectometry Measurement Setup

The reflectometry setup used in the experiments in chapter 4 and 5 is shown in Figs. B.1(c) and B.2. Figure B.2 shows the room temperature components in more detail. The rf-

[2] For GaAs QPCs and SQDs a center frequency, $f_{\mathrm{R}} \sim 230$ MHz, of the amplifier gain window is a good choice.

[3] www.coilcraft.com

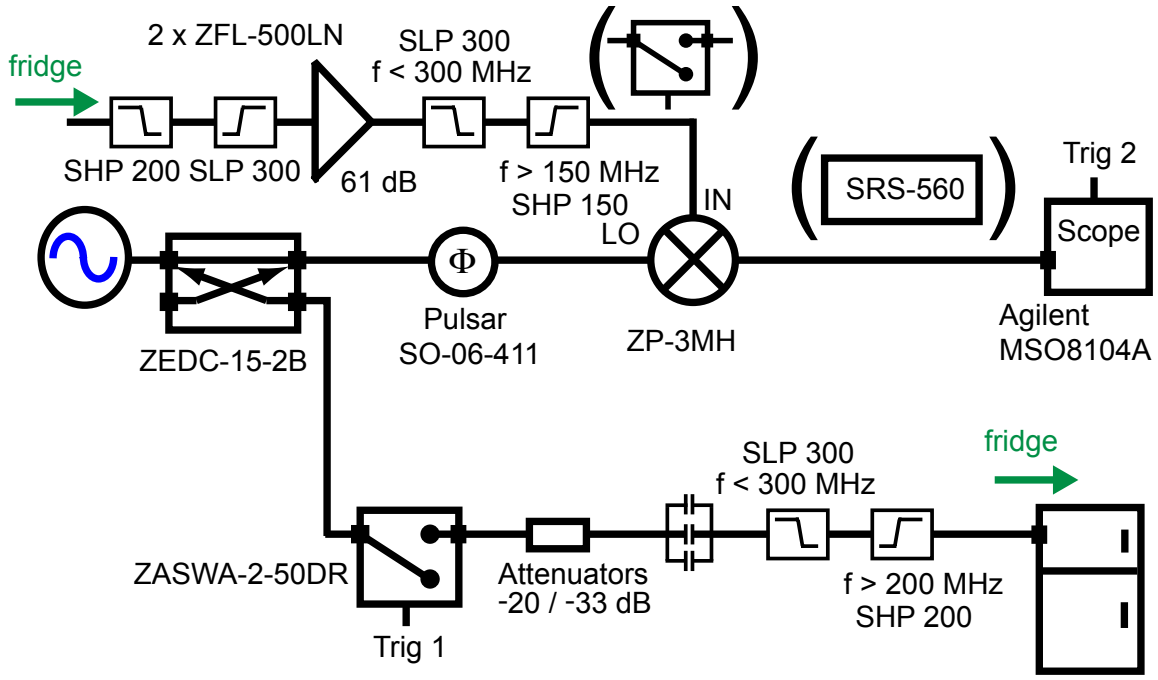

Figure B.2: RF-setup as used in the experiments described in chapters 4 - 7. Components without manufacturer name, but with part number given are supplied by minicircuits. The rf-generator is of model HP 8647A, from Hewlett Packard. The directional coupler (ZEDC-15-2B) splits the rf signal from the generator into local oscillator (~ -2 dB) and excitation (~ -15 dB) which is transmitted to the sample if the rf-switch (ZASWA-2-50DR) is switched on by a trigger from the pulse generator (Tektronix, AWG 710B or AWG5014), see Table B.1. For the experiments in chapter 4 the attenuation used was 20 dB, for the experiments in chapter 5, the attenuation was 33 dB. The signal from the refrigerator is amplified by two amplifiers (ZFL-500LN) and mixed with the local oscillator after an optional switch (ZASWA-2-50DR) by a mixer (ZP-3MH). A Stanford research SRS-560 can be used to low pass filter the signal and amplify it, as for experiments in chapter 5 (without low pass filtering option used). A fast sampling scope, Agilent Infinium MS)8104, is used for 'slow' fast-readout measurements and single-shot readout alike, and records the rf-signal. The value of a second trigger, Trig2, marking time intervals at which a the rf-amplitude contains charge signal information during single-shot measurements, is recorded as well in a second channel.

generator (Hewlett Packard, HP8647A) emits an rf-excitation up to 13 dBm. A phase shifter of model Pulsar, SO-06-411 is used to to set the optimal phase for the demodulation at the mixer. Various high- and low-pass filters as well as a dc-block decouple the dilution refrigerator wiring from the noise of the line-powered instruments. A microwave switch (ZASWA-2-5-DR) can be used to switch the rf-excitation on and off on nanosecond timescale, triggered by a marker channel of the arbitrary waveform generator.

The reflectometry is used in two main configurations, as in Refs. [Reilly APL 2007;

Reilly 2007] - in fast readout, or for single-shot measurements as in Ref. [Barthel 2009; Barthel SQD 2010].

B.2.1 Fast Readout

Due to the high bandwidth and signal-to-noise ratio of the reflectometry setup the measurement integration is no longer the bottleneck of the measurement (dc-QPC measurements typically average $\gtrsim 100$ ms per datapoint). The limitation now lies in the changing of gate voltages. For the measurement of charge stability diagrams or in order to measure ensemble averages of pulsed experiments as in Refs. [Reilly 2007; Reilly Diff. 2008; Reilly 2008], one of the double dot plunger gate voltages V_{L} or V_{R} (see chapter 2, Fig. 2.5(a)) is rapidly ramped with a sawtooth waveform at ~ 40 Hz. The ramping is achieved by simply adding the output of a Hewlett Packard HP 30250A function generator to one of the digital to analog converter (DAC) channels that provide the voltages, V_{L} and V_{R}. Triggering the oscilloscope on the marker from the function generator encodes the gate-voltage information in the time axis of the scope [Reilly APL 2007].

The gate voltage opposite of the charge sensor is ramped, in order to minimize parasitic gating of the sensor. This allows to measure a whole column in a charge stability diagram as in Fig. 2.5(d) to be measured in ~ 20 ms, rather than 10's of seconds with dc readout. The ramp rate is limited by the RC time constant of the dc gate-wiring, e.g. by the bias tee resistance. For more details about fast readout, see Ref. [Reilly APL 2007].

B.3 Single-Shot Readout

For single-shot readout operation, the rf-signal from the sample is recorded with ~ 100 ns time resolution on the scope [4], over ~ 100 ms. The rf-voltage signal from ~ 10000 experimental pulse-cycles, see chapter 2.5, is saved without loss of information, as it would be the case in conventional ensemble averaged measurements via lock-in amplifiers or in

[4] In chapter 4, the time resolution is 250 ns, in chapter 5, 50 ns. In chapter 6 the time-resolution is adapted between 100 ns and 250 ns to optimize scope memory usage when measuring short decay time constants over shorter time periods, and long decay time constants over longer time periods.

Point	$\Delta\tau$	ΔV_{R}	ΔV_{L}	Trig1	Trig2
Preparation	100	-3	1	0	0
Separation	1000	-9	9	0	0
Measure0	50	0	0	0	0
Measure1	250	0	0	1	0
Measure2	7000	0	0	1	1
Wait	150	0	0	1	0

Table B.1: Simplified sample pulse sequence. The first column contains the name of the pulse segment, the second column contains the duration of the segment in nanoseconds. The third and fourth column contain the pulse-amplitudes applied to the gatesΔ V_{R} and ΔV_{L} that control the double dot energy detuning. The fifth column contains the binary value of the first trigger Trig1 that switches on the rf-excitation to the sample, see Fig. B.2. The sixth column contains the binary value of the second trigger Trig2 that marks the time intervals during which rf-charge signal information is contained in the rf-voltage recorded by the scope, see Fig. B.2.

fast-readout operation, see section B.2.1. The loss of information in those measurements is due to integration over several experimental cycles, yielding only one averaged voltage for thousands of cycles, from which a singlet or triplet probability can be extracted.

In single-shot readout, the intervals of rf-data that correspond to spin-/charge- measurements must be identified in post-processing. In order to identify which time intervals contain a signal from a measurement time window, and in order to switch on the rf-source only during the measurement, two markers are generated by the pulse generator, and synchronized with the gate voltage pulses.

Table B.1 shows a simplified gate- and marker- voltage sequence for single-shot readout measurments. No rf-excitation is applied to the charge sensor during the preparation and separation time intervals. The separation interval is shown for a simple FID type experiment, as discussed in chapter 4. Any operation sequence, as exchange rotations or spin echo sequences can be substituted, see chapter 7. During the time interval Measure0 the gate voltage configuration is set to the measurement point, still without application of rf-excitation, to avoid enhanced relaxation during electron recombination.

The marker Trig1, see Fig. B.2, switches the rf-excitation to the sensor on, shortly after the gate voltages, V_{L} and V_{R}, are set to the measurement point, see chapter 2.5. After a wait time, long enough for the tank circuit to settle from ringing during switch-on, typically $\sim$ 200 ns, the marker channel Trig2 is switched on. The marker Trig2, see Fig. B.2,

is synchronized to the time at which the signal from the beginning of the measurement time interval arrives at the scope. The voltage output from Trig 2 is recorded in a second scope channel. A computer program written in Igor uses the scope trace with the Trig2 voltage to identify pieces of data during which an actual charge signal from the sensor is arriving at the scope.

The delay between Trig1 and Trig2 is set such that Trig2 fires just as the rf-signal from a well determined delay after the beginning of Measure0 arrives at the scope. This synchronization is achieved on the one hand by the delay in the pulse sequence, shown in table B.3, on the other hand the delay is fine-tuned by the delay of the scope channels that record charge sensor signal and marker Trig2 respectively. The scope delay is tuned by creating a voltage spike on one of the plunger gates. The scope delay is then set such that the voltage spike occurs at time zero on the scope. A time delay in the pulse sequence of the AWG, then corresponds to the actual time delay between beginning of time spent at the measurement point and the time at which Trig2 marks the voltage signal as charge signal.

The delay between the signal from the beginning of Measure0 arriving at the scope and the beginning of the marker Trig2 is set to ~ 300 ns in the experiments described in chapters 4 - 7.

Appendix C

Signal and Noise in RF-Reflectrometry Measurements

C.1 Introduction

In chapters 4 and 5 fast rf measurement of the charge and spin state of a double quantum is discussed. In this appendix, the signal, $v_{\rm rf}$, and the RMS voltage noise, $\sigma_{\rm rf}$, are calculated for the sensor quantum dot (SQD), discussed in chapter 5, and for the QPC, discussed in chapters 4 and 5, using the experimental parameters. This analysis closely follows Ref. [Korotkov 1999].

C.2 Common Parameters

Both SQD and QPC are operated at rf frequency, $f \sim 220$ MHz, which is the resonance of the rf tank circuit, see Appendix B. With the inductance of the tank circuit coil, $L = 910$ nH, and the relation for the tank circuit resonance frequency

$$f = \frac{1}{2\pi\sqrt{LC}}, \tag{C.1}$$

we can determine, $C \sim 0.56$ pF. The capacitance is created by ohmic contacts 2DEG, bond wires and pads and can hence not directly measured but may be different for each device and even cooldown. For QPC and SQD in the experiments described in chapters 4 and 5 the resonance frequencies and therefore the capacitances were approximately equal.

Attenuation between rf generator and tank circuit

The applied power can be calculated from the output of the rf generator and the attenuations between generator and tank circuit:

- directional couper: 15 dB
- rf switch: 2dB
- attenuators at room temperature:
  - SQD: 33 dB
  - QPC: 20 dB
- attenuation in dilution refrigerator: 57 dB

The total attenuation between rf generator and tank circuit is:

- SQD: 107 dB
- QPC: 94 dB

C.3 SQD Signal and Noise

Applied power is estimated from 7.8 dBm output at RF-generator, -107 dB attenuation. The applied power to the SQD is -99 dBm, therefore $P = 1.3 \times 10^{-13}$W. The current amplitude through the dot sensor is therefore, with a SQD resistance $R \sim 125$ kΩat $g \sim 0.2\ e^2/\mathrm{h}$,

$$I = \sqrt{2} \times \sqrt{P/R} = \sqrt{2} \times \sqrt{1.3 \times 10^{-13}\mathrm{VA}/(1.25 \times 10^{5}\mathrm{V/A})} = 1.4 \text{ nA}. \tag{C.2}$$

C.3.1 SQD Signal

The conductance swings over a range of up to 70% around $g \sim 0.2\ e^2/\mathrm{h}$, $95 \ldots 180$kΩ, so the current will vary by$\Delta\ I \sim 0.45$ nA. According to Korotkov we can calculate the rf signal as

$$X = 2\sqrt{L/C}\langle I(t) \sin \omega t \rangle = \sqrt{L/C} \times I, \tag{C.3}$$

as $I(t) \propto \sin(\omega t)$. The pre-mixer signal ,$\Delta\ V'$, will be related to the tank circuit signal $\Delta X = \sqrt{L/C} \times \Delta I$ as

$$\Delta V' = G_A \times \Delta X = G_A \times \sqrt{L/C} \times \Delta I, \tag{C.4}$$

with the Amplifier gain, $G_A = 102$ dB, from 45 dB cold amplifier, -1dB from directional coupler in fridge, and 61 dB from room temperature amplifier, as well as -3 dB loss from a 3dB-splitter. The pre mixer signal calculates to

$$\Delta V' = 10^{102/20} \times \sqrt{910\ \text{nH}/0.56\ \text{pF}} \times 0.45\text{nA} = 72\text{mV}, \tag{C.5}$$

This voltage is before the mixer and the signal,$\Delta\ V$, actually measured on the scope is

$$\Delta V = G_M \times \Delta V', \tag{C.6}$$

The gain of ZP-3MH mixer is -5 dB, for 10 dBm of applied local oscillator power, while we are applying 5 dBm of local oscillator power. Measuring the conversion loss for the actual conditions yields, $G_M \sim -6$ dB. Thus

$$\Delta V = 36mV, \tag{C.7}$$

which is in good quantitative agreement with the measured signal,$\Delta\ V_{\text{SQD}} \sim 33mV$, see chapter 5.

C.3.2 Noise Sources in SQD Measurement

Shot-Noise

Assuming shot noise with Fano factor 1/2, as the tunnel barriers are about equal, and using the current, $I = 1.4$ nA from Eq. (C.2) we get

$$S^{\text{I}}_{\text{SQD}} = 2, (1/2)\, e\, I = 2 \times (1/2) \times 1.602 \times 10^{-19}\text{As} \times 1.42 \times 10^{-9}\text{A} = \tag{C.8}$$

$$2.3 \times 10^{-28}\text{A}^2/\text{Hz} \tag{C.9}$$

We convert this current noise power into into a voltage noise power with Eq. (3) from Ref. [Korotkov 1999],

$$S_{\mathrm{SQD}} = 4L/C\langle S^{\mathrm{I}}_{\mathrm{SQD}}(t)\sin^2\omega t\rangle. \tag{C.10}$$

The time dependence in $S^I_{SQD}(t)$ comes from the time dependence of $I(t)$, the time average is solved below in section C.5. Taking the time-average, $\langle S^I_{SQD}(t)\sin^2\omega t\rangle = 0.42$, yields the voltage noise power

$$S_{\mathrm{SQD}} = 4L/C \times S^I_{\mathrm{SQD}} \times 0.42 = 4 \times 910\mathrm{nH}/0.56\mathrm{pF} \times 2.3 \times 10^{-28}\mathrm{A}^2/\mathrm{Hz} \times 0.42 = \tag{C.11}$$

$$6.2 \times 10^{-22}\mathrm{V}^2/\mathrm{Hz}. \tag{C.12}$$

This noise at the sensor is amplified by a gain of 102 dB, by cold amplifier (45 dB), directional coupler (-1dB) and warm amplifier (61 dB), and 3dB splitter (-3dB). Ignoring losses in the coaxes we get a noise power at room temperature

$$S_{\mathrm{RT}} = S_{\mathrm{SQD}} \times G = 6.2 \times 10^{-22}\mathrm{V}^2/\mathrm{Hz} \times 10^{10.2} = 1 \times 10^{-11}\mathrm{V}^2/\mathrm{Hz}. \tag{C.13}$$

As with the signal, the noise will be attenuated by the mixer gain, $G_M = -6$ dB.

$$S_{\mathrm{scope}} = 1/4\, S_{\mathrm{RT}} \tag{C.14}$$

This yields with a bandwidth, of 1.5 MHz, limited to 1 MHz due to the 1 μs integration time associated with σ_0, the 1 μs-RMS voltage noise

$$\sigma_0 = V_{\mathrm{RMS}} = \sqrt{S_{\mathrm{scope}} \times \mathrm{BW}} = \sqrt{1/4 \times 10^{-11}\mathrm{V}^2/\mathrm{Hz} \times 1\mathrm{MHz}} = 1.5\ \mathrm{mV}. \tag{C.15}$$

With the measured RMS voltage width, $\sigma_0 = 5$ mV, this indicates that $\sim 10\%$ of the noise is due to shot-noise[1], while about 90% is due to other noise sources like the cold amplifier.

[1]Contributions to the RMS voltage noise add in quadrature, as the noise powers, not voltages add.

Amplifier noise

The noise of the cold amplifier can be calculated from the quoted amplifier noise temperature of 2.7 K. The cold amplifier alone would yield a RMS voltage noise

$$V_{RMS} = \sigma_0 = \sqrt{4 \times k_B \times 2.7\text{K} \times 50\Omega \times 10^{102/10} \times 0.5\,\text{MHz}} \times 10^{-6/20} = 3.9\ \text{mV}. \quad \text{(C.16)}$$

Note that, because of the one-sided power spectral density in its definition, for the Johnson-Nyquist formula the relation$\Delta\ f = 1/(2\tau)$ with integration time, τ, is used. The Amplifier-noise is therefore responsible for $\sim 60\%$ of the total noise.

Johnson-Nyquist noise, thermal fluctuations

Analog to shot-noise and amplifier noise we can calculate the Johnson-Nyquist noise due to thermal fluctuations in the SQD

$$S^I_{\text{Th}} = 4 \times k_B \times 125\text{mK}/(125\text{k} \times \Omega) = 5.5 \times 10^{-29}\text{A}^2/\text{Hz}, \quad \text{(C.17)}$$

which is 1/4 of the shot-noise power spectral density. Remembering that the factor of two difference in power spectrum definition (Johnson noise has a one-sided power spectral density, while shot-noise is two-sided.), makes the contribution from thermal fluctuations 1/8 of the shot-noise contribution or $\sim 1\%$ of the total noise.

C.4 QPC1 Signal and Noise

The applied power is estimated from 5.4 dBm output at RF-generator, - 15 dB directional coupler, -2 dB rf-switch, -20 dB RT attenuator, -57 attenuation in dilution refrigerator. The applied power to QPC1 is -88.6 dBm, therefore $P = 1.4^{-12}$W. The current through QPC1, with a QPC resistance $R \sim 65$ kΩat $\ g \sim 0.4\ e^2/\text{h}$, is

$$I_0 = \sqrt{2} \times \sqrt{P/R} = \sqrt{2} \times \sqrt{1.4 \times 10^{-12}\text{VA}/(6.5 \times 10^4\text{V/A})} = 6.5\ \text{nA}. \quad \text{(C.18)}$$

C.4.1 QPC1 Signal

The conductance swings over a range of up to 5% around $g \sim 0.4\ e^2/\mathrm{h}$, therefore the current will vary by$\Delta\ I \sim 6.5/40 \sim 0.16$ nA. According to Ref. [Korotkov 1999] and analogous to section C.3.2, we can calculate the rf signal as

$$X = 2\sqrt{L/C}\langle I(t)\sin\omega t\rangle = \sqrt{L/C} \times I, \tag{C.19}$$

since $I(t) \propto \sin(\omega t)$. The pre-mixer signal ,$\Delta\ V'$, will be related to the tank circuit signal $\Delta X = \sqrt{L/C} \times \Delta I$ as

$$\Delta V' = G_A \times \Delta X = G_A \times \sqrt{L/C} \times \Delta I, \tag{C.20}$$

with the Amplifier gain, $G_A = 100$ dB, from 45 dB cold amplifier, -1 dB from directional coupler in refrigerator, 61 dB from room temperature amplifier, -2 dB from an rf-switch before the mixer, and -3 dB from 3dB splitter. The pre-mixer signal calculates to

$$\Delta V' = 10^{100/20} \times \sqrt{910\ \mathrm{nH}/0.56\ \mathrm{pF}} \times 0.16\mathrm{nA} = 20\mathrm{mV}, \tag{C.21}$$

This voltage is before the mixer and the signal,$\Delta\ V$, actually measured on the scope is

$$\Delta V = G_M \times \Delta V', \tag{C.22}$$

The gain of ZP-3MH mixer is -5 dB, for 10 dBm of local oscillator power, while we are applying 3 dBm of local oscillator power. Measuring the conversion loss for the actual conditions yields, $G_M \sim -7.5$ dB. Thus

$$\Delta V = 8.6mV, \tag{C.23}$$

which is in reasonable agreement with the measured signal,$\Delta\ V_{\mathrm{QPC1}} \sim 9.5mV$, see chapters 4 and 5.

C.4.2 Noise Sources in QPC1 Measurement

QPC Shot-noise

Assuming shot noise with Fano factor 1 and current $I = 6.5$ nA from Eq. (C.18), we get the current noise power:

$$S^I_{\mathrm{QPC}} = 2(1)eI_0 = 2 \times 1.602 \times 10^{-19}\mathrm{As} \times 6.5 \times 10^{-9}\mathrm{A} = 2.1 \times 10^{-27}\mathrm{A}^2/\mathrm{Hz}, \quad \text{(C.24)}$$

which we convert into a voltage noise power with Formula (3) from Ref. [Korotkov 1999]

$$S_{\mathrm{QPC}} = 4L/C\langle S^I_{\mathrm{QPC}}(t)\sin^2\omega t\rangle. \quad \text{(C.25)}$$

The time dependence in $S^I_{QPC}(t)$ comes from the time dependence of $I(t)$, the time average is solved below in section C.5. Solution of the integral, $\langle S^I_{SQD}(t)\sin^2\omega t\rangle = 0.42$, yields the voltage noise power

$$S_{\mathrm{QPC}} = 4L/C \times S^I_{\mathrm{QPC}} \times 0.42 = 4 \times 910\mathrm{nH}/0.56\mathrm{pF} \times 2.1 \times 10^{-27}\mathrm{A}^2/\mathrm{Hz} \times 0.42 = \quad \text{(C.26)}$$

$$5.7 \times 10^{-21}\mathrm{V}^2/\mathrm{Hz}. \quad \text{(C.27)}$$

This noise at the tank-circuit is amplified by a gain of 100 dB, by cold amplifier (45 dB), directional coupler (-1dB), warm amplifier (61 dB), rf-switch (-2dB, Zaswa-2-50DR), and 3 dB splitter (-3dB), ignoring losses in the coaxes that gives a noise power at room temperature

$$S_{\mathrm{RT}} = S_{\mathrm{QPC}} \times G = 5.7 \times 10^{-21}\mathrm{V}^2/\mathrm{Hz} \times 10^{10} = 5.7 \times 10^{-11}\mathrm{V}^2/\mathrm{Hz} \quad \text{(C.28)}$$

As for the signal the noise will be attenuated by the mixer gain, $G_M = -7.5$ dB.

$$S_{\mathrm{scope}} = 10^{-7.5/10} \times S_{\mathrm{RT}} \quad \text{(C.29)}$$

This yields, for the integration time of $1\mu s$, hence the bandwidth of 1 MHz, the 1 μs-RMS

voltage noise

$$\sigma_0 = V_{\mathrm{RMS}} = \sqrt{S_{\mathrm{scope}} \times BW} = \sqrt{1 \times 10^{-11}\ \mathrm{V^2/Hz} \times 1\mathrm{MHz}} = 3.2\ \mathrm{mV} \tag{C.30}$$

With the measured noise induced width, $\sigma_0 = 4.5$ mV this indicates that $\sim 50\%$ of the noise is due to shot-noise, while about 50% is due other sources like the cold amplifier.

Amplifier noise

With the amplifier's noise temperature of 2.7 K, the cold amplifier alone would yield

$$V_{\mathrm{RMS}} = \sigma_0 = \sqrt{4 \times k_B \times 2.7\mathrm{K} \times 50\Omega \times 10^{100/10} \times 0.5\mathrm{MHz}} \times 10^{-7.5/20} = 2.6\ \mathrm{mV} \tag{C.31}$$

This means about 40% of the RMS voltage width is due to the noise of the cold amplifier. For the Johnson-Nyquist formula one uses$\Delta\ f = 1/(2\tau)$, because of the one-sided power spectral density in the definition.

Johnson-Nyquist noise, thermal fluctuations

Analog to shot-noise and amplifier noise we can calculate the Johnson-Nyquist noise due to thermal fluctuations

$$S^I_{\mathrm{Th}} = 4 \times k_B \times 125\mathrm{mK}/(65\mathrm{k}\Omega) = 1.1 \times 10^{-28}\mathrm{A}^2/\mathrm{Hz}, \tag{C.32}$$

which is 1/20 of the shot-noise power spectral density. Remembering that the factor of two difference in power spectrum definition (Johnson noise is defined with a one-sided power spectral density (PSD), while shot-noise is two-sided.), makes the contribution from thermal fluctuations 1/40 of the shot-noise contribution, or $\sim 1\%$ of the total noise.

C.5 Time Average of Shot-Noise, Integral Solution

In the definition of Korotkov $S^I_{QPC}(t) \propto \sin(\omega t)$ as so is $V_b(t)$, the bias across the dot, which I assume acts ohmic, therefore $I(t)$ should have the same phase as $V_b(t)$, hence $S^I_{QPC}(t) = 2(1)eI_0|\sin(\omega t)|$ with which we get

$$S^V = 4L/CS^I\langle|\sin(\omega t)|\sin^2\omega t\rangle = \tag{C.33}$$

$$4L/CS^I \times \int_0^{2\pi} \frac{1}{2\pi} d\theta |\sin(\theta)| \sin^2\theta = \tag{C.34}$$

$$4L/CS^I \times 0.42, \tag{C.35}$$

as the integral can be solved as

$$\int_0^{2\pi} \frac{1}{2\pi} d\theta |\sin(\theta)| \sin^2\theta = 2 \times \int_0^{\pi} \frac{1}{2\pi} d\theta \sin^3\theta = 2 \times \frac{1}{2\pi}\frac{16}{12} \sim 0.42. \tag{C.36}$$

Appendix D

Rapid Single-Shot Measurement of a Singlet-Triplet Qubit: Supplementary Material

C. Barthel[1] D. J. Reilly[1,2] C. M. Marcus[1] M. P. Hanson[3] A. C. Gossard[3]

[1]Department of Physics, Harvard University, 17 Oxford Street, Cambridge, Massachusetts 02138, USA

[2]School of Physics, University of Sydney, Sydney, 2006, Australia

[3]Materials Department, University of California, Santa Barbara, California 93106, USA

This supplementary note presents a derivation of an equation that appears in the main text of the Letter "Rapid Single-Shot Measurement of a Singlet-Triplet Qubit" for the ensemble-averaged triplet T_+ return probability, P_T. The equation is used to fit experimental data in Fig. 4(b) of that Letter. The analysis assumes classical Overhauser fields that are static on the time scale of electron spin evolution but fluctuate randomly on longer time scales, where ensemble statistics are measured.

In one of the experiments described in the accompanying Letter, "Rapid Single-Shot Measurement of a Singlet-Triplet Qubit", two electrons in a double quantum dot are initialized in the singlet state, then brought to the anticrossing of the lower branch of the hybridized singlet, S, and the $m = +1$ triplet, $T_+ = |\uparrow\uparrow\rangle$. The hyperfine interaction felt by the electrons due to the large number ($\sim 10^6$) of nuclei in the host material is treated as an effective classical Zeeman (Overhauser) field acting on the electrons. The Overhauser field is further assumed to be static on time scales of the electron dynamics. Near the $S - T_+$ resonance, the difference in transverse components of the Overhauser fields in the left (L) and right (R) dots,$\Delta\ B_{\mathrm{x(y)}} = [B^L_{\mathrm{x(y)}} - B^R_{\mathrm{x(y)}}]/2$ mix singlet and triplet state, while the average longitudinal Overhauser field, $B_{\mathrm{z}} = [B^L_{\mathrm{z}} + B^R_{\mathrm{z}}]/2$, acts as a random energy detuning. An external magnetic field, B, defines the quantization axis z. This supplementary note presents a derivation of the triplet probability, P_T, used to fit experimental data in Fig. 4(b), following Ref. [Taylor Thesis 2007]. The Hamiltonian in the basis (S, T_+) is [Coish 2005; Taylor PRB 2007]

$$H = g^*\mu_B \begin{pmatrix} -J/(g^*\mu_B) & \cos\theta\, B_+/\sqrt{2} \\ \cos\theta\, B_-/\sqrt{2} & B + B_{\mathrm{z}} \end{pmatrix}, \tag{D.1}$$

where $\cos\theta$ is the (1,1) component of the hybridized singlet ground state, $|S\rangle = \cos\theta\,|(1,1)S\rangle + \sin\theta\,|(0,2)S\rangle$ and $B_\pm = \Delta B_{\mathrm{x}} \pm i\Delta B_{\mathrm{y}}$. The effective electron g-factor is $g^* = -0.44$. An additional factor $\sqrt{2}$ in the numerator of the off-diagonal term stems from constructive interference of two electron spin flip - pathways, since there are two electrons participating [Coish 2005]. The exchange, J, the external magnetic field, B, and the nuclear Overhauser z-component, B_{z}, are combined to the energy mismatch $\delta = -g^*\mu_B(B + B_{\mathrm{z}}) - J$. In the described experiment the exchange is tuned to resonance, leaving $\delta = -g^*\mu_B B_{\mathrm{z}}$. For an initial singlet $c_T(\tau_{\mathrm{I}} = 0) = 0$ the solution for the probability amplitude, $c_T(\tau_{\mathrm{I}})$, is [CohenTanuoudji 1999]

$$c_T(\tau_{\mathrm{I}}) = \frac{\cos\theta(\Delta B_{\mathrm{x}} + i\Delta B_{\mathrm{y}})}{\sqrt{2}\,\hbar\omega/|g^*\mu_B|}\sin(\omega\tau_{\mathrm{I}}), \tag{D.2}$$

with the precession frequency, ω,

$$\omega = \frac{1}{2\hbar}\sqrt{\delta^2 + 2\cos^2\theta\,(g^*\mu_B)^2(\Delta B_{\rm x}^2 + \Delta B_{\rm y}^2)} = \frac{|g^*\mu_B|}{2\hbar}\sqrt{B_{\rm z}^2 + 2\cos^2\theta\,(\Delta B_{\rm x}^2 + \Delta B_{\rm y}^2)}. \quad \text{(D.3)}$$

The nuclear Overhauser field z-component, $B_{\rm z}$, and the gradient fields,$\Delta\ B_{\rm x}$ and$\Delta\ B_{\rm y}$, are not known and constant, but distributed [Coish 2005; Taylor PRB 2007] according to the distribution function $\rho(\mathbf{B}) = (2\pi B^{\rm nuc})^{-3/2} e^{-(\mathbf{B}/(B^{\rm nuc}))^2/2}$, with $\mathbf{B} = (\ \Delta B_{\rm x}, \Delta B_{\rm y}, B_{\rm z})$. The evolution of the nuclear fields is slower than the evolution of the electron spin, hence the triplet probability for an ensemble of measurements, $P_T^{\rm ideal}(\tau_{\rm I})$, can be written as the integral of all probabilities for a single constant Overhauser field, weighted by $\rho(\mathbf{B})$,

$$P_T^{\rm ideal}(\tau_{\rm I}) = \int d^3\mathbf{B}\,\rho(\mathbf{B}) c_T(\tau_{\rm I}) c_T^*(\tau_{\rm I}) = \int d^3\mathbf{B}\,\rho(\mathbf{B}) \frac{\cos^2\theta\,(\Delta B_{\rm x}^2 + \Delta B_{\rm y}^2)}{2\,(\hbar\omega/|g^*\mu_B|)^2} \sin^2(\omega\tau_{\rm I}). \quad \text{(D.4)}$$

The evolution occurs far detuned from the (1,1)-(0,2) charge degeneracy, therefore the hybridized singlet is approximately identical to the (1,1) singlet, and $\cos\theta \sim 1$. Furthermore allowing an offset, P_T^0, of P_T, because of imperfect preparation or miscounting of singlets as triplets and a smaller than one visiblity, V, yields the equation in the paper:

$$P_T = P_T^0 + V \int d^3\mathbf{B}\,\rho(\mathbf{B}) \frac{(\Delta B_{\rm x}^2 + \Delta B_{\rm y})^2}{2\,(\hbar\omega/|g^*\mu_B|)^2} \sin^2(\omega\tau_{\rm I}), \quad \text{(D.5)}$$

which describes the measured triplet probability, averaged over many singleshot measurements.

Appendix E

Dephasing due to Imperfect Gate Voltage Pulses: Supplementary Material to Chapter 7

C. Barthel[1] J. M. Medford[1] C. M. Marcus[1] [1]Department of Physics, Harvard University, 17 Oxford Street, Cambridge, Massachusetts 02138, USA

This supplementary note presents a discussion of the influence of pulse-imperfections on the envelope function of spin echo recovery amplitudes. For a constant gate-voltage difference between the dephasing and rephasing step, before and after the π-pulse, inhomogenous broadening results in a Gaussian envelope function of the echo amplitude with a microsecond time-scale. For a linear voltage droop over the whole time spent at the electron separation point S, an envelope function of the form $e^{-(\tau/T^*_{2,\mathrm{eff}})^4}$ is found. The analysis assumes classical Overhauser fields that are static on the time scale of electron spin evolution but fluctuate randomly on longer time scales, where ensemble statistics are measured. The inhomogenous width $T^*_{2,\mathrm{eff}}$ would be fitted as and interpreted with an T_2.

In one of the experiments described in chapter 7 of this thesis two electrons in a double quantum dot are initialized in the separated singlet state, $(1,1)S$. After a time $\tau_{\rm D}/2$ a Hahn spin echo is performed and the singlet probability is measured after an additional time $\tau_{\rm D}/2$, spent at point S. The hyperfine interaction felt by the electrons due to the large number ($\sim 10^6$) of nuclei in the host material is treated as an effective classical Zeeman (Overhauser) field acting on the electrons. The Overhauser field is further assumed to be static on time scales of the electron dynamics. The longitudinal Overhauser field difference, $\Delta B_{\rm z} = [B_{\rm z}^L - B_{\rm z}^R]$, acts as a random dephasing. An external magnetic field, B, defines the quantization axis z.

E.1 Free Induction Decay

First we investigate the effect of a gate voltage drift during two-electron separation on the free induction decay measurement that yields the inhomogeneous dephasing time T_2^*, see Ref. [Petta 2005]. Following Ref. [Taylor PRB 2007; Merkulov 2002] we can write down the singlet return probability for a FID pulse in a constant field difference:

$$P_S = \cos^2\left(\Delta B_{\rm z}\gamma_{\rm e}/2\tau_{\rm S}\right) = \frac{1}{2}(1+\cos\left(\Delta B_{\rm z}\gamma_{\rm e}\tau_{\rm S}\right)), \tag{E.1}$$

where $\tau_{\rm S}$ is the time the singlet spends separated in two dots. We can generalize this for a field gradient that is not constant during the separation time:

$$P_S = \cos^2\left(\gamma_{\rm e}/2\int_0^{\tau_{\rm S}}\Delta B_{\rm z}(t)dt\right), \tag{E.2}$$

with a time-dependent$\Delta\ B_{\rm z}(t)$, due to a shift of the electron wavefunction over time induced by a voltage-drift or -droop$\Delta\ V(t)$ of the double dot gate voltage detuning. Then the singlet measurement probability becomes

$$P_S = \cos^2\left(\gamma_{\rm e}/2\int_0^{\tau_{\rm S}}\Delta B_{\rm z}^0 + \frac{d(\Delta B_{\rm z})}{d(\Delta V)}\Delta V(t)dt\right), \tag{E.3}$$

with the change in gradient due to gate voltage change $\frac{d(\Delta B_z)}{d(\Delta V)}$. Assuming in first order, that the nuclear field gradient is linear, and that the voltage droop is linear, we get

$$P_S = \cos^2(\gamma_e/2\,[\,\Delta B_z^0 + \frac{d(\Delta B_z)}{d(\Delta V)}\dot{\Delta V}\tau_S]\tau_S). \tag{E.4}$$

Due to the assumption of a linear gradient, and linear voltage droop we can simplify

$$\frac{d(\Delta B_z)}{d(\Delta V)} = \frac{\Delta B_z^0}{a_S}\frac{da}{d\Delta V}, \tag{E.5}$$

with the two-electron separation, a_S at the beginning of the separation, and the change of separation $\frac{da}{d\Delta V}$ with gate voltage, assumed to be constant. This allows us to simplify Eq. (E.4) to

$$P_S = \cos^2(\gamma_e/2\,[1 + \frac{da}{d\Delta V}\frac{\dot{\Delta V}}{a_S}\tau_S]\Delta B_z^0\tau_S). \tag{E.6}$$

which is identical to the regular free precession amplitude, aside from a small correction $\frac{da}{d\Delta V}\frac{\dot{\Delta V}}{a_S}$. The inhomogenous broadening is dominated by the$\Delta\ B_z^0\tau_S$ term.

E.2 Hahn Echo

For a Hahn echo, the evolution of the qubit is inverted after half of the total dephasing time, τ_D, spent at the separation point. The singlet measurement probability for perfect pulses and static nuclear field becomes:

$$P_S = \cos^2(\Delta B_z\gamma_e/2[\tau_D/2 - \tau_D/2]), \tag{E.7}$$

which is unity for arbitrary τ_D. The minus sign between the two times $\tau_D/2$ is due to the inversion of the evolution by the π-pulse.

E.2.1 Constant Offset between Gate Voltage Pulses

For a constant difference in gate voltage,$\Delta\ V$, between the dephasing time window before and the rephasing time window after the π-pulse we can modify the expression for an ideal

Hahn echo (E.7),

$$P_S = \cos^2\left(\gamma_{\rm e}/2\left[\,\Delta B_{\rm z}\tau_{\rm D}/2 - \left(\Delta B_{\rm z} + \delta\Delta B_{\rm z}\right)\tau_{\rm D}/2\right]\right), \tag{E.8}$$

with the discrepancy in field difference, $\delta\Delta B_{\rm z}$, before and after the echo pulse. Due to the field discrepancy only part of the dephasing will be refocussed,

$$P_S = \cos^2\left(\gamma_{\rm e}/2\left[-\delta\Delta B_{\rm z}\tau_{\rm D}/2\right]\right) = \cos^2\left(\gamma_{\rm e}\delta\Delta B_{\rm z}\tau_{\rm D}/4\right). \tag{E.9}$$

The field discrepancy can be estimated from the relative shift in electron wave function due to the voltage discrepancy.

$$\delta\Delta B_{\rm z} = \Delta B_{\rm z}\frac{\delta a_{\rm S}}{a_{\rm S}}, \tag{E.10}$$

with $a_{\rm S}$, the typical distance of the two electrons when separated into two dots, at point S, and $\delta a_{\rm S}$, the difference in distance between the time interval before and after the π-pulse. The electron wavefunction shift can be estimated from discrepancy, $\delta\Delta V$, in gate voltage, ΔV, before and after the π-pulse,

$$\frac{\delta a_{\rm S}}{a_{\rm S}} = \Delta B_{\rm z}\frac{da_{\rm S}}{d\Delta V}\frac{1}{a_{\rm S}}\delta\Delta V. \tag{E.11}$$

Using the relation from Ref. [Taylor PRB 2007],

$$\left\langle\cos^2\left(\omega\,\tau\right)\right\rangle = \frac{1}{2}\left(1 + e^{-(t/T_2^*)^2}\right), \tag{E.12}$$

we get:

$$P_S = \frac{1}{2}\left(1 + e^{-(t/T_{2,\rm eff}^*)^2}\right), \tag{E.13}$$

with the effective T_2^*,

$$T_{2,\rm eff}^* = 2\,T_2^*\frac{a_{\rm S}}{\delta a_{\rm S}}, \tag{E.14}$$

$T^*_{2,\mathrm{eff}}$	$\delta a_\mathrm{S}/a_\mathrm{S}$	$\delta\Delta V$ for$\Delta\ V = 15$ mV
1 μs	$\sim 3\%$	0.5 mV
5 μs	$\sim 0.6\%$	0.2 mV
10 μs	$\sim 0.3\%$	0.1 mV
30 μs	$\sim 0.1\%$	0.03 mV
100 μs	$\sim 0.03\%$	0.01 mV

Table E.1: Maximum relative changes in electron-wavefunction position, $\delta a_\mathrm{S}/a_\mathrm{S}$, and corresponding maximum gate-voltage changes between dephasing and refocussing time of a Hahn spin echo sequence, in order to achieve the inhomogenous coherence time ,$T^*_{2,\mathrm{eff}}$, given in the first column.

where

$$T^*_{2,\mathrm{eff}} = 2\,T^*_2\,\frac{a_\mathrm{S}}{\delta a_\mathrm{S}}, \tag{E.15}$$

With Eq. E.11, and assuming linear shift of position with voltage, we can estimate the imperfections that would give a certain $T^*_{2,\mathrm{eff}}$. Table E.2.1 shows the accuracies in relative separation distance,$\frac{\delta a_\mathrm{S}}{a_\mathrm{S}}$, needed in order to achieve a certain $T^*_{2,\mathrm{eff}}$. Gaussian envelope functions for ensemble averaged echo recovery amplitudes with time constants, $T^*_{2,\mathrm{eff}}$, in agreement with measured T_2 times result from very small gate-voltage deviations between dephasing and refocussing stage of a Hahn spin echo sequence.

E.2.2 Linear Decay of Gate Voltage Pulse Amplitude

Generalizing as for the free induction decay we get:

$$P_S = \cos^2\left(\gamma_\mathrm{e}/2\left[\int_0^{\tau_\mathrm{D}/2}\Delta B_\mathrm{z}(t)dt - \int_{\tau_\mathrm{D}/2}^{\tau_\mathrm{D}}\Delta B_\mathrm{z}(t)dt\right]\right), \tag{E.16}$$

$$P_S = \cos^2\left(\gamma_\mathrm{e}/2\left[\left(1+\frac{da}{d\Delta V}\frac{\dot{\Delta V}}{a_\mathrm{S}}\tau_\mathrm{D}/2\right)\Delta B^0_\mathrm{z}\tau_\mathrm{D}/2 - \left(1+3\frac{da}{d\Delta V}\frac{\dot{\Delta V}}{a_\mathrm{S}}\tau_\mathrm{D}/2\right)\Delta B^0_\mathrm{z}\tau_\mathrm{D}/2\right]\right), \tag{E.17}$$

which can be simplified to

$$P_S = \cos^2\left(\gamma_\mathrm{e}/2\left[\frac{da}{d\Delta V}\frac{\dot{\Delta V}}{a_\mathrm{S}}\tau_\mathrm{D}\right]\Delta B^0_\mathrm{z}\tau_\mathrm{D}/2\right), \tag{E.18}$$

as the linear terms cancel out. Simplification yields:

$$P_S = \cos^2\left(\gamma_e/4\left[\frac{da}{d\Delta V}\frac{\dot{\Delta V}}{a_S}\right]\Delta B_z^0 \tau_D^2\right), \tag{E.19}$$

Using the relation from Ref. [Taylor PRB 2007],

$$\langle \cos^2(\omega\,\tau)\rangle = \frac{1}{2}\left(1 + e^{-(t/T_2^*)^2}\right), \tag{E.20}$$

we get:

$$P_S = \frac{1}{2}\left(1 + e^{-(t/T_{2,\mathrm{eff}}^*)^4}\right), \tag{E.21}$$

with an effective T_2^*,

$$(T_{2,\mathrm{eff}}^*)^2 = 2\,T_2^*\left[\frac{da}{d\Delta V}\frac{\dot{\Delta V}}{a_S}\right]^{-1}. \tag{E.22}$$

The term in the brackets can be identified as the time it takes for the electrons to drift back into on dot, which is roughly ~ 100 μs. Therefore $(T_{2,\mathrm{eff}}^*) \sim 2$ μs for our dots without any compensation.

Acknowledgements

The inhomogeneous broadening effect and the idea for its derivation was pointed out to us by Hendrik Bluhm, to whom we are especially grateful for useful discussion. We acknowledge funding from ARO/iARPA, the Department of Defense. This work was performed in part at the Center for Nanoscale Systems (CNS), a member of the National Nanotechnology Infrastructure Network (NNIN), which is supported by the National Science Foundation under NSF award no. ECS-0335765. We thank Sandra Foletti, David Reilly and W. Witzel, for useful discussion.

Appendix F

Etched Structures to define GaAs Quantum Dots

F.1 Motivation

Much progress has been made in the realization of almost all the requirements for a viable singlet-triplet qubit for quantum information processing [DiVincenzo 1998]. Single-qubit initialization, universal control, fast measurement and coherence have been demonstrated, see chapter 2. Two-qubit operations are crucial for the implementation of quantum computing. In order to couple two singlet-triplet qubits, at least two double quantum dots need to be fabricated in close vicinity to allow charge coupling between the two [Taylor 2006; Laird 2010]. Two-qubit operations using dot-dot tunnel coupling is also thinkable and needs two double dots in close vicinity as well.

Depletion gates are a versatile tool for the confinement of double and multiple quantum dots. The need to contact them bears complications for large numbers of devices though because not only the depletion gates themselves need to be intregrated in tight space, connector layers run across the whole mesa and need ~ 100 μm sized bond pads. Furthermore, a large number of metallic gates screens the electrical interaction between the electrons in for example two double dots. Creating confinement without metallic gates, e.g. by etching features into a GaAs heterostructure may thus be a useful tool to be combined with depletion gates to create multiple charge and tunnel coupled quantum dots in close vicinity.

F.2 Etched Lines, Widths and Depths

Reactive ion beam etching when applied to a GaAs heterostructure surface, can etch narrow trenches into the material and thus remove the Si delta-dopant layer, thereby completely depleting the 2DEG underneath. With this in mind, trenches were written using a reactive ion etch, to test the feasibility and the achievable smallest feature size. The work was performed on the RIE7 - Unaxis Shuttleline ICP RIE, an Inductive Coupled Plasma reactor.

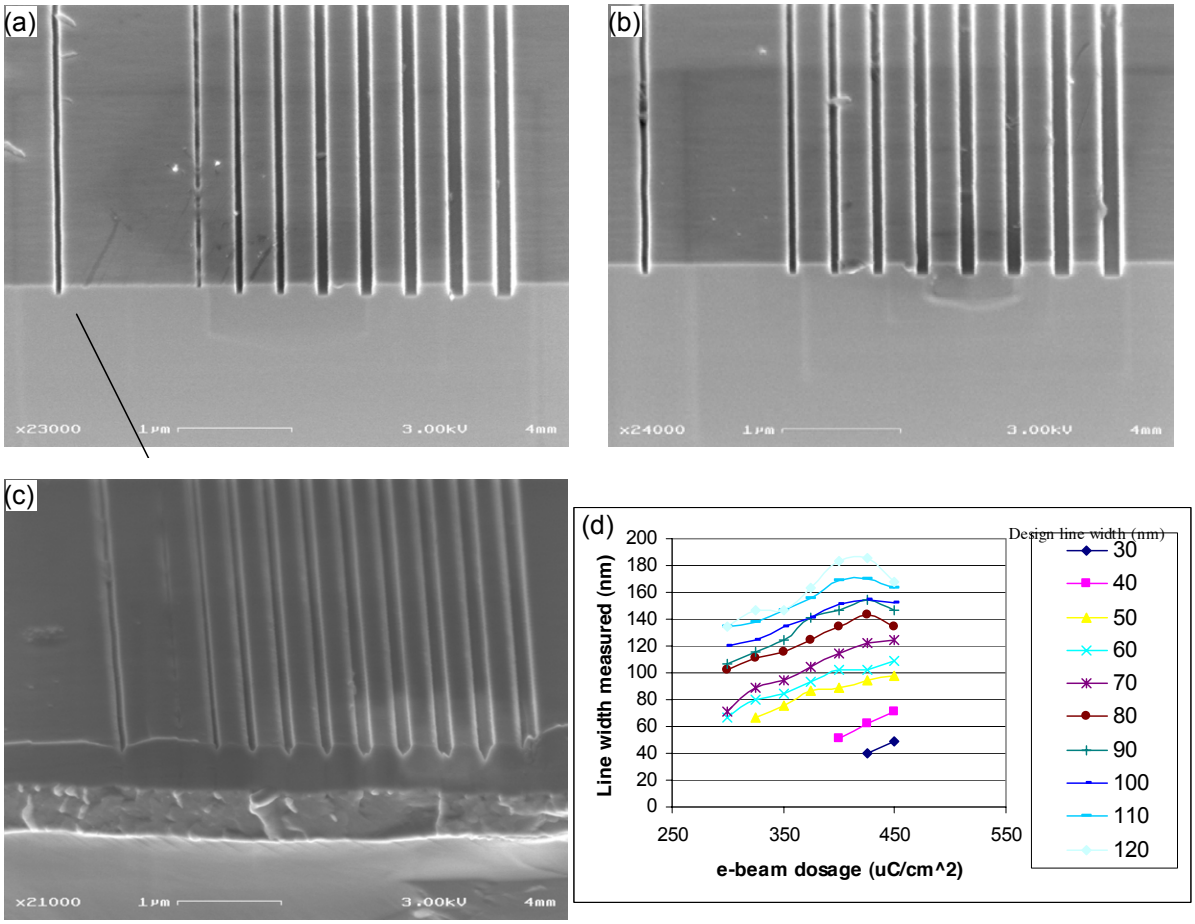

Figure F.1: (a) Scanning electron beam images of cross section of GaAs wafer with trenches etched by reactive ion etching. The e-beam dosage is 300 μC/cm^2, the design line widths are 120 nm for the right line, decreasing by 10 nm for each line towards the left. Lines for design line widths of 30, 40 nm are not visible. (b) Identical to (a) but with e-beam dose of 325 μC/cm^2. (c) Identical to (a) but with e-beam dose of 425 μC/cm^2. The trenches take a wedge shape and are much wider and deeper than intended. (d) Trench widths for etched heterostructures as shown in (a)-(c), as a function of e-beam dosage, for different design trench widths.

Features, defined by e-beam resist, down to 60 nm width can be written and etch depths

of $\sim$ 100 nm, sufficient for dopant-layer removal for most heterostructures, can be achieved. Etch-depth weakly depends on dose, but strongly on design width. For design widths of $\sim$ 50 nm the etch-depth is $\sim$ 100 nm, while the etch depth for $\sim$ 100 nm design width is $\sim$ 200 nm.

SEM images of cross sections of etched trenches are shown in Fig. F.1(a)-(c) for three different e-beam dosages. For the lowest dosage, 300 μC/cm^2, the trenches are not fully etched, while for higher doses the trenches become much deeper and wider than intended and wedge-shaped. For $\sim$ 325, μC/cm^2, see Fig. F.1(b) an optimal line depth ($\sim$ 100 nm) and width [$\sim$ 60 nm, see Fig. F.1(c)] are obtained.

Acknowledgements

The work in this appendix was done in collaboration with Colin Dillard and Ling Xie. Ling Xie performed the etch in the cleanroom at the Center for Nanoscale Systems (CNS), a member of the National Nanotechnology Infrastructure Network (NNIN), which is supported by the National Science Foundation under NSF award no. ECS-0335765.

Bibliography

[Aharonov 1988] Y. Aharonov, D.Z. Albert, and L. Vaidman, *How the result of a measurement of a component of the spin of a spin-1/2 particle can turn out to be 100*, Phys. Rev. Lett. **60**, 1351 (1988).

[Amasha 2008] S. , K. MacLean, I. P. Radu, D. M. Zumbuhl, M. Kastner, M. P. Hanson, and A. C. Gossard, *Electrical Control of Spin Relaxation in a Quantum Dot* Phys. Rev. Lett. **100**, 046803(2008).

[Armen 2002] M. A. Armen *et al.*, *Adaptive Homodyne Measurement of Optical Phase*, Phys. Rev. Lett. **89**, 133602 (2002).

[Astafiev 2004] O. Astaev *et al.*, *Single-shot measurement of the Josephson charge qubit*, Phys. Rev. B **69**, 180507 (2004).

[Barnenco 1995] A. Barenco, *A universal 2-bit gate for quantum computation*, P. Roy. Soc. Lond. A-Mat. **449**, 679 (1995).

[Barthel 2009] C. Barthel, D. J. Reilly, C. M. Marcus, M. P. Hanson, and A. C. Gossard, *Rapid single-shot measurement of a singlet-triplet qubit*, Phys. Rev. Lett. **103**, 160503 (2009).

[Barthel SQD 2010] C. Barthel, M. Kjærgaard, J. Medford, M., M. Stopa, C. M. Marcus, M. P. Hanson, and A. C. Gossard, *Fast sensing of double-dot charge arrangement and spin state with an rf sensor quantum dot*, Phys. Rev. B **81**, 161308(R) (2010).

[Barthel T1 2010] C. Barthel, J. Medford, H. Bluhm, C. M. Marcus, M. P. Hanson, and

A. C. Gossard, *Singlet-Triplet Qubit Relaxation and Initialization in a Magnetic Field Gradient*, in preparation(2010).

[Barthel T2 2010] C. Barthel, J. Medford, C. M. Marcus, M. P. Hanson, and A. C. Gossard, *Dynamic Decoupling and Protected Coherent Operations of a Singlet Triplet Qubit*, in preparation (2010).

[Baugh 2007] J. Baugh, Y. Kitamura, K. Ono, and S. Tarucha, *Large nuclear overhauser fields detected in vertically coupled double quantum dots*, Phys. Rev. Lett. **99**, 4 (2007).

[Beenakker Review 1991] C. W. J. Beenakker, H. van Houten *Quantum Transport in Semiconductor Nanostructures* Solid State Physics **44**, 1 (1991).

[Beenakker CB 1991] C. W. J. Beenakker, *Theory of Coulomb-blockade oscillations in the conductance of a quantum dot* Phys. Rev. B **44**, 1646 (1991).

[Bell 1962] R. L. Bell, *Electric dipole spin transitions in InSb*, Phys. Rev. Lett. **9**, 52 (1962).

[Bleany 1953] B. Bleaney, and K. W. H. Stevens, *Paramagnetic resonance* Rep. Prog. Phys. **16**, 108 (1953)

[Bluhm FB 2010] H. Bluhm, S. Foletti, D. Mahalu, V. Umansky, and A. Yacoby, *Enhancing the Coherence of Spin Qubits by Narrowing the Nuclear Spin Bath Using a Quantum Feedback Loop*, Phys. Rev. Lett., submitted (2010)

[Bluhm T_2 2010] H. Bluhm, S. Foletti, I. Neder, M.Rudner, D. Mahalu, V. Umansky, and A. Yacoby, *Long coherence of electron spins coupled to a nuclear spin bath*, Nature Physics, submitted (2010)

[Buehler 2005] T. M. Buehler, D. J.Reilly, R. P. Starrett, A. D. Greentree, A. R. Hamilton, A. S. Dzurak, and R. G. Clark, *Single-shot readout with the radio-frequency single-electron transistor in the presence of charge noise*, Appl. Phys. Lett. **86** 143117 (2005).

[Buizert 2008] C. Buizert, F. H. L. Koppens, M. Pioro-Ladrière, H.-P. Tranitz, I. T. Vink, S. Tarucha, W. Wegscheider, and L. M. K. Vandersypen, *In situ reduction of charge noise in $GaAs/Al_xGa_{1-x}As$ Schottky-gated devices*, Phys. Rev. Lett. **101**, 1 (2008).

[Carr 1954] H. Y. Carr, E. M. Purcell, *Effects of Diffusion on Free Precession in Nuclear Magnetic Resonance Experiments*, Phys. Rev. 94, 630638 (1954)

[Cassidy 2008] M. Cassidy, *Effects of Diffusion on Free Precession in Nuclear Magnetic Resonance Experiments*, Master's thesis, University of New South Wales (2008)

[CohenTanuoudji 1999] C.Cohen-Tannoudji, *Quantum Mechanics* **2**, 4.3.3 (1999).

[Coish 2005] W. A. Coish, and D. Loss, *Singlet-triplet decoherence due to nuclear spins in a double quantum dot* Phys. Rev. B,**72**, 125337,(2005).

[Cronenwett 2001] S. M. Cronenwett, *Coherence, charging and spin effects in quantum dots and point contacts*, Ph.D. Thesis, Harvard University (2001).

[Das Sarma 2001] S. Das Sarma, *Spintronics*, Am. Sci. **89**, 516 (2001).

[Datta 1990] S. Datta, and B. Das, *Electronic analog of the electrooptic modulator*, Appl. Phys. Lett. **56**, 665 (1990).

[De 2009] A. De, C. E. Pryor, and M. E. Flatte, *Electric-field control of a hydrogenic donor's spin in a semiconductor*, Phys. Rev. Lett. **102**, 017603 (2009).

[Dicarlo 2004] L. Dicarlo, H. Lynch, A. C. Johnson, L. I. Childress, K. Crockett, C. M. Marcus, M. Hanson, and A. C. Gossard, *Differential charge sensing and charge delocalization in a tunable double quantum dot*, Phys. Rev. Lett. **92**, 226801 (2004).

[Dicarlo Thesis 2007] L. Dicarlo, *Mesoscopic Electronics Beyond DC Transport*, Ph.D. Thesis, Harvard University (2007).

[DiVincenzo 1995] D. P. DiVincenzo, *2-bit gates are universal for quantum computation*, Phys. Rev. A **51**, 1015 (1995).

[DiVincenzo 1998] D. P. DiVincenzo, and D. Loss, *Quantum information is physical*, Superlattices Microstruct. **23**, 419 (1998).

[Dobers 1988] M. Dobers, K. V. Klitzing, J. Schneider, G. Weimann, and K. H. Ploog, *Electrical detection of nuclear magnetic-resonance in GaAs-$Al_xGa_{1-x}As$ heterostructures*, Phys. Rev. Lett. **61**, 1650 (1988).

[Drummond 1986] T. Drummond, W. T. Masselink, and H. Morcok, *Modulation-doped GaAs/(Al,Ga)As heterojunction field-effect transistors - modfets*, P. Ieee **74**, 773 (1986).

[Elzerman 2003] J. Elzerman, R. Hanson, J. S. Greidanus, L. H. W. V. Beveren, S. D. Franceschi, L. M. K. Vandersypen, S. Tarucha, and L. P. Kouwenhoven, *Few-electron quantum dot circuit with integrated charge read out*, Phys. Rev. B **67**, 4 (2003).

[Elzerman 2004] J. M. Elzerman, R. Hanson, L. H. Willems van Beveren, B. Witkamp, L. M. K. Vandersypen, and L. P. Kouwenhoven, *Single-shot read-out of an individual electron spin in a quantum dot*, Nature **430**, 431 (2004).

[Engel 2001] H.-A. Engel and D. Loss, *Detection of single spin decoherence in a quantum dot via charge currents*, Phys. Rev. Lett. **86**, 4648 (2001).

[Fermi 1930] E. Fermi, *Über die magnetischen Momente der Atomkerne. (About the magnetic moment of atomic nuclei.)* Z. Phys.**60**, 320 (1930)

[Fertig 1987] H. Fertig, and B. I. Halperin, *Transmission coefficient of an electron through a saddle-point potential in a magnetic field* Phys. Rev. B **36**, 7969 (1987).

[38] R. Feynman, *Simulating physics with computers*, International Journal of Theoretical Physics **21**, 467 (1982).

[Field 1993] M. Field, C. G. Smith, M. Pepper, D. A. Ritchie, J. E. F. Frost, G. A. C. Jones, and D. G. Hasko, *Measurements of Coulomb blockade with a noninvasive voltage probe*, Phys. Rev. Lett. **70**, 1311 (1993).

[Foletti 2009] S. Foletti, H. Bluhm, D. Mahalu, V. Umansky, and A. Yacoby, *Universal quantum control of two-electron spin quantum bits using dynamic nuclear polarization*, Nature physics, **5**, 903 (2009)

[Franken 1961] P. Franken, G. Weinreich, C. Peters, and A. Hill, *Generation of optical harmonics*, Phys. Rev. Lett. **7**, 118 (1961).

[Fujisawa 1998] T. Fujisawa, T. H. Oosterkamp, W. G. van der Wiel, B. W. Broer, R. Aguado, S. Tarucha, and L. P. Kouwenhoven, *Spontaneous Emission Spectrum in Double Quantum Dot Devices*, Science **282**, 932 (1998).

[Fujisawa 2004] T. Fujisawa, T. Hayashi, Y. Hirayamab, H. D. Cheong, and Y. H. Jeong, *Real-time detection of single-electron tunneling current* Appl. Phys. Lett. **84**, 2343 (2004).

[Goldhaber-Gordon 1998] D. Goldhaber-Gordon, H. Shtrikman, D. Mahalu, D. Abusch-Magder, U. Meirav, and M. Kastner, *Kondo effect in a single-electron transistor*, Nature **391**, 156 (1998).

[Golovach 2006] V. N. Golovach, M. Borhani and D. Loss, *Electric-dipole-induced spin resonance in quantum dots*, *Phys. Rev. B*, **74** 165319 (2006)

[Grover 1997] L. Grover, *Quantum mechanics helps in searching for a needle in a haystack*, Phys. Rev. Lett. **79**, 325 (1997).

[Gueron 1959] M. Gueron and C. Ryter, *Overhauser effect in metallic lithium*, Phys. Rev. Lett. **3**, 338 (1959).

[Gulland 2010] M. Gulland, J. J. Krich, J. M. Taylor, H. Bluhm, B. I. Halperin, C. M. Marcus, M. Stopa, A. Yacoby, and M. D. Lukin, *Dynamic Nuclear Polarization in Double Quantum Dots* arXiv: 1003.4508v1 (2010)

[Hahn 1950] E. L. Hahn, *Spin Echoes*, Phys. Rev. 80, 580 (1950)

[Hanson 2003] R. Hanson, B. Witkamp, L. M. K. Vandersypen, L. H. W. V. Beveren,

J. Elzerman, and L. P. Kouwenhoven, *Zeeman energy and spin relaxation in a one-electron quantum dot*, Phys. Rev. Lett. **91**, 196802 (2003).

[Hanson 2007] R. Hanson, L. P. Kouwenhoven, J. R. Petta, S. Tarucha, and L. M. K. Vandersypen, *Spins in few-electron quantum dots*, Rev. Mod. Phys. **79**, 1217 (2007).

[Horowitz 1989] P. Horowitz, and W. Hill, *The art of electronics*, Cambridge University Press, 2 edition (1989)

[Ihn 2009] T. Ihn, S. Gustavsson, U. Gasser, B. Küng, T. Müller, R. Schleser, M. Sigrist, I. Shorubalko, R. Leturcq, and K. Ensslin, *Quantum dots investigated with charge detection techniques* Solid State Communications **149**, 1419-1426 (2009).

[Jelezko 2004] F. Jelezko, T. Gaebel, I. Popa, A. Gruber, and J. Wrachtrup, *Observation of coherent oscillations in a single electron spin*, Phys. Rev. Lett. **92**, 076401 (2004).

[Johnson Nature 2005] A. C. Johnson, J. R. Petta, J. M Taylor, A. Yacoby, M. D. Lukin, C. M. Marcus, M. Hanson, and A. C. Gossard, *Triplet-singlet spin relaxation via nuclei in a double quantum dot*, Nature **435**, 925 (2005).

[Johnson PRB 2005] A. C. Johnson, J. R. Petta, and C. M. Marcus, *Singlet-triplet spin blockade and charge sensing in a few-electron double quantum dot*, Phys. Rev. B **72**, 7 (2005).

[Johnson Thesis 2005] A. C. Johnson, *Charge sensing and spin dynamics in GaAs quantum dots*, Ph.D. Thesis, Harvard University (2005).

[Kato 2003] Y. Kato, R. Myers, D. C. Driscoll, A. C. Gossard, J. Levy, and D. Awschalom, *Gigahertz electron spin manipulation using voltage-controlled g-tensor modulation*, Science **299**, 1201 (2003).

[Katz 2008] N. Katz, M. Neeley, M. Ansmann, R. C. Bialczak, M. Hofheinz, E. Lucero, A. O'Connell, H. Wang, A. N. Cleland, J. M. Martinis, and A. N. Korotkov, *Reversal of the weak measurement of a quantum state in a superconducting phase qubit*, Phys. Rev. Lett. **101**, 200401 (2008).

[Khaetski 2002] A. Khaetskii, D. Loss, and L. Glazman, *Electron spin decoherence in quantum dots due to interaction with nuclei*, Phys. Rev. Lett. **88**, 186802 (2002).

[Khazan 1993] L. Khazan, Y. Rubo, and V. Sheka, *Exchange-induced optical spin transitions in semimagnetic semiconductors*, Phys Rev B **47**, 13180 (1993).

[Kitaev 1997] A. Kitaev, *Quantum computations: algorithms and error correction*, Russ. Math. Surv. **52**, 1191 (1997).

[Koppens 2005] F. H. L. Koppens, J. A. Folk, J. Elzerman, R. Hanson, L. H. W. V. Beveren, I. T. Vink, H.-P. Tranitz, W. Wegscheider, L. P. Kouwenhoven, and L. M. K. Vandersypen, *Control and detection of singlet-triplet mixing in a random nuclear field*, Science **309**, 1346 (2005).

[Koppens 2006] F. H. L. Koppens, C. Buizert, K. J. Tielrooij, I. T. Vink, K. C. Nowack, T. Meunier, L. P. Kouwenhoven, and L. M. K. Vandersypen, *Driven coherent oscillations of a single electron spin in a quantum dot*, Nature **442**, 766 (2006).

[Koppens 2007] F. H. L. Koppens, D. Klauser, W. A. Coish, K. C. Nowack, L. P. Kouwenhoven, D. Loss, and L. M. K. Vandersypen, *Universal phase shift and nonexponential decay of driven single-spin oscillations*, Phys. Rev. Lett. **99**, 106803 (2007).

[Korotkov 1999] A. N. Korotkov, and M. A. Paalanen, *Charge sensitivity of radio frequency single-electron transistor* Appl. Phys. Lett. **74**, 4052 (1999).

[Kouwenhoven 1999] L. P. Kouwenhoven, C. M. Marcus, P. L. McEuen, S. Tarucha, R. M. Westervelt, and N. S. Wingreen, *Electron transport in quantum dots*, in *Mesoscopic Electron Transport* (Kluwer Academic, Dordrecht, 1997).

[Laird 2006] E. A. Laird, J. R. Petta, A. C. Johnson, C. M. Marcus, A. Yacoby, M. P. Hanson, and A. C. Gossard, *Effect of exchange interaction on spin dephasing in a double quantum dot*, Phys. Rev. Lett. **97**, 4 (2006).

[Laird 2007] E. A. Laird, C. Barthel, E. I. Rashba, C. M. Marcus, M. P. Hanson, and A. C. Gossard, *Hyperfine-mediated gate-driven electron spin resonance*, Phys. Rev. Lett. **99**, 246601 (2007).

[Laird 2009] E. A. Laird, C. Barthel, E. I. Rashba, C. M. Marcus, M. P. Hanson, and A. C. Gossard, *A new mechanism of electric dipole spin resonance: hyperfine coupling in quantum dots*, Semicond. Sci. Technol. **24**, 064004 (2009).

[Laird 2010] E. A. Laird, *Electrical control of quantum dot spin qubits* Ph.D. Thesis, Harvard University

[Lee 2008] B. Lee, W. M. Witzel, and S. Das Sarma *Universal Pulse Sequence to Minimize Spin Dephasing in the Central Spin Decoherence Problem* Phys. Rev. Lett. **100**, 160505 (2008)

[Levitov 2003] L. S. Levitov and E. I. Rashba, *Dynamical spin-electric coupling in a quantum dot*, Phys. Rev. B **67**, 5 (2003).

[Levy 2002] J. Levy, *Universal quantum computation with spin-1/2 pairs and Heisenberg exchange*, Phys. Rev. Lett. **89**, 147902 (2002).

[Loss 1998] D. Loss, and D.P. DiVincenzo, *Quantum computation with quantum dots*, Phys. Rev. A **57** 589 (1998).

[Lu 2003] W. Lu, Z. Ji, L. Pfeiffer, K. W. West, and A. J. Rimberg, *Real-time detection of electron tunneling in a quantum dot*, Nature **423** 422 (2003).

[McCombe 1967] B. McCombe, S. Bishop, and R. Kaplan, *Combined resonance and electron g-values in InSb*, Phys. Rev. Lett. **18**, 748 (1967).

[Meiboom 1958] S. Meiboom, D. Gill, *Modified Spin-Echo Method for Measuring Nuclear Relaxation Times* Rev. Sci. Instrum. 29, 688 (1958)

[Merkulov 2002] Merkulov I A, Efros Al L and Rosen M *Electron spin relaxation by nuclei in semiconductor quantum dots*, *Phys. Rev. B*, **65** 205309 (2002)

[Mermin 2007] N. D. Mermin, *Quantum Computer Science* Cambridge University Press, 2007.

[Meunier 2006] T. Meunier, I. Vink, L. H. Willems van Beveren, F. H. .L. Koppens, H.-P. Tranitz, W. Wegscheider, L. P. Kouwenhoven, and L. M. K. Vandersypen,

Single-shot readout of electron spins in a semiconductor quantum dot Phys. Rev. B **74**, 195303 (2006).

[Monzon 1997] F. G. Monzon, M. Johnson, and M. L. Roukes, *Strong Hall voltage modulation in hybrid ferromagnet/semiconductor microstructures* Appl. Phys. Lett. **71** (21), 3087 (1997)

[SETE code] The SETE code is available from the National Nanotechnology Infrastructure Network Computation project through the Harvard University Center for Nanoscale Systems, www.cns.fas.harvard.edu.

[Nowack 2007] K. C. Nowack, F. H. L. Koppens, Y. V. Nazarov, and L. M. K. Vandersypen, *Coherent control of a single electron spin with electric fields*, Science **318**, 1430 (2007).

[Ono 2002] K. Ono, *Current rectification by Pauli exclusion in a weakly coupled double quantum dot system*, Science **297**, 1313 (2002).

[Ono 2004] K. Ono and S. Tarucha, *Nuclear-spin-induced oscillatory current in spin-blockaded quantum dots*, Phys. Rev. Lett. **92**, 256803 (2004).

[Overhauser 1953] A. Overhauser, *Polarization of nuclei in metals*, Phys. Rev. **91**, 476 (1953).

[Paget 1977] D. Paget, G. Lampel, B. Sapoval, and V. Safarov, *Low field electron-nuclear spin coupling in gallium-arsenide under optical-pumping conditions*, Phys. Rev. B **15**, 5780 (1977).

[Pasini 2009] S. Pasini, G. S. Uhrig, *Optimized dynamical decoupling for power-law noise spectra* Phys. Rev. A 81, 012309 (2010)

[Pauli 1925] W. Pauli, *Über den Zusammenhang des Abschlusses der Elektronengruppen im Atom mit der Komplexstruktur der Spektren (On the Connexion between the Completion of Electron Groups in an Atom with the Complex Structure of Spectra)*, Z. Phys. **31**, 765 (1925)

[Pekar 1965] S. I. Pekar and E. I. Rashba, *Combined resonance in crystals in inhomogeneous magnetic fields*, Sov. Phys. - JETP **20**, 1295 (1965).

[Petta 2004] J. R. Petta, A. C. Johnson, C. M. Marcus, M. Hanson, and A. C. Gossard, *Manipulation of a single charge in a double quantum dot*, Phys. Rev. Lett. **93**, 186802 (2004).

[Petta 2005] J. R. Petta, A. C. Johnson, J. M. Taylor, E. A. Laird, A. Yacoby, M. D. Lukin, C. M. Marcus, M. P. Hanson, and A. C. Gossard, *Coherent manipulation of coupled electron spins in semiconductor quantum dots*, Science **309**, 2180 (2005).

[Petta PRB 2005] J. R. Petta, A. C. Johnson, A. Yacoby, C. M. Marcus, M. Hanson, and A. C. Gossard, *Pulsed-gate measurements of the singlet-triplet relaxation time in a two-electron double quantum dot*, Phys. Rev. B **72**, 161301 (2005).

[Petta 2008] J. R. Petta, J. M Taylor, A. C. Johnson, A. Yacoby, M. D. Lukin, C. M. Marcus, M. Hanson, and A. C. Gossard, *Dynamic Nuclear Polarization with Single Electron Spins*, Phys. Rev. Lett. **100**, 067601 (2008).

[Pioro-Ladrière 2007] M. Pioro-Ladrière, Y. Tokura, T. Obata, T. Kubo, and S. Tarucha, *Micromagnets for coherent control of spin-charge qubit in lateral quantum dots*, Appl. Phys. Lett. **90**, 024105 (2007).

[Pioro-Ladriere 2008] M. Pioro-Ladriere, T. Obata, Y. Tokura, Y.-S. Shin, T. Kubo, K. Yoshida, T. Taniyama, and S. Tarucha, *Electrically driven single-electron spin resonance in a slanting Zeeman field*, Nature Physics **4**, 776 (2008).

[Pozar 1988] D. M. Pozar, *Microwave Engineering*, John Wiley (1988).

[Prinz 1998] G. A. Prinz, *Magnetoelectronics*, Science **282**, 1160 (1998).

[Rabi 1937] I. Rabi, *Space quantization in a gyrating magnetic field*, Phys Rev **51**, 0652 (1937).

[Ramon 2007] G. Ramon, and X. Hu, *Dynamical nuclear spin polarization and the Zamboni effect in gated double quantum dots* Phys. Rev. B 75, 161301 (2007)

[Rashba 1962] E. I. Rashba, *Properties of semiconductors with an extremum loop: 1. Cyclotron and combinational resonance in a magnetic field perpendicular to the plane of the loop*, Sov. Phys. Sol. State. **2**, 1109 (1960).

[Rashba 1991] E. I. Rashba and V. I. Sheka *Landau Level Spectroscopy* (Amsterdam: North-Holland)(1991)

[Rashba 2008] E. I. Rashba, *Theory of electric dipole spin resonance in quantum dots: Mean field theory with Gaussian fluctuations and beyond*, Phys. Rev. B **78**, 195302 (2008).

[Reilly APL 2007] D. J. Reilly, C. M. Marcus, M. P. Hanson, and A. C. Gossard, *Fast Single-Charge Sensing with an rf Quantum Point Contact*, Appl. Phys. Lett. **91**, 162101 (2007).

[Reilly 2007] D. J. Reilly, J. M. Taylor, E. A. Laird, J. R. Petta, and C. M. Marcus, *Measurement of temporal correlations of the Overhauser field in a double quantum dot*, Phys. Rev. Lett. **101**, 236803 (2008).

[Reilly Diff. 2008] D. J. Reilly, J. M. Taylor, J. R. Petta, C. M. Marcus, M. Hanson, and A. C. Gossard, *Exchange Control of Nuclear Spin Diffusion in a Double Quantum Dot*, arXiv: 0803.3082v1 (2008).

[Reilly 2008] D. J. Reilly, J. M. Taylor J. R. Petta C. M. Marcus, M. P. Hanson, and A. C. Gossard, *Suppressing Spin Qubit Dephasing by Nuclear State Preparation*, Science **321**, 817 (2008).

[Ribeiro 2008] H. Ribeiro, and G. Burkard, *Nuclear State Preparation via Landau-Zener-St—"uckelberg Transitions in Double Quantum Dots* Phys. Rev. Lett. **102**, 216802 (2009)

[Romito 2008] A. Romito, Y. Gefen, and Y. M. Blanter, *Weak values of electron spin in a double quantum dot*, Phys. Rev. Lett. **100**, 056801 (2008).

[Rudner 2007] M. S. Rudner and L. S. Levitov, *Electrically driven reverse Overhauser pumping of nuclear spins in quantum dots*, Phys. Rev. Lett. **99**, 4 (2007).

[Rugar 2004] D. Rugar, R. Budakian, H. J. Mamin, and B. W. Chui, *Single spin detection by magnetic resonance force microscopy*, Nature **430**, 329 (2004).

[Schoelkopf 1998] R. J. Schoelkopf, P. Wahlgren, A. A. Kozhevnikov, P. Delsing, and D. E. Prober, *The Radio-Frequency Single-Electron Transistor (RF-SET): A Fast and Ultrasensitive Electrometer*, Science **280**, 1238 (1998).

[Schrödinger 1935] E. Schrödinger, *Die gegenwärtige Situation in der Quantenmechanik (The Present Situation in Quantum Mechanics)* , Naturwissenschaften **23** pp.807-812; 823-828; 844-849 (1935).

[Shor 1994] P. Shor, *Algorithms for quantum computation: Discrete logarithms and factoring*, Proceedings, 35th Annual Symposium on Foundations of Computer Science (1994).

[Steane 1996] A. Steane, *Multiple-particle interference and quantum error correction*, P. Roy. Soc. Lond. A-Mat. **452**, 2551 (1996).

[Stopa 1993] M. Stopa, *Coulomb oscillation amplitudes and semiconductor quantum-dot self-consistent level structure*, Phys. Rev. B **48**, 18340 (1993).

[Stopa 1996] M. Stopa, *Quantum dot self-consistent electronic structure and the Coulomb blockade*, Phys. Rev. B **54**, 13767 (1996).

[Stopa 2010] M. Stopa, J. J. Krich, and A. Yacoby, *Inhomogeneous Nuclear Spin Flips*, arXiv: 0905.4520v2 (2010)

[Taylor 2006] J. M. Taylor, H.-A. engel, W. Dür, A. Yacoby, C. M. Marcus, P. Zoller, and M. D. Lukin, *Fault-tolerant architecture for quantum computation using electrically controlled semiconductor spins* Nature Physics, **1**, 177 (2006)

[Taylor PRB 2007] J. M. Taylor, J. R. Petta, A. C. Johnson, A. Yacoby, C. M. Marcus and M. D. Lukin, *Relaxation, dephasing, and quantum control of electron spins in double quantum dots*, Phys. Rev. B **76**, 035315,(2007).

[Taylor Thesis 2007] J. M. Taylor, *Hyperfine Interactions and Quantum Information Processing in Quantum Dots*, Ph.D. Thesis, Harvard University (2007).

[Tokura 2006] Y. Tokura, W. G. van der Wiel, T. Obata, and S. Tarucha *Coherent Single Electron Spin Control in a Slanting Zeeman Field*, Phys. Rev. Lett., **96** 047202 (2006)

[Uhrig 2007] G. S. Uhrig, *Keeping a Quantum Bit Alive by Optimized π-Pulse Sequences* Phys. Rev. Lett. 98, 100504 (2007)

[Van der Wiel 2003] W. G. V. D. Wiel, S. D. Franceschi, J. Elzerman, T. Fujisawa, S. Tarucha, and L. P. Kouwenhoven, *Electron transport through double quantum dots*, Rev. Mod. Phys. **75**, 1 (2003).

[Van Wees 1989] B. J. van van Wees, L. P. Kouwenhoven, C. J. P. M. Harmans, J. Williamson, C. Timmering, M. Broekaart, C. Foxon, and J. Harris, *Observation of zero-dimensional states in a one-dimensional electron interferometer*, Phys. Rev. Lett. **62**, 2523 (1989).

[Wheeler 1983] J. A. Wheeler, and W. H. Zurek (eds), *Quantum Theory and Measurement*, Princeton University Press, (1983)

[Witzel 2005] W. M. Witzel, R. de Sousa, and S. Das Sarma, *Quantum theory of spectral-diffusion-induced electron spin decoherence* Phys. Rev. B **72**, 161306(R) (2005)

[Witzel 2006] W. M. Witzel and S. Das Sarma, *Quantum theory for electron spin decoherence induced by nuclear spin dynamics in semiconductor quantum computer architectures: Spectral diffusion of localized electron spins in the nuclear solid-state environment*, Phys. Rev. B **74**, 035322 (2006)

[Witzel CDD 2007] W. M. Witzel, S. Das Sarma, *Concatenated dynamical decoupling in a solid-state spin bath* Phys. Rev. B **76**, 241303 (2007).

[Witzel CPMG 2007] W. M. Witzel, S. Das Sarma, *Multiple-Pulse Coherence Enhancement of Solid State Spin Qubits*, Phys. Rev. Lett. **78**, 077601 (2007).

[Xiao 2004] M. Xiao, I. Martin, E. Yablonovitch, and H. W. Jiang, *Electrical detection of the spin resonance of a single electron in a silicon field-effect transistor*, Nature, **430** 435 (2004)

[Yao 2006] W. Yao, R.-B. Liu, and L. J. Sham, *Theory of electron spin decoherence by interacting nuclear spins in a quantum dot*, Phys. Rev. B, **74** 195301 (2006)